

AD-A132 845

TURBULENT FLOW IN PASSAGE AROUND A 180 DEG BEND; AN
EXPERIMENTAL AND NUME. (U) CALIFORNIA UNIV BERKELEY
DEPT OF MECHANICAL ENGINEERING J A HUMPHREY SEP 83

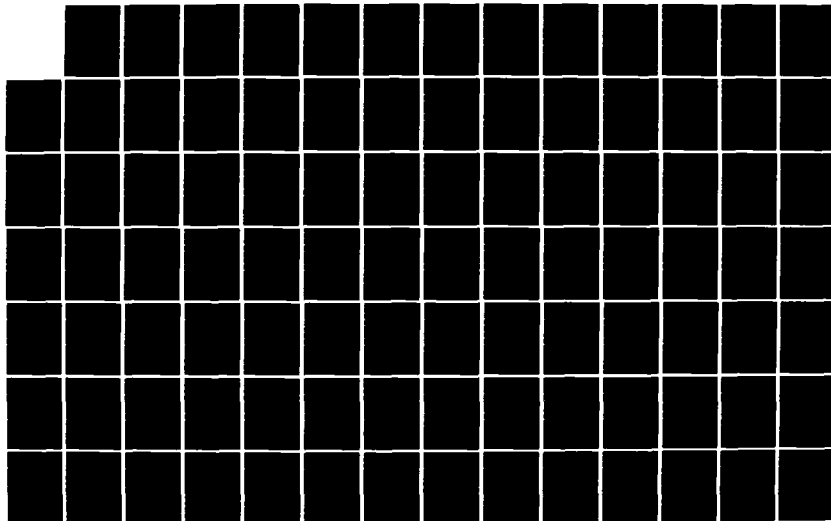
1/2

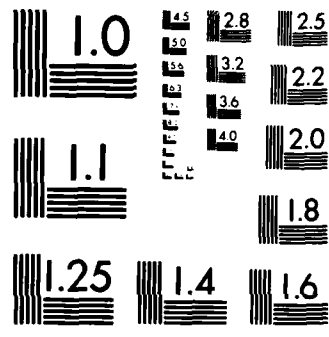
UNCLASSIFIED

UCB/FM-83-7 N00014-80-C-0031

F/G 20/4

NL





MICROCOPY RESOLUTION TEST CHART
NATIONAL BUREAU OF STANDARDS-1963-A

(12)

AD-A132845

University of California
Berkeley Campus

TURBULENT FLOW IN PASSAGE AROUND A 180° BEND;
AN EXPERIMENTAL AND NUMERICAL STUDY

Final Annual Report for Period
October 1, 1982 - September 30, 1983
of Research completed under
ONR (Power Program) Research Contract
N00014-80-C-0031

DTIC
SELECTE
SEP 22 1983
S A D

Principal Investigator J.A.C. Humphrey
Research Assistant S.M. Chang

undertaken in collaboration with
Professor B.E. Launder, University of Manchester
Institute of Science and Technology, Great Britain

This document has been approved
for public release and sale; its
distribution is unlimited.

September 1983

102
Rep. FM-83-7

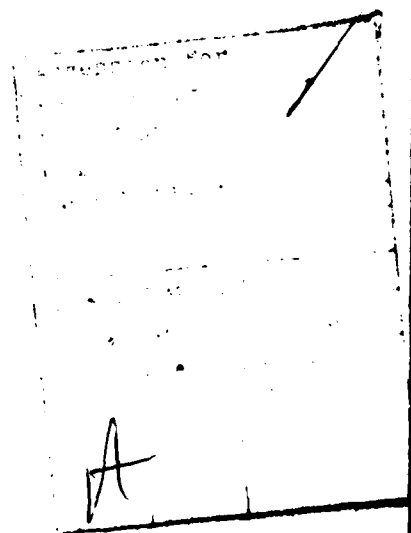
DTIC FILE COPY

REPORT DOCUMENTATION PAGE		READ INSTRUCTIONS BEFORE COMPLETING FORM
1. REPORT NUMBER N00014-80-C-0031A	2. GOVT ACCESSION NO. AD A132 845	3. RECIPIENT'S CATALOG NUMBER
4. TITLE (and Subtitle) Turbulent Flow and Heat Transfer in Passage Around 180° Bend-An Experimental and Numerical Study		5. TYPE OF REPORT & PERIOD COVERED Yearly (Summary) Oct. 1, 1982-Sept. 30, 1983
7. AUTHOR(s) Joseph A.C. Humphrey		6. PERFORMING ORG. REPORT NUMBER
9. PERFORMING ORGANIZATION NAME AND ADDRESS Department of Mechanical Engineering University of California Berkeley, CA 94720		8. CONTRACT OR GRANT NUMBER(s) N00014-80C-0031
11. CONTROLLING OFFICE NAME AND ADDRESS Office of Naval Research 800 N. Quincy Street Arlington, VA 22217		10. PROGRAM ELEMENT, PROJECT, TASK AREA & WORK UNIT NUMBERS
14. MONITORING AGENCY NAME & ADDRESS (if different from Controlling Office)		12. REPORT DATE September 1983
		13. NUMBER OF PAGES 152
		15. SECURITY CLASS. (of this report) unclassified
16. DISTRIBUTION STATEMENT (of this Report) Approved for Public Release; Distribution Unlimited		15a. DECLASSIFICATION/DOWNGRADING SCHEDULE
17. DISTRIBUTION STATEMENT (of the abstract entered in Block 20, if different from Report) Same as Block No. 16		
18. SUPPLEMENTARY NOTES		
19. KEY WORDS (Continue on reverse side if necessary and identify by block number) Turbulence Modeling, Curved Duct Flow, Laser Doppler Velocimetry, Numerical Computation, Finite Differencing, Heat Transfer, Algebraic Stress Modeling, Numerical Diffusion, Secondary Flow.		
20. ABSTRACT (Continue on reverse side if necessary and identify by block number) Work undertaken during a four-year period of research is reported. Laser doppler velocimeter measurements for turbulent flow in a 180° bend of square cross-section are presented and discussed. These reveal previously undocumented anisotropic features in the flow. Limited data are also provided for the flow in the downstream tangent. Numerical predictions of the flow configurations were made with two types of turbulence models. The two-equation (k-ε) model (continued on attached page)		

20. Abstract

yields results in broad agreement with the data but fails to reproduce detailed variations present in the flow. It is shown that while the algebraic stress model can resolve these variations, good spatial resolution of the mean flow field is required.

COPY
RECEIVED
2



Measurement and Calculation of Developing Turbulent Flow
in a U-Bend and Downstream Tangent of Square Cross-Section

ABSTRACT

Experimental measurement and numerical modeling has been performed on the flow in a 180° bend of square cross-section, preceded and followed by straight ducts of the same cross-section.

Measurements of mean velocities and their associated turbulent stresses along the streamwise (θ) and the gapwise or radial (r) directions have been made at several longitudinal planes, using the non-intrusive laser-Doppler velocimeter technique in backscatter mode. Mean flow data reveal features in qualitative agreement with results obtained from inviscid flow analysis. Measurements of the turbulent stresses display previously undocumented anisotropic characteristics arising from shearing motions induced in the core of the flow. In the downstream tangent, measurements show that drastic reductions of the secondary motion take place in less than 5 hydraulic diameters. From then on, however, the flow recovers only slowly from the effects of the bend.

Numerical predictions using a $k-\epsilon$ model of turbulence have been performed for the experimental configuration. Model deficiencies are

more clearly revealed by the higher order accuracy of the finite differencing scheme used and the implementation of a partially-parabolic calculation algorithm. It is found that, with the problem of numerical diffusion relieved, false physical diffusion and the isotropic characteristics inherent in the model are the main causes for the differences observed between measurements and computations.

Additional predictions with an algebraic stress model (ASM) show poor agreement with the measurements. As a result, two "experimental" tests have been carried out to check indirectly the predicting ability of the ASM closure. It is found that the proposed model is capable of resolving the anisotropy of the turbulence correctly, provided that the mean velocity field is known accurately.

FOREWORD

This report represents the culmination of a four year effort undertaken at the Berkeley Campus, aimed at measuring and making predictable the turbulent flow in passage through a 180° curved duct of square cross section. The research program initially started out as a joint venture with the Davis campus of the University of California. After year one, the Davis portion of the program, under the direction of Professor Brian E. Launder, was moved to the University of Manchester Institute of Science and Technology. In spite of the distances and difficulties involved, the close and beneficial collaboration with Professor Launder and his group at UMIST continued uninterruptedly throughout the duration of the program in Berkeley. We are indebted to Mr. K. Ellingsworth of the Office of Naval Research for making the collaboration possible.

Whereas research in UMIST has centered on the heat transfer aspects of turbulent flow in bends, that in Berkeley has dealt exclusively with the fluid mechanics. At the time of writing measurements are being obtained, in Berkeley, in a 180° curved pipe to extend the data base available. The results will be reported in a subsequent addendum to this report. The data will be used by the UMIST team to test and validate a numerical procedure for predicting turbulent flow in curved ducts of circular cross-section.

CONTENTS

ACKNOWLEDGEMENTS	iv	
LIST OF TABLES	vi	
LIST OF FIGURES	vii	
CHAPTER 1	INTRODUCTION	1
1.1	The problem of Interest	1
1.2	Objectives	2
1.3	Earlier Work	3
1.3.1	Experimental Studies	3
1.3.2	Numerical Calculation/Modeling	5
1.4	Outline of the Thesis	8
CHAPTER 2	The EXPERIMENT	9
2.1	Introduction	9
2.2	Flow System and Instrumentation	9
2.3	Experimental Methodology	13
2.4	Error Estimates	16
CHAPTER 3	MEAN FLOW EQUATIONS AND TURBULENCE MODELS	19
3.1	Introduction	19
3.2	Mean Flow Equations and the Problem of Closure	19
3.3	Modeling of Turbulence	22
3.3.1	$k-\epsilon$ Model	22
3.3.2	Algebraic Stress Model	26
3.3.3	Summary of the ASM Relations for Flows in a Duct of Square Cross-Section	33

CHAPTER 4	NUMERICAL PROCEDURE	40
4.1	Introduction	40
4.2	Partially-Parabolic Flows	40
4.3	Discretization	42
4.4	Numerical Prescriptions of Boundary Conditions	48
4.5	Solution Algorithm	49
CHAPTER 5	VALIDATION	52
5.1	Introduction	52
5.2	Laminar Flow Tests	53
5.3	Testing of Turbulence Models	55
CHAPTER 6	RESULTS AND DISCUSSION	59
6.1	Introduction	59
6.2	Turbulent Flow Measurements and the k- ϵ model Calculations	59
6.3	The ASM Predictions	73
CHAPTER 7	CONCLUSIONS AND RECOMMENDATIONS	77
REFERENCES		82
TABLES		88
FIGURES		92

ACKNOWLEDGEMENTS

The contents of this report are based primarily on the Ph.D. Thesis of Dr. S.M. Chang.

It is with pleasure that we acknowledge a close and beneficial collaboration during the course of this work with Professor Brian E. Launder, Mr. R.W. Johnson and Mr. H. Iacovides of the University of Manchester, Institute of Science and Technology. During its early stages, the project benefited from the participation of Dr. T. Han (numerical modeling) and Dr. A. Modavi and Dr. J. Sabnis (experimental measurement). We also are indebted to Messieurs N. Al-Shama, G. Beshori and G. Lewis for their help in building and maintaining the experimental apparatus.

This investigation was made possible by a grant from the Office of Naval Research through Contract No. N00014-80-C-0031. Additional funds for computations were provided by the Technical Coordination Staff of the Office of Fossil Energy of the U.S. Department of Energy, under Contract No. DE-AC03-76SF0098 through the Fossil Energy Materials Program, Oakridge National Laboratory, Oakridge, Tennessee. We are indebted to Mr. K. Ellingsworth of the

Office of Naval Research, and Mr. A. Levy of the Lawrence
Berkeley Laboratory for their continued interest and
support for this work.

LIST OF TABLES

- Table 2.1 Estimated maximum measurement errors
- Table 4.1 QUICK scheme formulae for convective terms over a cross-stream plane
- Table 6.1 Grid distribution over a cross-stream plane for the k- ϵ model calculations
- Table 6.2 Grid distribution over a cross-stream plane for the algebraic stress model calculations

LIST OF FIGURES

- Figure 1.1 General flow pattern of the secondary motion of the first kind in a curved duct of square cross-section.
- Figure 1.2 General flow pattern of the secondary motion of the second kind in a straight duct of square cross-section.
- Figure 2.1 Schematic showing test section dimensions, coordinate system and velocity components of the flow.
- Figure 2.2 Optimum experimental arrangement of stainless steel screens and perforated plate in the flow-uniformizing section preceding the upstream tangent.
- Figure 2.3 Top and side view of laser-Doppler velocimeter aligned for measurements at a bend angle $\theta = 180^\circ$. Traversing mechanism details are not shown.
- Figure 4.1 Location of variables on the calculation grid.
- Figure 4.2 Definition of control volumes.
- Figure 4.3 Definition of dimensions and subscripts appearing in equation (4.3.1).
- Figure 5.1 Fully developed laminar flow in a 2D straight channel. (·) HYBRID calculation; (—) exact solution.
- Figure 5.2 Fully developed laminar flow in a 2D curved channel of $(r_o - r_i)/r_i = 1.0$. (·) HYBRID calculations; (—) exact solution.
- Figure 5.3 Fully developed laminar flow in a straight duct with one wall moving at a constant speed normal to the main flow direction.
- Figure 5.4 Laminar flow in a 90° curved duct of square cross-section with fully developed velocity profile near the inlet plane to the bend. (---) QUICK; (—) HYBRID; (o) measurements of Humphrey et al. [1977].
- Figure 5.5 $k-\epsilon$ model calculation of fully-developed turbulent flow in a 2D straight channel; mean longitudinal velocity U/U_{\max} .
- Figure 5.6 $k-\epsilon$ model calculation of fully developed turbulent flow in a 2D straight channel; turbulent energy $(k/U_{\max}^2) \times 100$.

- Figure 5.7 Fully developed turbulent flow in a 2D straight channel; distributions of \bar{u}_x , \bar{u}_y and \bar{u}_z calculated by using the ASM relations and U_x , k^x , k^y and ϵ^z from the k- ϵ model calculation.
- Figure 5.8 ASM calculation of fully developed turbulent flow in a 2D straight channel; mean longitudinal velocity U/U_{\max} .
- Figure 5.9 ASM calculation of fully developed turbulent flow in a 2D straight channel; \bar{u}_x/U_{\max} , \bar{u}_y/U_{\max} and \bar{u}_z/U_{\max} .
- Figure 5.10 ASM calculation of fully developed turbulent flow in a 2D straight channel; $\overline{u_x u_y}/U_{\max}^2$.
- Figure 5.11 ASM calculation of fully developed turbulent flow in a 2D curved channel; \bar{u}_θ/U_θ and $U_\theta/U_{\theta,\max}$: (—) measurements of Eskinazi and Yeh [1956]; (---) ASM calculation; (---) ASM calculation with non-symmetric f-function of Humphrey and Pourahmadi [1982].
- Figure 5.12 ASM calculation of fully developed turbulent flow in a 2D curved channel; $\overline{u_r u_\theta}/U_{\theta,\max}$ and u_r/U_θ : (— and o) measurements; (---) ASM calculation; (-.-) ASM calculation with non-symmetric f-function of Humphrey and Pourahmadi [1982].
- Figure 6.1 Distribution of pressure coefficient ($C_p = \Delta P/\rho U_B^2$) in the bend and tangents for conditions of the experiment: $Re = 56,700$, $R_c/D_H = 3.35$ and $De = 21,900$. Measurements made through pressure taps on side walls of test section components.
- Figure 6.2 Comparison between turbulent flow measurements of mean velocity and normal stress from this work (o) at $X_H = -1$ and measurements by Melling and Whitelaw (—) after a development length of $36.8 D_H$.
- Figure 6.3 Turbulent flow measurements of mean velocity and normal stress in the upstream tangent at $X_H = -5$.
- Figure 6.4 Turbulent measurements of mean velocity and normal stress in the upstream tangent at $X_H = -1$.
- Figure 6.5 Turbulent flow measurements and k- ϵ model calculations of mean velocity and normal stress in the bend at $\theta = 3^\circ$: (—) HYBRID, (---) QUICK; dashed line at 0.875 is best fit to measurements.
- Figure 6.6 Turbulent flow measurements and k- ϵ model calculations of mean velocity and normal stress in the bend at $\theta = 45^\circ$: (—) HYBRID, (---) QUICK.

- Figure 6.7 Turbulent flow measurements and k- ϵ model calculations of mean velocity and normal stress in the bend at $\theta = 90^\circ$: (—) HYBRID, (---) QUICK; dashed line at 0.875 is best fit to measurements.
- Figure 6.8 Turbulent flow measurements and k- ϵ model calculations of mean velocity and normal stress in the bend at $\theta = 130^\circ$: (—) HYBRID, (---) QUICK.
- Figure 6.9 Turbulent flow measurements and k- ϵ model calculations of mean velocity and normal stress in the bend at $\theta = 177^\circ$: (—) HYBRID, (---) QUICK; dashed lines at 0.75 and 0.875 are best fits to measurements.
- Figure 6.10 Turbulent flow measurements of mean velocity and normal stress in the downstream tangent at $X_H = 1$.
- Figure 6.11 Turbulent flow measurements and k- ϵ model calculations of mean velocity and normal stress in the downstream tangent at $X_H = 5$: (—) HYBRID, (---) QUICK; dashed line at 0.875 is best to fit measurements.
- Figure 6.12 Turbulent flow measurements of mean velocity and normal stress in the downstream tangent at $X_H = 10$; dashed lines at 0.75 and 0.875 are best fits to measurements.
- Figure 6.13 Turbulent flow measurements of mean velocity and normal stress in the downstream tangent at $X_H = 20$; dashed line at 0.875 is best fit to measurements.
- Figure 6.14 Turbulent flow measurements of shear stress at $X_H = -5$ and -1 : (o) data from this work; (—) data from Melling and Whitelaw; dashed lines at 0.75 are best fit to data.
- Figure 6.15 Turbulent flow measurements of shear stress at four longitudinal stations in the bend; dashed line at 0.75 is best fit to measurements.
- Figure 6.16 Turbulent flow measurements of shear stress at four longitudinal stations in the downstream tangent; dashed lines are best fits to measurements.
- Figure 6.17 Turbulent flow predictions (k- ϵ model) of cross-stream and streamwise velocities at $\theta = 177^\circ$: velocity components are normalized by U_B ; outer radius (concave) wall is shown at the top of each plot.
- Figure 6.18 ASM calculations of U_θ/U_B at $\theta = 45^\circ$: (—) best fits to measurements, (---) ASM, (----) k- ϵ model.

- Figure 6.19 ASM calculations of $(\tilde{u}_\theta/U_B) \times 100$ at $\theta = 45^\circ$: (—) best fits to measurements, (---) ASM.
- Figure 6.20 ASM calculations of (U_r/U_B) at $\theta = 45^\circ$: (—) best fits to measurements, (---) ASM, (----) k- ϵ model.
- Figure 6.21 ASM calculations of $(\tilde{u}_r/U_B) \times 100$ at $\theta = 45^\circ$: (—) best fits to measurements, (---) ASM.
- Figure 6.22 ASM calculations of U_θ/U_B at $\theta = 90^\circ$: (—) best fits to measurements, (---) ASM, (----) k- ϵ model.
- Figure 6.23 ASM calculations of $(\tilde{u}_\theta/U_B) \times 100$ at $\theta = 90^\circ$: (—) best fits to measurements, (---) ASM. (---) "experimental" test #1.
- Figure 6.24 ASM calculations of (U_r/U_B) at $\theta = 90^\circ$: (—) best fits to measurements, (---) ASM, (----) k- ϵ model.
- Figure 6.25 ASM calculations of $(\tilde{u}_r/U_B) \times 100$ at $\theta = 90^\circ$: (—) best fits to measurements, (---) ASM, (---) "experimental" test #1.
- Figure 6.26 ASM calculations of U_θ/U_B at $\theta = 177^\circ$: (—) best fits to measurements, (---) ASM, (----) k- ϵ model.
- Figure 6.27 ASM calculations of $(\tilde{u}_\theta/U_B) \times 100$ at $\theta = 177^\circ$: (—) best fits to measurements, (---) ASM.
- Figure 6.28 ASM calculations of (U_r/U_B) at $\theta = 177^\circ$: (—) best fits to measurements, (---) ASM, (----) k- ϵ model.
- Figure 6.29 ASM calculations of $(\tilde{u}_r/U_B) \times 100$ at $\theta = 177^\circ$: (—) best fits to measurements, (---) ASM.
- Figure 6.30 ASM calculations of U_θ/U_B at $x/D_H = 1$: (—) best fits to measurements, (---) ASM, (----) k- ϵ model.
- Figure 6.31 ASM calculations of $(\tilde{u}_\theta/U_B) \times 100$ at $x/D_H = 1$: (—) best fits to measurements, (---) ASM.
- Figure 6.32 ASM calculations of (U_r/U_B) at $x/D_H = 1$: (—) best fits to measurements, (---) ASM, (----) k- ϵ model.

- Figure 6.33 ASM calculations of $(\bar{u}_r/U_B) \times 100$ at $x/D_H = 1$: (—) best fits to measurements, (---) ASM.
- Figure 6.34 ASM calculations of $(\overline{u_\theta u_r}/U_B^2) \times 100$ at $\theta = 45^\circ$: (—) best fits to measurements, (---) ASM.
- Figure 6.35 ASM calculations of $(\overline{u_\theta u_r}/U_B^2) \times 100$ at $\theta = 90^\circ$: (—) best fits to measurements, (---) ASM.
- Figure 6.36 ASM calculations of $(\overline{u_\theta u_r}/U_B^2) \times 100$ at $\theta = 177^\circ$: (—) best fits to measurements, (---) ASM.
- Figure 6.37 ASM calculations of $(\overline{u_\theta u_r}/U_B^2) \times 100$ at $x/D_H = 1$: (—) best fits to measurements, (---) ASM.
- Figure 6.38 ASM calculations of $(\overline{u_\theta u_r}/U_B^2) \times 100$ at $\theta = 90^\circ$: (—) best fits to measurements, (---) ASM, (---) "experimental" test #1, (.....) "experimental" test #2.

CHAPTER 1. INTRODUCTION

1.1 The Problem of Interest

Considerable efforts have been devoted to the study of flow in curved conduits over the past 40 years due to its fundamental as well as industrial importance. When a fluid flows through a curved duct of square cross-section, the radial pressure gradient established in the core region (directed to the center of curvature) acts upon the slower moving fluid near the side walls, causing the fluid there to move to the inner (convex) side of the bend. In turn, faster moving fluid in the core region moves to the outer (concave) side of the bend, producing the secondary motion depicted in Figure 1.1. In addition to the pressure-gradient driven secondary flow described above, gradients of the turbulent stresses in a plane normal to the main flow direction can also produce secondary motion in ducts of non-circular cross-section. The sense of this secondary motion in a straight duct of square cross-section is shown in Figure 1.2 over a quarter of the cross-section. It carries high momentum fluid from the core region toward a corner along the corner bisector and pushes low momentum fluid near the walls back to the central region along the wall bisectors. This secondary motion causes the contours of mean longitudinal velocity to bulge toward the corners and, as a result, enhances the heat transfer rate and shear stress there. In the literature, the secondary motion induced by streamline curvature is usually referred to as the "secondary motion of the first kind" whereas that produced by gradients of turbulent stresses is

sometimes called the "secondary motion of the second kind." The theory of both types of secondary motions has been reviewed by Johnston [1978].

The flow configuration of interest to the present study consists of a 180° circular bend of square cross-section preceeded and followed by straight ducts or tangents. This U-shaped geometry is found in numerous piping systems and industrial flow configurations. In particular, it is directly relevant to compact heat exchangers. The flow patterns established in and downstream of a U-bend strongly influence the heat transfer characteristics which, in turn, dictate the overall performance of a heat exchanger. The study of this type of flow also provides further understanding of turbulent flow phenomena in turbo-machinery components and, thus, can lead to the improved design of these components.

1.2 Objectives

The primary objectives of this study are:

- 1) To obtain measurements of the mean flow and turbulence characteristics by means of laser-Doppler velocimetry in a U-bend and downstream tangent of equal square cross-section.

Because the present configuration involves the combined effects of flow in a 180° bend and the downstream tangent, a complex flow of very distinct and previously undocumented velocity characteristics emerges. Besides serving to advance understanding of the flow, the experimental data should also be of value for developing and testing turbulence models suitable for three-dimensional complex turbulent flows.

2) To test the respective capabilities of a two equation ($k-\epsilon$) model and an algebraic stress model of turbulence for predicting the mean flow and its turbulence characteristics.

Previous elliptic calculations of Humphrey et al. [1981] with a $k-\epsilon$ model for turbulent flow in a 90° bend of square cross-section yielded results in poor agreement with their measurements for bend angles greater than 45° . However, in that study it was not possible to separate satisfactorily the inadequacy of the $k-\epsilon$ model from inaccuracies of numerical origin. Subsequent work by Chang et al. [1982] using a partially-parabolic procedure and a quadratic upwind-weighted interpolation for convection terms (the QUICK scheme) yielded substantially improved predictions. In the present study their numerical procedure is employed whenever possible to establish more precisely the performance and limitations of the two turbulence models explored.

1.3 Earlier Work

1.3.1 Experimental Studies

Measurements of turbulent flows in bends of constant rectangular cross-sections have been made by Joy [1950], Eichenberger [1952, 1953] and Squire [1954] and, more recently, by Bruun [1979], Humphrey et al. [1981] and Taylor et al. [1982]. Joy [1950] measured the total pressure distributions in three rectangular bends (aspect ratio 2:1) of different radii to the bend center for two turning angles (either 90° or 180°). He discovered that for the 180° configuration, the direction of secondary motion was reversed at a bend angle around $\theta = 135^\circ$. Further experimental

evidence of the oscillatory nature of secondary motions in bends of prolonged curvature were also found by Eichenberger [1952] and Squire [1954], and was summarized by Hawthorne [1963].

In a study on the influence of inlet boundary layer thickness on secondary flow development and pressure losses, Bruun [1979] performed detailed measurements of mean values of the total pressure, static pressure and velocity fields as well as limited measurements of turbulence intensity distributions in two 120° bends of rectangular cross-sections. By analyzing the measurements, he was able to present a physical description of the secondary flow processes.

The measurements of developing mean flow and turbulence characteristics in a 90° bend of square cross-section by Humphrey et al. [1981] and Taylor et al. [1982] are directly related to the present work. These studies were performed by using Laser-Doppler velocimetry techniques in the same bend for the same Reynolds number. The only difference between the two experiments was the boundary layer thickness of the flow at the bend inlet plane. In the work of Taylor et al. [1982] thin boundary layers were purposefully induced at the bend inlet plane, whereas in Humphrey et al. [1981] essentially fully developed straight duct flow was presented as the inlet condition. The most marked differences between the results of these two studies were, in general, the: a) stronger secondary motion, and b) higher levels of turbulence, experienced by the flow with thicker inlet boundary layers.

Detailed measurements of the much weaker Reynolds stress driven secondary motions for the case of developing flow in a duct of square cross-section have been reported by Melling and Whitelaw [1976], and in

a series of papers by Gessner et al., the latest reference being [1982]. It is noteworthy that the flow field measurements of Humphrey et al. [1981] and Taylor et al. [1982] do not show the symmetric corner vortex structures characteristic of straight duct flow. This supports the notion that in the bend sections of these studies the cross-stream flow was influenced more strongly by the transverse mean pressure-gradient than by gradients of the Reynolds stresses.

1.3.2 Numerical Calculation/Modelling

Curved duct turbulent flow calculations based on the numerical solution of the Navier-Stokes equations have been made by Humphrey, Whitelaw and Yee [1981] for their experimental configuration, and more recently by Buggeln, Briley and McDonald [1980] for the flow measured by Taylor, Whitelaw and Yianneskis [1982]. In the work of Humphrey et al. [1981] a two-equation $k-\epsilon$ model of turbulence was used whereas Buggeln et al. [1980] employed the one-equation model investigated by Shamroth and Gibeling [1979]. In general, both studies show good agreement between measurements and calculations of the mean velocity components up to a bend angle of approximately 45° , but as of this point significant deviations appear. For bend angles larger than 45° calculations of Buggeln et al. [1980] are in better accord with the measurements than corresponding results of Humphrey et al. [1981]. This is attributed primarily to the thinner boundary layer inlet condition present in the measurements of Taylor et al. [1982], which was responsible for the production of weaker secondary motions than were observed and predicted by Humphrey et al. [1981]. It should be remarked that cost considerations

dictated the use of coarse grids in both of the above studies and, since significant levels of numerical diffusion probably affected the results, there is an inadequate basis for judging the merits and demerits of the turbulence models used respectively by the authors.

A review of computational methods for internal flows has been carried out by McNally and Sockol [1981]. The following is a brief summary relating to numerical techniques of relevance to this work. Within the class of numerical methods which neglects streamwise diffusion is the partially-parabolic procedure proposed by Pratap and Spalding [1975] for calculating flow in curved ducts. In this method, iterated forward marching sweeps of the three-dimensional flow field are performed, yielding solutions of the momentum equations and corrections to the pressure field, until local and global continuity are attained. This type of numerical procedure was used by Chang et al. [1982] to predict the flow of Humphrey et al. [1981] after modifying the procedure to include quadratic upstream interpolation of convection terms as in Han et al. [1981] to reduce numerical diffusion. In general, better agreement was found in Chang et al. [1982] than in Humphrey et al. [1981] between mean velocity measurements and calculations as a consequence of the numerical improvements to the calculation scheme.

Inviscid flow approximations for the calculation of flows in curved ducts have been proposed by, for example, Briley and McDonald [1979]. The numerical procedure developed by these authors represents an extension of viscous forward marching methods in that it accounts approximately for transverse variations in streamwise pressure gradient. While this approach appears particularly promising for fast and relatively inexpen-

sive curved flow computations, work continues on its development and application; see Krekovsky, Briley and McDonald [1980].

In contrast to the pressure-dominated flows arising in curved ducts, the difficulties associated with predicting Reynolds stress driven secondary motions in ducts of non-circular cross-section are principally related to the accurate modeling of cross-stream turbulent flow anisotropy. Brundrett and Baines [1964] have shown that the turbulence term contributing most strongly to mean streamwise vorticity in steady, incompressible, constant property flow is $\frac{\partial^2}{\partial y \partial z} (\overline{u_y^2} - \overline{u_z^2})$. In a later study, Perkins

[1970] also demonstrated the importance of the term $(\frac{\partial^2}{\partial z^2} - \frac{\partial^2}{\partial y^2}) \overline{u_y u_z}$.

In these terms, y , z , u_y and u_z are the cross-stream coordinates and velocity fluctuations respectively. It can readily be shown that turbulence models based on the notion of an isotropic turbulent viscosity, such as the $k-\epsilon$ model, cannot account for the generation of stress-driven secondary motions. In their recent study, Naot and Rodi [1981] have reviewed briefly various investigations employing Reynolds stress level closures to predict these motions. They conclude that the essential basic flow features can be predicted qualitatively with relatively simple algebraic stress closures. It is noteworthy that, except for the full Reynolds stress closure predictions by Reece [1976], all numerical studies of the problem have neglected convection and diffusion contributions to the balance of $\overline{u_i u_j}$, thus implying the condition of a homogeneous turbulent flow.

1.4 Outline of the Thesis

The remainder of this thesis describes the study performed in greater detail throughout the next six chapters. In Chapter 2 the experimental program is presented. This includes descriptions of the apparatus and instrumentation, the experimental methodology, and the major error sources with estimates of their magnitudes. In Chapter 3 the numerical model framework for predicting turbulent flows is established. In Chapter 4 the concept of partially-parabolic flows is introduced, followed by a detailed account of the numerical procedure as well as the boundary conditions used.

The performance of the numerical procedure and the turbulence models were separately checked, by reference to calculations of several appropriately documented flows. The results of these tests are presented in Chapter 5. Chapter 6 discusses the measured and calculated results. Finally, major conclusions and specific recommendations are summarized in Chapter 7.

CHAPTER 2. THE EXPERIMENT

2.1 Introduction

In this chapter the experimental part of the research project is described. Section 2.2 outlines the flow system, the instrumentation, and the flow conditions for which data were taken. Section 2.3 details the experimental methodology and finally, Section 2.4 discusses major error sources and estimates of their magnitudes.

2.2 Flow System and Instrumentation

The experimental system was composed of: a water rig, of which the most important component was the flow test section; a laser-Doppler velocimeter and its associated electronic instrumentation; a motorized traversing mechanism; and a PDP-11/34a Digital Equipment Corporation minicomputer.

The basic components of the flow test section and the coordinate systems are shown schematically in Figure 2.1, and comprised two straight ducts and a bend of square cross-sections. The tangents were each 31 hydraulic diameters long and were respectively attached to the 0° (inlet) and 180° (outlet) planes of the bend. The ratio of bend mean radius of curvature to hydraulic diameter was $R_c/D_H = 3.35$. The bend component was constructed by machining an open, curved channel of mean radius of curvature $R_c = 14.92$ cm (± 0.02 cm) into one of the faces of a large, flat, solid piece of plexiglass 7.6 cm thick. A plexiglass plate 1.27 cm

thick was machined to fit snugly as a lid over the open channel piece, so yielding an enclosed curved duct shape of cross-section dimensions $4.45 \times 4.45 \text{ cm}^2$ ($\pm 0.02 \times 0.02 \text{ cm}^2$). An O-ring seal placed between the open channel piece and the lid prevented water leaks. The modular form of this construction made disassembly easy for surface cleaning purposes. The upstream and downstream tangents were each 138 cm (± 0.02 cm) long and were also constructed from plexiglass, with flat walls 1.27 cm thick. These two ducts were joined by flanges to the bend, with special care taken to avoid possible mismatches between the component cross-sections which otherwise might disturb the flow.

A flow-straightening section 7.15 hydraulic diameters long was placed upstream of the straight duct attached to the bend inlet plane. The purpose of this device was to uniformize and accelerate the development of the cross-stream plane distribution of the flow approaching the bend in the upstream tangent. Various arrangements of differently sized stainless steel screens were tested in combination with one or more perforated plexiglass plates 3.175 cm thick, containing 85 holes of 3.175 mm diameter arranged in a rectangular array spaced 4.495 mm on the centers in each direction. The most successful arrangement of plates and screens in the uniformizing section was found experimentally and is shown in Figure 2.2.

The test section was part of a closed loop system through which water at 20°C was made to flow by gravity from a constant head tank. From this tank the flow passed through the test section, and then into a large sump tank from where it was pumped back to the constant head tank by a 3/4 HP Burkes centrifugal pump. The constant head was ensured

by a large diameter PVC overflow pipe extending through the bottom of the head tank. Flow to the head tank was controlled by a gate valve and measured using a 2 in. Barco venturi meter (P.N. 2-393) connected to a 50 in. (1.27 m) differential mercury manometer. In order to rule out the possibility of propagating perturbations induced by flow components, the use of valves, sharp bends and metering devices was avoided altogether along the test section flow loop. Flow to and from the test section tangents was channelled through 2 in. i.d. tygon tube pieces; flexible enough to be bent without kinks over a large radius of curvature, yet stiff enough to avoid wall collapse due to flow-induced pressure drop. Baffles located in the constant head tank served to dampen the swirling motion of the flow leaving the tank. Residual swirl from the head tank and secondary motions induced by mild curvature in the tygon tube upstream of the test section were eliminated by the flow-uniformizing section placed between the tygon tube and the upstream tangent. All experiments were conducted for the flow rate condition imposed by the constant head tank. This corresponded to a Reynolds number of $Re = 56,700$ and a Dean number of $De = 21,900$ in the flow test section.

Measurements of the mean flow and turbulence characteristics were made using the laser-Doppler velocimeter technique in backscatter mode. The velocimeter employed is shown schematically in Figure 2.3 in relation to the flow test section. It comprised a 2 watt Lexel Argon-Ion water-cooled laser, a mirror stage for reflecting the laser beam 180° into the velocimeter optics, the optics, and a 4 in. (10.2 cm) diameter mirror for reflecting the converging velocimeter beams from the horizontal to the vertical direction. This mirror also served the function of

reflecting the back-scattered Doppler-shifted radiation into the velocimeter collecting optics. The optics were of the DISA 55X Modular Series and consisted of: two separately adjustable quarter-wave retardation plates; a 50:50 neutral beam splitter; a beam color splitter; a back-scatter unit (containing a mirror inclined 45° with respect to the velocimeter optical axis, and serving to support at right angles to the optical axis the photomultiplier optics consisting of: a color separator; two interference filters and two RCA-4526 photomultiplier tubes); a pinhole section; a beam translator and a 310 mm achromatic focusing lens.

The laser and velocimeter optics were mounted to the top of a thick aluminum table, which was itself firmly bolted to an x, y, z traversing mechanism. The traversing mechanism could displace the table top ± 7.5 cm in $5 \mu\text{m}$ increments along any of the coordinate axes by means of three linearly encoded stepping motors monitored by the Digital Equipment Corporation PDP 11/34a minicomputer. The minicomputer functioned as the central data acquisition and reduction controller. In addition to directing the spatial sequence of an experimental run, the computer was programmed to conduct the acquisition, statistical processing, plotting and storage of Doppler data validated and measured by a DISA 55L96 Doppler signal processor or "counter". The PDP 11/34a has a 256 K 16 bit random access memory and is equipped with dual hard RL01 magnetic disc drives (5 Mbytes each). The computer interacts by means of an RT-11 software package with various input-output devices, including a Tektronix 4025 graphics terminal, a Decwriter II hardcopy terminal and a Tektronix 4662 digital pen plotter.

2.3 Experimental Methodology

Prior to an experimental run, water was allowed to flow through the rig until it was purged of air bubbles and had attained a steady thermal state corresponding to 20°C ($\pm 1^{\circ}\text{C}$). Mass flow through the test section was controlled by setting the constant head overflow condition to a mere trickle and continuously monitoring the pressure drop through the venturi meter connected to the head tank feed line.

At any given streamwise measurement station, the velocimeter support table was manually positioned such that the velocimeter horizontal optical axis was oriented perpendicular to the test section side; see Figure 2.3 for an example corresponding to a streamwise location of $\theta = 180^{\circ}$. Fine adjustments to the 90° beam deflector mirror ensured that the velocimeter vertical optical axis was perpendicular to the test section top surface. In combination, these adjustments produced a fringe pattern which was parallel (to within $\pm 0.3^{\circ}$ at any y, z cross-section location) to the cross-stream plane of the test section. The velocimeter optical probe volume was formed by the intersection of two 514.5 nm (green) light beams with a half-angle in air of 4.90° , for which the volume characteristics were: a diameter of 0.09 mm , a length of 1.1 mm , and a fringe spacing of $3.02\text{ }\mu\text{m}$ with about 28 fringes contained in the probe. In reality, spatial filtering and threshold settings on the counter reduced the dimensions of the optical probe. The probe volume was positioned at the top outer-wall corner, inside the test section, by fine control of the motorized traversing table. Positioning in the x and y coordinate directions was accurate to within $\pm 0.05\text{ mm}$ while positioning in the z direction was accurate to better than $\pm 0.5\text{ mm}$.

With the reference corner position at a streamwise location established, the computer software was activated which controls signal acquisition and data processing on a sequentially scanned measurement-grid. After flow symmetry had been established at various streamwise stations, the bulk of the measurements were restricted to a symmetrical half of the test section, on a grid consisting of 4 to 5 profiles at different z locations, each containing 29 to 31 equally spaced points in the y direction. At each point on the measurement-grid the mean flow and turbulence characteristics were statistically determined from populations of 5 to 10 samples consisting of 1,000 measurements each. Each measurement was required to satisfy the counter 5/8 validation comparison to within a preset tolerance of 3%. At every validation of a Doppler burst a "data ready" signal was issued by the counter to a logic conversion circuit. This circuit then sent a triggering pulse to the computer parallel line interface module which was checked for data availability by a software loop approximately every 20 μ s. No interrupt routines were used for obtaining data due to the higher sample rates made possible by the handshake technique. Data rates of about 1 kHz, with approximately 60% validation, were obtained after the flow was seeded with cornstarch particles ranging in size between 1 and 10 μ m. Optical alignment and automatic grid scanning were performed at the following streamwise locations: $x_H = -5, -1, 1, 5, 10, 20$ in the straight ducts, and $\theta = 3^\circ, 45^\circ, 90^\circ, 130^\circ, 177^\circ$ in the bend.

Although capable of two-component measurements; the availability of only one counter during the early stages of this work restricted the use of the velocimeter to single channel mode for most of the experiments.

Values for the streamwise component of mean velocity and normal stress, U_θ and $\overline{u_\theta^2}$, were derived directly from measurements obtained with the velocimeter fringes aligned perpendicularly to the streamwise coordinate direction. Values for the transverse components, U_r and $\overline{u_r^2}$, and for the Reynolds stress, $\overline{u_\theta u_r}$, were derived as described in Melling and Whitelaw [1976] by combining measurements obtained with fringes oriented at angles of $+45^\circ$ and -45° with respect to the streamwise direction. As a check, measurements of U_θ and $\overline{u_\theta^2}$ obtained in this manner were found to agree to within experimental error with the direct observations. Measurements involving the velocity component in the spanwise (z) coordinate direction could not be made accurately due to optical inaccessibility of the flow.

While the bulk of the measurements were made in the manner described above, with the velocimeter in single channel mode, towards the end of the experiment the availability of a second counter allowed us to perform a limited number of measurements using the two velocimeter channels simultaneously. For this case the interference fringe patterns were respectively aligned parallel and perpendicular to the streamwise velocity component. To resolve flow directional ambiguity, and also to optimize the filter range of the counters, a net frequency shift of 700 kHz was imposed on both channels using a DISA 55N10 Bragg cell combined with electronic downmixing. In this way additional measurements at $X_H = -5, -1, 1$ and 5 in the respective tangents were obtained. In addition, careful checks were conducted of the data previously obtained at $X_H = -5$ and 5 and at $\theta = 3^\circ$ and 177° . In general, the checks showed very good agreement between the two measurement methods, for both of the

velocity components and their respective normal stresses. However, at $X_H = -5$ the two methods differed markedly with respect to the measurement of the very weak transverse velocity component arising at this location. The first method consistently showed larger scatter in the measurements and the uncertainty was ultimately traced to relatively small but significant inaccuracies associated with determining the $\pm 45^\circ$ orientations required by this method. At $X_H = -5, -1, 1$ and 5 , and $\theta = 3^\circ$, it is the more accurate frequency-shifted transverse velocity data which is reported here.

2.4 Error Estimates

Error sources affecting the accuracy (systematic error) and precision (random error) of laser-Doppler measurements have been discussed by, for example, Durst, Melling and Whitelaw [1976], Drain [1980] and Buchhave [1979]. In this study the most serious systematic errors were attributed to velocity gradient broadening and velocity bias respectively. Velocity gradient broadening has been analyzed by Melling [1975] who proposed a simple method for estimating its magnitude. Various weighting methods have been proposed by, among others, McLaughlin and Tiederman [1973], George [1975] and Buchhave [1975] to correct for the velocity bias effect, but none of these is entirely satisfactory; they all involve assumptions regarding the statistical distribution of particles in the flow and, in practice, the corrections can be influenced by the additional problem of "incomplete-signal bias". For the conditions of this study, gradient broadening and velocity bias were estimated to be significant only in the near wall regions of the flow, where

velocity gradients and turbulence intensities were highest and the data rate lowest. Fortunately, the errors are of similar magnitude and of opposite sign, tending to cancel out their respective effects on the measurements. For this reason, and because the errors were small anyway, corrections were not applied to the measurements. Table 2.1 presents estimates of the maximum combined inaccuracies of these two error sources on the quantities measured.

Values of the transverse mean velocity component, U_r , and of the Reynolds stress, $\overline{u_\theta u_r}$, were prone to a third systematic error. At the last four locations in the bend, and at $X_H = 10$ and 20 , these two quantities were derived from measurements taken at $+45^\circ$ and -45° to the streamwise flow direction. An error in setting this 90° angle could seriously affect the accuracy of these measurements. The problem has been considered by Humphrey [1977] for a flow of similar characteristics to the present one, and he shows that an angular uncertainty of 0.4° can lead to an error of 5% in U_r and $\pm 3\%$ in $\overline{u_\theta u_r}$. In this work special care was taken to ensure a maximum angular uncertainty of less than 0.3° in setting the $\pm 45^\circ$ beam orientations.

The two main sources of random error affecting the precision of the measurements were attributed to statistical sampling uncertainty (due to the finite size of sample populations) and uncertainty in the determination of the reference or normalizing velocity, U_B . Estimates of the first uncertainty were derived from the measurements themselves and, for all quantities, were found to be less than $\pm 1\%$ r.m.s. error. The error in U_B was larger ($\pm 2\%$) and arose principally from uncertainties in the construction of the venturi meter. As a further check, the

bulk mass flow at each longitudinal station was estimated by integrating the measurements. This yielded a value of U_B which was within $\pm 6\%$ of the venturi meter measurement. Estimates of the maximum combined effects of these two errors on the measurements are provided in Table 2.1.

Measurements of the pressure coefficient, C_p , in the straight and curved duct test sections, using side wall pressure tapings connected to an inclined manometer bank, were also prone to a random r.m.s. error ranging from $\pm 10\%$ at low absolute values of C_p to $\pm 5\%$ at the higher values. The uncertainty in C_p was due mainly to the reading error associated with the manometer bank.

CHAPTER 3. MEAN FLOW EQUATIONS AND TURBULENCE MODELS

3.1 Introduction

In this chapter the numerical modeling framework for predicting turbulent flows is detailed. Section 3.2 presents the mean flow equations and discusses the problem of closure common to all nonlinear stochastic systems. Section 3.3 describes the models tested in the present study. These include the k- ϵ model of turbulence in Section 3.3.1 and the algebraic stress model (ASM) in Section 3.3.2. The model constants for both the k- ϵ and the ASM closures are also given in Section 3.3.2. Finally, the ASM relations appropriate for the present flow configuration is summarized in Section 3.3.3.

3.2 Mean Flow Equations and the Problem of Closure

In the present study numerical calculations of turbulent flows were based upon the time-averaged Navier-Stokes equation and continuity equation as first proposed by Osborne Reynolds. For a statistically stationary flow of a fluid with uniform density ρ , Reynolds decomposition of the field variables followed by time averaging of the resulting equations yields

Continuity:

$$\frac{1}{r} \frac{\partial}{\partial r} (r U_r) + \frac{\partial}{\partial x} (U_x) + \frac{\partial}{\partial z} (U_z) = 0 \quad (3.2.1)$$

Momentum:

$$\begin{aligned}
 & \frac{1}{r} \frac{\partial}{\partial r} (\rho r U_r U_r) + \frac{\partial}{r \partial \theta} (\rho U_\theta U_r) + \frac{\partial}{\partial z} (\rho U_z U_r) - j \frac{\rho U_r^2}{r} = - \frac{\partial p}{\partial r} \\
 & + \frac{1}{r} \frac{\partial}{\partial r} (\mu r \frac{\partial U_r}{\partial r}) + \frac{\partial}{r \partial \theta} (\mu \frac{\partial U_r}{\partial \theta}) + \frac{\partial}{\partial z} (\mu \frac{\partial U_r}{\partial z}) - j (\frac{\mu U_r}{r^2} + \frac{2\mu}{r} \frac{\partial U_\theta}{\partial \theta}) \\
 & + \frac{1}{r} \frac{\partial}{\partial r} (-\rho r \overline{u_r u_r}) + \frac{\partial}{r \partial \theta} (-\rho \overline{u_r u_\theta}) + \frac{\partial}{\partial z} (-\rho \overline{u_r u_z}) + j \frac{\rho \overline{u_\theta u_\theta}}{r}
 \end{aligned} \tag{3.2.2}$$

$$\begin{aligned}
 & \frac{1}{r} \frac{\partial}{\partial r} (\rho r U_r U_\theta) + \frac{\partial}{r \partial \theta} (\rho U_\theta U_\theta) + \frac{\partial}{\partial z} (\rho U_z U_\theta) + j \frac{\rho U_r U_\theta}{r} = - \frac{\partial p}{r \partial \theta} \\
 & + \frac{1}{r} \frac{\partial}{\partial r} (\mu r \frac{\partial U_\theta}{\partial r}) + \frac{\partial}{r \partial \theta} (\mu \frac{\partial U_\theta}{\partial \theta}) + \frac{\partial}{\partial z} (\mu \frac{\partial U_\theta}{\partial z}) - j (\frac{\mu U_\theta}{r^2} - \frac{2\mu}{r} \frac{\partial U_r}{\partial \theta}) \\
 & + \frac{1}{r} \frac{\partial}{\partial r} (-\rho r \overline{u_r u_\theta}) + \frac{\partial}{r \partial \theta} (-\rho \overline{u_\theta u_\theta}) + \frac{\partial}{\partial z} (-\rho \overline{u_\theta u_z}) - j \frac{\rho \overline{u_r u_r}}{r}
 \end{aligned} \tag{3.2.3}$$

$$\begin{aligned}
 & \frac{1}{r} \frac{\partial}{\partial r} (\rho r U_r U_z) + \frac{\partial}{r \partial \theta} (\rho U_\theta U_z) + \frac{\partial}{\partial z} (\rho U_z U_z) = - \frac{\partial p}{\partial z} \\
 & + \frac{1}{r} \frac{\partial}{\partial r} (\mu r \frac{\partial U_z}{\partial r}) + \frac{\partial}{r \partial \theta} (\mu \frac{\partial U_z}{\partial \theta}) + \frac{\partial}{\partial z} (\mu \frac{\partial U_z}{\partial z}) \\
 & + \frac{1}{r} \frac{\partial}{\partial r} (-\rho r \overline{u_r u_z}) + \frac{\partial}{r \partial \theta} (-\rho \overline{u_\theta u_z}) + \frac{\partial}{\partial z} (-\rho \overline{u_z u_z})
 \end{aligned} \tag{3.2.4}$$

where lower and upper case u's stand for fluctuating and time-averaged velocity components respectively, P represents mean pressure, overbars imply time averaging of the correlations in question and μ denotes the viscosity of the fluid.

Equations (3.2.1) to (3.2.4) can be applied to both cylindrical (r, θ, z) and rectangular (y, x, z) coordinate systems. To get the appropriate equations in rectangular coordinates, set $j = 0$ and $r = 1$ and make the following substitutions:

$$\frac{\partial}{\partial \theta} \rightarrow \frac{\partial}{\partial x}, \quad \frac{\partial}{\partial r} \rightarrow \frac{\partial}{\partial y}, \quad U_{\theta} \rightarrow U_x \quad \text{and} \quad U_r \rightarrow U_y$$

wherever they appear. The governing equations in cylindrical coordinates can be deduced simply by setting $j = 1$ in equations (3.2.1) to (3.2.4).

Unfortunately, the above set of equations can not be solved directly for the mean velocities and pressure due to the appearances of the six correlations: $\overline{u_r u_r}$, $\overline{u_{\theta} u_{\theta}}$, $\overline{u_z u_z}$, $\overline{u_r u_{\theta}}$, $\overline{u_r u_z}$ and $\overline{u_{\theta} u_z}$. The quantities $-\overline{\rho u_r u_r}$, $-\overline{\rho u_{\theta} u_{\theta}}$, $-\overline{\rho u_z u_z}$, $-\overline{\rho u_r u_{\theta}}$, $-\overline{\rho u_r u_z}$ and $-\overline{\rho u_{\theta} u_z}$ are known as turbulent or Reynolds stresses. Exact transport equations for these correlations can be derived, however they contain correlations of even higher order due to the nonlinear nature of the equations. "Closure" therefore can not be achieved by resorting to solving transport equations of higher and higher order. Instead, model approximations must be introduced at a certain order in terms of lower order correlations and mean quantities. This constitutes the task of turbulence modeling which is the subject of next section.

3.3 Modeling of Turbulence

As mentioned earlier, the role of turbulence modeling is to provide a path for the determination of the Reynolds stresses appearing in equations (3.2.2) to (3.2.4). Depending upon the level of closure and the generality/complexity desired, a wide variety of models have been proposed and tested. For a comprehensive review, see Launder and Spalding [1972], Reynolds [1976] and Rodi [1978]. Two models of turbulence were selected for the present study: a two-equation ($k-\epsilon$) model and an algebraic Reynolds stress model. Their essential features are outlined in the next two subsections.

3.3.1 $k-\epsilon$ Model

Following Boussinesq [1877], the turbulent stresses are related to the mean rate-of-strain tensor via the definition of an isotropic turbulent viscosity, μ_t . In cylindrical/rectangular coordinates, these relations take the forms given below.

$$-\rho \overline{u_r u_r} = \mu_t \left(2 \frac{\partial U_r}{\partial r} \right) - \frac{2}{3} \rho k \quad (3.3.1.1)$$

$$-\rho \overline{u_\theta u_\theta} = \mu_t \left(2 \frac{\partial U_\theta}{r \partial \theta} + j 2 \frac{U_r}{r} \right) - \frac{2}{3} \rho k \quad (3.3.1.2)$$

$$-\rho \overline{u_z u_z} = \mu_t \left(2 \frac{\partial U_z}{\partial z} \right) - \frac{2}{3} \rho k \quad (3.3.1.3)$$

$$-\rho \overline{u_r u_\theta} = \mu_t \left(\frac{\partial U_r}{r \partial \theta} + \frac{\partial U_\theta}{\partial r} - j \frac{U_\theta}{r} \right) \quad (3.3.1.4)$$

$$-\rho \overline{u_r u_z} = \mu_t \left(\frac{\partial U_z}{\partial r} + \frac{\partial U_r}{\partial z} \right) \quad (3.3.1.5)$$

$$-\rho \overline{u_\theta u_z} = \mu_t \left(\frac{\partial U_z}{r \partial \theta} + \frac{\partial U_\theta}{\partial z} \right) \quad (3.3.1.6)$$

Equations (3.3.1.1) to (3.3.1.6) are completely analogous to the constitutive relations for an incompressible flow of a Newtonian fluid, except for the additional term $2\rho k/3$ which appears in each of the normal stress relations. This addition is necessary to ensure that the definition of turbulence energy

$$k = \frac{1}{2} (\overline{u_r u_r} + \overline{u_\theta u_\theta} + \overline{u_z u_z})$$

is not violated.

Substituting equations (3.3.1.1) to (3.3.1.6) into equations (3.2.2) to (3.2.4) and rearranging yields:

$$\begin{aligned} & \frac{1}{r} \frac{\partial}{\partial r} (\rho r U_r U_r) + \frac{\partial}{\partial \theta} (\rho U_\theta U_r) + \frac{\partial}{\partial z} (\rho U_z U_r) - j \frac{\rho U_\theta^2}{r} = -\frac{\partial p'}{\partial r} \\ & + \left\{ \frac{1}{r} \frac{\partial}{\partial r} (\mu_t r \frac{\partial U_r}{\partial r}) + \frac{\partial}{\partial \theta} (\mu_\theta \frac{\partial U_r}{r \partial \theta}) + \frac{\partial}{\partial z} (\mu_z \frac{\partial U_r}{\partial z}) - j \frac{\mu_\theta}{r} \left(\frac{U_r}{r} + 2 \frac{\partial U_\theta}{r \partial \theta} \right) \right\} \\ & + \left\{ \frac{\partial}{\partial z} (\mu_z \frac{\partial U_z}{\partial r}) + \frac{1}{r} \frac{\partial}{\partial r} (\mu_t r \frac{\partial U_r}{\partial r}) + \frac{\partial}{\partial \theta} (\mu_\theta \frac{\partial U_\theta}{\partial r}) - j \left[\frac{\partial}{\partial \theta} (\mu_t \frac{U_\theta}{r}) + \mu_t \frac{U_r}{r^2} \right] \right\} \end{aligned} \quad (3.3.1.7)$$

$$\begin{aligned}
& \frac{1}{r} \frac{\partial}{\partial r} (\rho r U_r U_\theta) + \frac{\partial}{\partial \theta} (\rho U_\theta U_\theta) + \frac{\partial}{\partial z} (\rho U_z U_\theta) + j \frac{\rho U_r U_\theta}{r} = - \frac{\partial p'}{\partial \theta} \\
& + \left\{ \frac{1}{r} \frac{\partial}{\partial r} (\mu_c r \frac{\partial U_\theta}{\partial r}) + \frac{\partial}{\partial \theta} (\mu_c \frac{\partial U_\theta}{\partial \theta}) + \frac{\partial}{\partial z} (\mu_c \frac{\partial U_\theta}{\partial z}) - j \frac{\mu_c}{r} (U_\theta - 2 \frac{\partial U_r}{\partial \theta}) \right\} \\
& + \left\{ \frac{\partial}{\partial x} (\mu_c \frac{\partial U_z}{\partial \theta}) + \frac{\partial}{\partial r} (\mu_c \frac{\partial U_r}{\partial \theta}) + \frac{\partial}{\partial \theta} (\mu_c \frac{\partial U_\theta}{\partial \theta}) \right\} \\
& + j \left[2 \frac{\partial}{\partial \theta} (\mu_c \frac{U_r}{r}) - \frac{\partial}{\partial r} (\mu_c \frac{U_\theta}{r}) + \frac{\mu_c}{r} (\frac{\partial U_\theta}{\partial r} - \frac{U_\theta}{r}) \right] \quad (3.3.1.8)
\end{aligned}$$

$$\begin{aligned}
& \frac{1}{r} \frac{\partial}{\partial r} (\rho r U_r U_z) + \frac{\partial}{\partial \theta} (\rho U_\theta U_z) + \frac{\partial}{\partial z} (\rho U_z U_z) = - \frac{\partial p'}{\partial z} \\
& + \left\{ \frac{1}{r} \frac{\partial}{\partial r} (\mu_c r \frac{\partial U_z}{\partial r}) + \frac{\partial}{\partial \theta} (\mu_c \frac{\partial U_z}{\partial \theta}) + \frac{\partial}{\partial z} (\mu_c \frac{\partial U_z}{\partial z}) \right\} \\
& + \left\{ \frac{1}{r} \frac{\partial}{\partial r} (\mu_c r \frac{\partial U_r}{\partial z}) + \frac{\partial}{\partial \theta} (\mu_c \frac{\partial U_\theta}{\partial z}) + \frac{\partial}{\partial z} (\mu_c \frac{\partial U_z}{\partial z}) \right\} \quad (3.3.1.9)
\end{aligned}$$

where $\rho' = \rho + \frac{2}{3} \rho k$

and $\mu_c = \mu_c + \mu$.

With the Boussinesq eddy viscosity approximation, the task of modeling is shifted to the determination of μ_t . Using the k - ϵ model, μ_t is determined from two turbulence quantities: the turbulence energy k and its rate of dissipation ϵ , via the relation

$$\mu_t = \rho C_\mu \frac{k^2}{\epsilon} \quad (3.3.1.10)$$

where C_μ , to first approximation, is a constant of proportionality. Following Jones and Launder [1972], the modelled k and ϵ transport equations are:

$$\begin{aligned} \frac{1}{r} \frac{\partial}{\partial r} (r U_r k) + \frac{\partial}{\partial \theta} (r U_\theta k) + \frac{\partial}{\partial z} (r U_z k) &= \rho P - \rho \epsilon \\ + \frac{1}{r} \frac{\partial}{\partial r} \left(\left[\mu + \frac{\mu_t}{\sigma_k} \right] r \frac{\partial k}{\partial r} \right) + \frac{\partial}{\partial \theta} \left(\left[\mu + \frac{\mu_t}{\sigma_k} \right] \frac{\partial k}{\partial \theta} \right) + \frac{\partial}{\partial z} \left(\left[\mu + \frac{\mu_t}{\sigma_k} \right] \frac{\partial k}{\partial z} \right) \end{aligned} \quad (3.3.1.11)$$

$$\begin{aligned} \frac{1}{r} \frac{\partial}{\partial r} (r U_r \epsilon) + \frac{\partial}{\partial \theta} (r U_\theta \epsilon) + \frac{\partial}{\partial z} (r U_z \epsilon) &= -C_{\epsilon 1} \rho \frac{\epsilon}{k} P - C_{\epsilon 2} \rho \frac{\epsilon^2}{k} \\ + \frac{1}{r} \frac{\partial}{\partial r} \left(\left[\mu + \frac{\mu_t}{\sigma_\epsilon} \right] r \frac{\partial \epsilon}{\partial r} \right) + \frac{\partial}{\partial \theta} \left(\left[\mu + \frac{\mu_t}{\sigma_\epsilon} \right] \frac{\partial \epsilon}{\partial \theta} \right) + \frac{\partial}{\partial z} \left(\left[\mu + \frac{\mu_t}{\sigma_\epsilon} \right] \frac{\partial \epsilon}{\partial z} \right) \end{aligned} \quad (3.3.1.12)$$

$$\begin{aligned}
P = \frac{\mu_t}{\rho} & \left[2 \left[\left(\frac{\partial U_r}{\partial r} \right)^2 + \left(\frac{\partial U_\theta}{r \partial \theta} \right)^2 + \left(\frac{\partial U_z}{\partial z} \right)^2 - \frac{U_\theta}{r} \left(\frac{\partial U_r}{r \partial \theta} + \frac{\partial U_\theta}{\partial r} \right) \right. \right. \\
& + \frac{U_r}{r} \left(\frac{U_r}{r} + 2 \frac{\partial U_\theta}{r \partial \theta} \right) + \left(\frac{\partial U_r}{r \partial \theta} \cdot \frac{\partial U_\theta}{\partial r} + \frac{\partial U_z}{r \partial \theta} \cdot \frac{\partial U_\theta}{\partial z} \right) \\
& \left. \left. + \frac{\partial U_r}{\partial z} \cdot \frac{\partial U_z}{\partial r} \right] + \left(\frac{U_\theta}{r} \right)^2 + \left(\frac{\partial U_\theta}{\partial r} \right)^2 + \left(\frac{\partial U_r}{r \partial \theta} \right)^2 + \left(\frac{\partial U_z}{\partial r} \right)^2 + \left(\frac{\partial U_z}{r \partial \theta} \right)^2 \right]
\end{aligned}
\tag{3.3.1.13}$$

Equations (3.2.1) and (3.3.1.7) to (3.3.1.13), together with appropriate boundary conditions form a closed system. Results of k-ε model calculations will be presented in Chapter 6.

3.3.2 Algebraic Stress Model

Algebraic stress models (ASM's) are special cases of full Reynolds stress models proposed by, among others, Hanjalic and Launder [1972] and Launder et al. [1975].

The starting point of ASM is the transport equation for $\overline{u_i u_j}$.* For a fluid of uniform density and viscosity and unaffected by external force fields, this equation can be written as:

*For ease of presentation and general discussion, Cartesian tensor notation is adopted in this section. Final algebraic relations appropriate to both cylindrical and rectangular coordinates are summarized in Section 3.3.3.

influential role in the $\overline{u_i u_j}$ equations. Since this term makes no net contribution to the turbulence energy but merely redistributes it among the normal stresses, it is also referred to as the "redistribution" term. The theoretical background for modelling ϕ_{ij} in terms of equation (3.3.2.3) was discussed in Hanjalic and Launder [1972] and Launder et al. [1975]. It can be shown that there are three types of physical processes which dictate the distribution of ϕ_{ij} : 1) mutual interactions between turbulence components ($\phi_{ij,1}$); 2) mean rate-of-strain interacting with the turbulence ($\phi_{ij,2}$); and 3) corrections to $\phi_{ij,1}$ and $\phi_{ij,2}$ resulting from the presence of walls ($\phi'_{ij,1}$ and $\phi'_{ij,2}$). The modelling of the four terms in equation (3.3.2.3) is outlined next.

For $\phi_{ij,1}$, Rotta's [1951] proposal was adopted whereby

$$\phi_{ij,1} = -C_1 \left(\frac{\epsilon}{k}\right) (\overline{u_i u_j} - \frac{2}{3} \delta_{ij} k) . \quad (3.3.2.4)$$

The primary functions of this term are to equalize normal stresses and to diminish to zero shear stresses. For this reason, it is usually referred to as the "return-to-isotropy" term.

For $\phi_{ij,2}$, Launder et al. [1975] have suggested

$$\phi_{ij,2} = -C_2 (P_{ij} - \frac{2}{3} \delta_{ij} P) \quad (3.3.2.5)$$

as the simpler alternatives for a more complete model of which the first term, apart from a proportionality constant, is the same as that given in equation (3.3.2.5).

Experiments show that the presence of a wall affects the turbulence by damping the fluctuating velocity component normal to the wall and by enhancing those components along the other two directions. In the present study these wall effects were modelled through $\phi'_{ij,1}$ and $\phi'_{ij,2}$ as

$$\phi'_{ij,1} = C_1' \left(\frac{\epsilon}{k} \right) (\overline{u_k u_m} n_k n_m \delta_{ij} - \frac{3}{2} \overline{u_k u_i} n_k n_j - \frac{3}{2} \overline{u_k u_j} n_k n_i) f\left(\frac{\ell}{n_i r_i}\right) \quad (3.3.2.6)$$

$$\phi'_{ij,2} = C_2' (\phi_{km} n_k n_m \delta_{ij} - \frac{3}{2} \phi_{ki} n_k n_j - \frac{3}{2} \phi_{kj} n_k n_i) f\left(\frac{\ell}{n_i r_i}\right) \quad (3.3.2.7)$$

where r_i is the position vector to the point in question, ℓ is a characteristic turbulent length scale, n_i is the unit normal to the wall and f is an empirical function of distance whose primary role is to diminish the respective influences of $\phi'_{ij,1}$ and $\phi'_{ij,2}$ with increased distance from the wall. Equation (3.3.2.6) was first proposed by Shir [1973] in a numerical study of atmospheric turbulent flows in the idealized planetary boundary layer. Gibson and Launder [1978] later extended Shir's idea to account for the wall effect expressed by $\phi'_{ij,2}$ as given by equation (3.3.2.7). For a two-dimensional straight channel, f was assumed to vary as recommended by Reece [1977] according to the expression

$$f\left(\frac{\ell}{y}\right) = \frac{k^{3/2}}{C_W \epsilon} \left[\frac{1}{y} + \frac{1}{D-y} \right] \quad (3.3.2.8)$$

where y is the distance measured from one of the two walls and D is the channel width. The constant C_W was chosen such that $f \rightarrow 1$ as $y \rightarrow 0$. It can be shown that in a region where the logarithmic law of the wall prevails and the turbulence is in local equilibrium that $C_W = \kappa / C_\mu^{3/4}$. For flows inside a square duct with two sets of opposing walls, it was assumed, following Reece [1977], that the influences of both sets of walls on ϕ_{ij} are independent of each other and can be added algebraically.

The model assumptions introduced so far in equations (3.3.2.2) to (3.3.2.8) for ϵ_{ij} and ϕ_{ij} are algebraic since they contain no spatial

gradient of the Reynolds stresses. If the remaining convection and diffusion terms in the $\overline{u_i u_j}$ -transport equation can also be modelled by expressions without gradients of $\overline{u_i u_j}$, equation (3.3.2.1) is reduced to the following algebraic form

$$\overline{u_i u_j} = \overline{u_i u_j} (\overline{u_p u_q}, \frac{\partial U_\ell}{\partial x_m}, k, \epsilon). \quad (3.3.2.9)$$

Models of this kind have been proposed by Launder [1972] and Rodi [1976] and it was the more general model of Rodi which was adopted in the present study.

Following Rodi [1976], the convection and the diffusion terms were modelled collectively as:

$$\frac{D \overline{u_i u_j}}{Dt} - \mathfrak{D}(\overline{u_i u_j}) = \frac{\overline{u_i u_j}}{k} \left[\frac{Dk}{Dt} - \mathfrak{D}(k) \right] = \frac{\overline{u_i u_j}}{k} (P - \epsilon) \quad (3.3.2.10)$$

where $\mathfrak{D}(\)$ stands for "diffusion of the quantity in parenthesis." The second part of equation (3.3.2.10) results from mere definition. Substituting all the modelling assumptions into equation (3.3.2.1) and rearranging yields

$$e_{ij} = \frac{\overline{u_i u_j}}{k} - \frac{2}{3} \delta_{ij} = \frac{\lambda}{\epsilon} \left\{ (P_{ij} - \frac{2}{3} \delta_{ij} P) + \frac{1}{1-C_2} (\phi'_{ij,1} + \phi'_{ij,2}) \right\} \quad (3.3.2.11)$$

with

$$\lambda = \frac{1 - C_2}{P/\epsilon + (C_1 - 1)}$$

$$P = - \overline{u_i u_j} \frac{\partial U_i}{\partial x_j}$$

and $\phi'_{ij,1}$ and $\phi'_{ij,2}$ given by equations (3.3.2.6) to (3.3.2.8).

It is also necessary to provide a means for the determination of k and ϵ and this was achieved by solving modelled transport equations for both variables. Following Launder et al. [1975], the k and ϵ equations adopted, in cylindrical/rectangular coordinates, are:

$$\begin{aligned} & \frac{1}{r} \frac{\partial}{\partial r} (prU_r k) + \frac{\partial}{r\partial\theta} (\rho U_\theta k) + \frac{\partial}{\partial z} (\rho U_z k) = \rho P - \rho \epsilon \\ & + \frac{1}{r} \frac{\partial}{\partial r} \left\{ \left[\mu + C_{\mu 1} \left(\frac{k}{\epsilon} \right) \overline{u_r u_r} \right] r \frac{\partial k}{\partial r} \right\} + \frac{\partial}{r\partial\theta} \left\{ \left[\mu + C_{\mu 2} \left(\frac{k}{\epsilon} \right) \overline{u_\theta u_\theta} \right] \frac{\partial k}{r\partial\theta} \right\} \\ & + \frac{\partial}{\partial z} \left\{ \left[\mu + C_{\mu 3} \left(\frac{k}{\epsilon} \right) \overline{u_z u_z} \right] \frac{\partial k}{\partial z} \right\} + S_k \end{aligned} \quad (3.3.2.12)$$

$$\begin{aligned} & \frac{1}{r} \frac{\partial}{\partial r} (prU_r \epsilon) + \frac{\partial}{r\partial\theta} (\rho U_\theta \epsilon) + \frac{\partial}{\partial z} (\rho U_z \epsilon) = C_{\epsilon 1} \rho \frac{\epsilon}{k} P \\ & - C_{\epsilon 2} \rho \frac{\epsilon^2}{k} + \frac{1}{r} \frac{\partial}{\partial r} \left\{ \left[\mu + C_{\epsilon 3} \left(\frac{k}{\epsilon} \right) \overline{u_r u_r} \right] r \frac{\partial \epsilon}{\partial r} \right\} \\ & + \frac{\partial}{r\partial\theta} \left\{ \left[\mu + C_{\epsilon 3} \left(\frac{k}{\epsilon} \right) \overline{u_\theta u_\theta} \right] \frac{\partial \epsilon}{r\partial\theta} \right\} + \frac{\partial}{\partial z} \left\{ \left[\mu + C_{\epsilon 3} \left(\frac{k}{\epsilon} \right) \overline{u_z u_z} \right] \frac{\partial \epsilon}{\partial z} \right\} + S_\epsilon \end{aligned} \quad (3.3.2.13)$$

where

$$\begin{aligned}
 P = & - \left\{ \overline{u_r u_r} \frac{\partial U_r}{\partial r} + \overline{u_\theta u_\theta} \left(\frac{\partial U_\theta}{r \partial \theta} + j \frac{U_r}{r} \right) + \overline{u_z u_z} \frac{\partial U_z}{\partial z} \right. \\
 & + \overline{u_r u_\theta} \left(\frac{\partial U_r}{r \partial \theta} + \frac{\partial U_\theta}{\partial r} - j \frac{U_\theta}{r} \right) + \overline{u_r u_z} \left(\frac{\partial U_r}{\partial z} + \frac{\partial U_z}{\partial r} \right) \\
 & \left. + \overline{u_\theta u_z} \left(\frac{\partial U_\theta}{\partial z} + \frac{\partial U_z}{r \partial \theta} \right) \right\}
 \end{aligned}$$

$$\begin{aligned}
 S_k = & \frac{\partial}{\partial r} \left\{ C_{k1} \left(\frac{k}{\epsilon} \right) \left[\overline{u_r u_\theta} \frac{\partial k}{r \partial \theta} + \overline{u_r u_z} \frac{\partial k}{\partial z} \right] \right\} \\
 & + \frac{\partial}{r \partial \theta} \left\{ C_{k1} \left(\frac{k}{\epsilon} \right) \left[\overline{u_r u_\theta} \frac{\partial k}{\partial r} + \overline{u_\theta u_z} \frac{\partial k}{\partial z} \right] \right\} \\
 & + \frac{\partial}{\partial z} \left\{ C_{k1} \left(\frac{k}{\epsilon} \right) \left[\overline{u_r u_z} \frac{\partial k}{\partial r} + \overline{u_\theta u_z} \frac{\partial k}{r \partial \theta} \right] \right\} \\
 & + j C_{k1} \left(\frac{k}{\epsilon} \right) \frac{1}{r} \left[\overline{u_r u_\theta} \frac{\partial k}{r \partial \theta} + \overline{u_r u_z} \frac{\partial k}{\partial z} \right]
 \end{aligned}$$

and

$$\begin{aligned}
 S_\epsilon = & \frac{\partial}{\partial r} \left\{ C_{\epsilon 3} \left(\frac{k}{\epsilon} \right) \left[\overline{u_r u_\theta} \frac{\partial \epsilon}{r \partial \theta} + \overline{u_r u_z} \frac{\partial \epsilon}{\partial z} \right] \right\} \\
 & + \frac{\partial}{r \partial \theta} \left\{ C_{\epsilon 3} \left(\frac{k}{\epsilon} \right) \left[\overline{u_r u_\theta} \frac{\partial \epsilon}{\partial r} + \overline{u_\theta u_z} \frac{\partial \epsilon}{\partial z} \right] \right\} \\
 & + \frac{\partial}{\partial z} \left\{ C_{\epsilon 3} \left(\frac{k}{\epsilon} \right) \left[\overline{u_r u_z} \frac{\partial \epsilon}{\partial r} + \overline{u_\theta u_z} \frac{\partial \epsilon}{r \partial \theta} \right] \right\} \\
 & + j C_{\epsilon 3} \left(\frac{k}{\epsilon} \right) \frac{1}{r} \left[\overline{u_r u_\theta} \frac{\partial \epsilon}{r \partial \theta} + \overline{u_r u_z} \frac{\partial \epsilon}{\partial z} \right] .
 \end{aligned}$$

Equations (3.3.2.12) and (3.3.2.13) are identical to those used for the k - ϵ model, except for diffusion terms which are now approximated without introducing the notion of an isotropic turbulent viscosity, μ_t .

The determination of the model constants appeared in Sections 3.3.1 and 3.3.2 have been made by: 1) available experimental data for simple flows; and 2) computer optimization. For a comprehensive review, see the lecture notes of Launder [1980]. The set of model constants adopted for the present study is listed below:

$$\kappa = 0.4187$$

$$C_\mu = 0.09$$

$$\sigma_k = 1.0$$

$$\sigma_\epsilon = \kappa^2 / (C_{\epsilon 2} - C_{\epsilon 1}) / C_\mu^{1/2}$$

$$C_{\epsilon 1} = 1.44$$

$$C_{\epsilon 2} = 1.92$$

$$C_{\epsilon 3} = 0.36 (C_{\epsilon 2} - C_{\epsilon 1})$$

$$C_{k1} = 0.22$$

$$C_1 = 1.8$$

$$C_2 = 0.6$$

$$C_1' = 0.5$$

$$C_2' = 0.3$$

3.3.3 Summary of the ASM Relations for Flows in a Duct of Square Cross-Section

The ASM outlined in Section 3.3.2 with Cartesian tensor notation is summarized here for both the straight and the curved flow configura-

tions of interest to this study.

The expressions for e_{ij} , P_{ij} , $\phi'_{ij,1}$ and $\phi'_{ij,2}$, when expanded in cylindrical/rectangular coordinates, take the forms given below:

$$e_{rr} = \frac{\overline{u_r u_r}}{k} - \frac{2}{3} - \frac{\lambda}{\epsilon} \left\{ (P_{rr} - \frac{2}{3}P) + \frac{1}{1-c_2} (\phi'_{rr,1} + \phi'_{rr,2}) \right\}$$

$$e_{\theta\theta} = \frac{\overline{u_\theta u_\theta}}{k} - \frac{2}{3} = \frac{\lambda}{\epsilon} \left\{ (P_{\theta\theta} - \frac{2}{3}P) + \frac{1}{1-c_2} (\phi'_{\theta\theta,1} + \phi'_{\theta\theta,2}) \right\}$$

$$e_{zz} = \frac{\overline{u_z u_z}}{k} - \frac{2}{3} = \frac{\lambda}{\epsilon} \left\{ (P_{zz} - \frac{2}{3}P) + \frac{1}{1-c_2} (\phi'_{zz,1} + \phi'_{zz,2}) \right\}$$

$$e_{r\theta} = \frac{\overline{u_r u_\theta}}{k} = \frac{\lambda}{\epsilon} \left\{ P_{r\theta} + \frac{1}{1-c_2} (\phi'_{r\theta,1} + \phi'_{r\theta,2}) \right\}$$

$$e_{rz} = \frac{\overline{u_r u_z}}{k} = \frac{\lambda}{\epsilon} \left\{ P_{rz} + \frac{1}{1-c_2} (\phi'_{rz,1} + \phi'_{rz,2}) \right\}$$

$$e_{\theta z} = \frac{\overline{u_\theta u_z}}{k} = \frac{\lambda}{\epsilon} \left\{ P_{\theta z} + \frac{1}{1-c_2} (\phi'_{\theta z,1} + \phi'_{\theta z,2}) \right\}$$

$$P_{rr} = -2 \left\{ \overline{u_r u_r} \frac{\partial U_r}{\partial r} + \overline{u_r u_\theta} \left(\frac{\partial U_r}{r \partial \theta} - j \frac{U_\theta}{r} \right) + \overline{u_r u_z} \frac{\partial U_r}{\partial z} \right\}$$

$$P_{\theta\theta} = -2 \left\{ \overline{u_\theta u_\theta} \left(\frac{\partial U_\theta}{r \partial \theta} + j \frac{U_r}{r} \right) + \overline{u_r u_\theta} \frac{\partial U_\theta}{\partial r} + \overline{u_\theta u_z} \frac{\partial U_\theta}{\partial z} \right\}$$

$$P_{zz} = -2 \left\{ \overline{u_z u_z} \frac{\partial U_z}{\partial z} + \overline{u_r u_z} \frac{\partial U_z}{\partial r} + \overline{u_\theta u_z} \frac{\partial U_z}{r \partial \theta} \right\}$$

$$P_{r\theta} = - \left\{ \overline{u_r u_r} \frac{\partial U_\theta}{\partial r} + \overline{u_\theta u_\theta} \left(\frac{\partial U_r}{r \partial \theta} - j \frac{U_\theta}{r} \right) + \overline{u_r u_z} \frac{\partial U_\theta}{\partial z} \right. \\ \left. + \overline{u_r u_\theta} \left(\frac{\partial U_\theta}{r \partial \theta} + \frac{\partial U_r}{\partial r} + j \frac{U_r}{r} \right) + \overline{u_\theta u_z} \frac{\partial U_r}{\partial z} \right\}$$

$$P_{rz} = - \left\{ \overline{u_r u_r} \frac{\partial U_z}{\partial r} + \overline{u_z u_z} \frac{\partial U_r}{\partial z} + \overline{u_r u_\theta} \frac{\partial U_z}{r \partial \theta} \right. \\ \left. + \overline{u_r u_z} \left(\frac{\partial U_z}{\partial z} + \frac{\partial U_r}{\partial r} \right) + \overline{u_\theta u_z} \left(\frac{\partial U_r}{r \partial \theta} - j \frac{U_\theta}{r} \right) \right\}$$

$$P_{\theta z} = - \left\{ \overline{u_\theta u_\theta} \frac{\partial U_z}{r \partial \theta} + \overline{u_z u_z} \frac{\partial U_\theta}{\partial z} + \overline{u_r u_\theta} \frac{\partial U_z}{\partial r} + \overline{u_r u_z} \frac{\partial U_\theta}{\partial r} \right. \\ \left. + \overline{u_\theta u_z} \left(\frac{\partial U_z}{\partial z} + \frac{\partial U_\theta}{r \partial \theta} + j \frac{U_r}{r} \right) \right\}$$

$$\Phi'_{rr,1} = c'_1 \left(\frac{\varepsilon}{k} \right) \left\{ \overline{u_z u_z} F - 2 \overline{u_r u_r} G \right\}$$

$$\Phi'_{\theta\theta,1} = c'_1 \left(\frac{\varepsilon}{k} \right) \left\{ \overline{u_r u_r} G + \overline{u_z u_z} F \right\}$$

$$\Phi'_{zz,1} = c'_1 \left(\frac{\varepsilon}{k} \right) \left\{ \overline{u_r u_r} G - 2 \overline{u_z u_z} F \right\}$$

$$\Phi'_{r\theta,1} = c'_1 \left(\frac{\varepsilon}{k} \right) \left\{ -1.5 \overline{u_r u_\theta} G \right\}$$

$$\Phi'_{rz,1} = C'_1 \left(\frac{\epsilon}{k} \right) \left\{ -1.5 \overline{u_r u_z} (F+G) \right\}$$

$$\Phi'_{\theta z,1} = C'_1 \left(\frac{\epsilon}{k} \right) \left\{ -1.5 \overline{u_\theta u_z} F \right\}$$

$$\Phi'_{rr,2} = -C_2 C'_2 \left\{ (P_{zz} - \frac{2}{3} P) F - 2 (P_{rr} - \frac{2}{3} P) G \right\}$$

$$\Phi'_{\theta\theta,2} = -C_2 C'_2 \left\{ (P_{rr} - \frac{2}{3} P) G + (P_{zz} - \frac{2}{3} P) F \right\}$$

$$\Phi'_{zz,2} = -C_2 C'_2 \left\{ (P_{rr} - \frac{2}{3} P) G - 2 (P_{zz} - \frac{2}{3} P) F \right\}$$

$$\Phi'_{r\theta,2} = 1.5 C_2 C'_2 P_{r\theta} G$$

$$\Phi'_{rz,2} = 1.5 C_2 C'_2 P_{rz} (F+G)$$

$$\Phi'_{\theta z,2} = 1.5 C_2 C'_2 P_{\theta z} F$$

where

$$F = \frac{k^{3/2}/\epsilon}{C_w} \left\{ \frac{1}{z} + \frac{1}{D_n - z} \right\}$$

$$G = \frac{k^{3/2}/\epsilon}{C_w} \left\{ \frac{1}{y} + \frac{1}{D_n - y} \right\}$$

and

$$y = (r - r_i)$$

Straight-forward but tedious manipulation of the above expressions result in the following algebraic relations for the six unknowns e_{rr} ,

$e_{\theta\theta}$, e_{zz} , $e_{r\theta}$, e_{rz} and $e_{\theta z}$:

$$\begin{aligned} & e_{rr} \left[-B4 \frac{\partial U_r}{\partial r} - 3A4 - \frac{1}{G_4} \right] + e_{\theta\theta} \left[B5 \left(\frac{\partial U_\theta}{r \partial \theta} + j \frac{U_r}{r} \right) \right] \\ & + e_{zz} \left[B2 \frac{\partial U_z}{\partial z} + 1.5A3 \right] + e_{r\theta} \left[-B4 \left(\frac{\partial U_r}{r \partial \theta} - j \frac{U_\theta}{r} \right) + B5 \frac{\partial U_\theta}{\partial r} \right] \\ & + e_{rz} \left[-B4 \frac{\partial U_r}{\partial z} + B2 \frac{\partial U_z}{\partial r} \right] + e_{\theta z} \left[B5 \frac{\partial U_\theta}{\partial z} + B2 \frac{\partial U_z}{r \partial \theta} \right] \\ & = -2A1 \frac{\partial U_z}{\partial z} + 2(1+2A2) \frac{\partial U_r}{\partial r} + 2A4 - A3 \end{aligned}$$

$$\begin{aligned} & e_{rr} \left[B5 \frac{\partial U_r}{\partial r} + 1.5A4 \right] + e_{\theta\theta} \left[-B6 \left(\frac{\partial U_\theta}{r \partial \theta} + j \frac{U_r}{r} \right) - \frac{1}{G_4} \right] \\ & + e_{zz} \left[B3 \frac{\partial U_z}{\partial z} + 1.5A3 \right] + e_{r\theta} \left[-B6 \frac{\partial U_\theta}{\partial r} + B5 \left(\frac{\partial U_r}{r \partial \theta} - j \frac{U_\theta}{r} \right) \right] \\ & + e_{rz} \left[B5 \frac{\partial U_r}{\partial z} + B3 \frac{\partial U_z}{\partial r} \right] + e_{\theta z} \left[-B6 \frac{\partial U_\theta}{\partial z} + B3 \frac{\partial U_z}{r \partial \theta} \right] \\ & = 2 \left(\frac{\partial U_\theta}{r \partial \theta} + j \frac{U_r}{r} \right) - A3 - A4 - 2A2 \frac{\partial U_r}{\partial r} - 2A1 \frac{\partial U_z}{\partial z} \end{aligned}$$

$$\begin{aligned} & e_{rr} \left[B2 \frac{\partial U_r}{\partial r} + 1.5A4 \right] + e_{\theta\theta} \left[B3 \left(\frac{\partial U_\theta}{r \partial \theta} + j \frac{U_r}{r} \right) \right] \\ & + e_{zz} \left[-B1 \frac{\partial U_z}{\partial z} - 3A3 - \frac{1}{G_4} \right] + e_{r\theta} \left[B2 \left(\frac{\partial U_r}{r \partial \theta} - j \frac{U_\theta}{r} \right) + B3 \frac{\partial U_\theta}{\partial r} \right] \\ & + e_{rz} \left[-B1 \frac{\partial U_r}{\partial z} + B2 \frac{\partial U_z}{\partial r} \right] + e_{\theta z} \left[-B1 \frac{\partial U_z}{r \partial \theta} + B3 \frac{\partial U_\theta}{\partial z} \right] \\ & = 2(1+2A1) \frac{\partial U_z}{\partial z} - 2A2 \frac{\partial U_r}{\partial r} + 2A3 - A4 \end{aligned}$$

$$e_{rr} \left[-B9 \frac{\partial U_\theta}{\partial r} \right] + e_{\theta\theta} \left[-B9 \left(\frac{\partial U_r}{r \partial \theta} - j \frac{U_\theta}{r} \right) \right] + e_{zz} [0]$$

$$+ e_{r\theta} \left[B9 \frac{\partial U_z}{\partial z} - 2.25 A4 - \frac{1}{66} \right] + e_{rz} \left[-B9 \frac{\partial U_\theta}{\partial z} \right]$$

$$+ e_{\theta z} \left[-B9 \frac{\partial U_r}{\partial z} \right] = \frac{2}{3} B9 \left(\frac{\partial U_\theta}{\partial r} + \frac{\partial U_r}{r \partial \theta} - j \frac{U_\theta}{r} \right)$$

$$e_{rr} \left[-B7 \frac{\partial U_z}{\partial r} \right] + e_{\theta\theta} [0] + e_{zz} \left[-B7 \frac{\partial U_r}{\partial z} \right]$$

$$+ e_{r\theta} \left[-B7 \frac{\partial U_z}{r \partial \theta} \right] + e_{rz} \left[-B7 \left(\frac{\partial U_z}{\partial z} + \frac{\partial U_r}{\partial r} \right) - 2.25 (A3 + A4) - \frac{1}{66} \right]$$

$$+ e_{\theta z} \left[-B7 \left(\frac{\partial U_r}{r \partial \theta} - j \frac{U_\theta}{r} \right) \right] = \frac{2}{3} B7 \left(\frac{\partial U_r}{\partial z} + \frac{\partial U_z}{\partial r} \right)$$

$$e_{rr} [0] + e_{\theta\theta} \left[-B8 \frac{\partial U_z}{r \partial \theta} \right] + e_{zz} \left[-B8 \frac{\partial U_\theta}{\partial z} \right]$$

$$+ e_{r\theta} \left[-B8 \frac{\partial U_z}{\partial r} \right] + e_{rz} \left[-B8 \frac{\partial U_\theta}{\partial r} \right] + e_{\theta z} \left[B8 \frac{\partial U_r}{\partial r} - 2.25 A3 - \frac{1}{66} \right]$$

$$= \frac{2}{3} B8 \left(\frac{\partial U_z}{r \partial \theta} + \frac{\partial U_\theta}{\partial z} \right)$$

where

$$A1 = \frac{C_2 C_2'}{1 - C_2} F$$

$$A2 = \frac{C_2 C_2'}{1 - C_2} G$$

$$A3 = \frac{C_2'}{1 - C_2} \left(\frac{\epsilon}{k} \right) F$$

$$A4 = \frac{C_1'}{1-C_2} \left(\frac{\epsilon}{k} \right) G$$

$$GG = \frac{2\lambda k}{3\epsilon}$$

$$B1 = 2(1+2A1) + A2$$

$$B2 = 1 + 2(A1 + A2)$$

$$B3 = 1 + 2A1 - A2$$

$$B4 = 2(1+2A2) + A1$$

$$B5 = 1 + 2A2 - A1$$

$$B6 = 2 + A1 + A2$$

$$B7 = 1.5(1 + 1.5A1 + 1.5A2)$$

$$B8 = 1.5(1 + 1.5A1)$$

$$B9 = 1.5(1 + 1.5A2)$$

CHAPTER 4. NUMERICAL PROCEDURE

4.1 Introduction

In view of the complexity of the governing equations, solutions to the problem are sought via numerical methods. In the present study, the structure and strategy of the TEACH calculation procedure developed at Imperial College [1976] are adopted, with major modifications to take advantages of the partially-parabolic nature of the flow. Section 4.2 introduces the concept of partially-parabolic flow and discusses the consequence of this classification in terms of the describing equations. Section 4.3 details the discretization practices. Section 4.4 summarizes the boundary conditions for the calculations. Finally, Section 4.5 outlines the solution algorithm.

4.2 Partially-Parabolic Flows

There are primarily three mechanisms which transmit local disturbances to other points of a flow: convection, molecular diffusion and pressure waves. Strictly speaking, all steady subsonic flows are elliptic in the sense that perturbations at a point can influence the flow state at any other point. A solution to this type of problem requires the specification of boundary conditions on a closed boundary of the flow domain. From a computational point of view, however, two additional classifications are possible: parabolic flows and partially-parabolic flows.

In terms of the three mechanisms mentioned above, a flow situation is classified as being partially-parabolic if along a certain direction the only means for transmitting local disturbances upstream is through the pressure field; there must be no flow reversal and diffusion should be negligible along the "partially-parabolized" direction.

The flow configuration of interest to the present study falls into the category of partially-parabolic flows as long as the bend is not so tight as to render flow reversal along the main flow direction. The problem of a deflected jet or a jet in a crosswind flow, as studied by Bergeles [1976], can also be classified as pertaining to the partially-parabolic category.

The immediate consequence of this "partial-parabolization" is that all the underlined terms in the equations presented in Chapter 3 are assumed negligible and so were neglected in the calculations. The validity of this simplification was checked by Humphrey et al. [1981] for turbulent flow in a square duct of strong curvature. It was found from their calculation that the longitudinal diffusion was no larger than 2% of the longitudinal convection. It would appear, therefore, that a partially-parabolic procedure accounting for strong pressure variations could provide more precise results through increased grid refinement.

Since all transport equations given in Chapter 3 share the same general form

$$\frac{1}{r} \frac{\partial}{\partial r} (r U_r \phi) + \frac{\partial}{\partial \theta} (U_\theta \phi) + \frac{\partial}{\partial z} (U_z \phi) = \frac{1}{r} \frac{\partial}{\partial r} (r \Gamma \frac{\partial \phi}{\partial r}) + \frac{\partial}{\partial z} (\Gamma \frac{\partial \phi}{\partial z}) + S_\phi \quad (4.2.1)$$

with S_ϕ including all the remaining terms, the following discussions on discretization will be based upon equation (4.2.1).

4.3 Discretization

The first step toward discretization is the arrangement of a convenient grid system. For the present study, a staggered grid was adopted as shown in Figures 4.1 and 4.2. This choice minimizes the amount of interpolation needed and improves stability. The locations of the Reynolds shear stresses were also staggered to the places as indicated in these figures.

Following the standard approach of TEACH-type codes, equation (4.2.1) is integrated over a control volume chosen for the variable ϕ . Using central differencing for the diffusion terms, the integrated form of equation (4.2.1), with all the subscripts and dimensions referred to Figure 4.3, becomes

$$C_e \phi_e - C_w \phi_w + C_n \phi_n - C_s \phi_s + C_d \phi_d - C_u \phi_u = D_e (\phi_E - \phi_P) \\ - D_w (\phi_P - \phi_W) + D_n (\phi_N - \phi_P) - D_s (\phi_P - \phi_S) + \overline{S_\phi} \Delta V$$

where

$$C_e = (r \Delta r \Delta \theta)_e (\rho U_z)_e$$

$$C_w = (r \Delta r \Delta \theta)_w (\rho U_z)_w$$

$$C_n = (r \Delta z \Delta \theta)_n (\rho U_r)_n$$

$$C_s = (r \Delta z \Delta \theta)_s (\rho U_r)_s$$

$$C_d = (\Delta r \Delta z)_d (\rho U_\theta)_d$$

$$C_u = (\Delta r \Delta z)_u (\rho U_\theta)_u$$

$$D_e = (r \Delta r \Delta \theta)_e \Gamma_e / (\delta z)_e$$

$$D_w = (r \Delta r \Delta \theta)_w \Gamma_w / (\delta z)_w$$

$$D_n = (r \Delta z \Delta \theta)_n \Gamma_n / (\delta r)_n$$

$$D_s = (r \Delta z \Delta \theta)_s \Gamma_s / (\delta r)_s$$

$$\Delta V = (r \Delta r \Delta \theta \Delta z)$$

and

$$\bar{S}_\theta = \frac{1}{\Delta V} \int S_\theta r dr d\theta dz$$

The source term $\overline{S\phi} \Delta V$ may be conveniently separated into two parts as $S_p \phi_p + S_U$ in order to take full advantage of the solution algorithm. A more elaborate discussion of this practice and its benefits will be found in Patankar [1980].

For the convection terms, a proper approximation of the ϕ 's at the control-volume surfaces has been proven to be crucial to the stability of the solution algorithm. The accuracy of the calculated results also depends strongly on the way these terms are simulated. A brief outline is given next of the schemes chosen for the present study.

1 For ϕ_d and ϕ_u which stem from convection along the main flow direction, upwind differencing was invariably used with $\phi_d = \phi_p$ and $\phi_u = \phi_p^o$ where ϕ_p^o stands for the value of ϕ_p at the adjacent upstream station. This choice is in line with the notion of a partially-parabolic flow in that, along this direction, there is no flow reversal and that diffusion is negligible.

2 For ϕ_e , ϕ_w , ϕ_n and ϕ_s over a cross-stream plane, two types of approximations were used: the central/upwind (HYBRID) scheme and the quadratic upwind-weighted interpolation (QUICK) scheme.

HYBRID: This scheme, first proposed by Spalding [1972], is based on an approximation to the exact solution of the one-dimensional convection-diffusion equation

$$\frac{d}{d\xi} (\rho U \phi - \Gamma \frac{d\phi}{d\xi}) = 0$$

between two points with known ϕ 's. It employs upwind differencing where

the flow is convection-dominated and shifts to central differencing otherwise. The determining parameter is the local Peclet number defined as $Pe = \rho U_{\xi} \Delta \xi / \Gamma$; the flow is considered to be convection-dominated if $|Pe| > 2$. Thus, in terms of an approximation for ϕ_e , the HYBRID scheme yields

$$\begin{aligned} \phi_e &= \frac{1}{2} (\phi_E + \phi_P) && \text{if } |Pe| \leq 2 \\ \phi_e &= \phi_P && \text{if } Pe > 2 \\ \phi_e &= \phi_E && \text{if } Pe < -2. \end{aligned}$$

Similar expressions can easily be constructed for the ϕ 's at the other control-volume surfaces. Note that when upwind differencing is used at the condition of convection-dominance, diffusion at the corresponding cell surface is neglected.

It has long been known that upwind schemes, while removing the stability problems associated with central differencing schemes, may introduce severe numerical diffusion arising primarily from streamline-to-grid skewness. This unphysical diffusion can cause serious difficulties for turbulence modelers who, in order to evaluate the performance of turbulence models, need to eliminate from their computations all the inaccuracies and uncertainties due to the finite difference practices. Alternatives to the HYBRID scheme have been proposed and tested in the literature, see Huang, Launder and Leschziner [1983] for a brief review.

QUICK: In an attempt to overcome the numerical diffusion problems associated with upwind schemes and to combine the accuracy of central differencing with the stability of upwind differencing, Leonard [1979] proposed a three-point, upwind-weighted quadratic interpolation to approximate the ϕ 's at the control-volume surfaces. The proper formulae

for, say, ϕ_e are

$$\phi_e = \frac{1}{2}(\phi_E + \phi_P) + \alpha_e \phi_P + \beta_e$$

$$\text{where } \alpha_e = \begin{cases} \delta_i(1 + \delta_i/\delta_{i-1})/8\Delta_i & \text{if } C_e > 0 \\ -\delta_i/8\Delta_{i-1} & \text{if } C_e < 0 \end{cases}$$

$$\text{and } \beta_e = \begin{cases} -(\delta_i)^2(\phi_E/\delta_i + \phi_W/\delta_{i-1})/8\Delta_i & \text{if } C_e > 0 \\ -(\delta_i)^2(\phi_{EE} - \phi_E)/\delta_{i+1} - \phi_E/\delta_i/8\Delta_{i+1} & \text{if } C_e < 0 \end{cases}$$

with symbols and dimensions defined in Figure 4.4. Formulae appropriate for ϕ 's at other surfaces are summarized in Table 4.1. Details of the QUICK scheme can be found in Leonard [1979] and of its performance in Han et al. [1981] and Huang et al. [1983].

With the formulae given above and the difference form of the continuity relation

$$C_d = C_u + C_s - C_e + C_w - C_n,$$

equation (4.3.1) may be written as

$$a_p \phi_P = a_N \phi_N + a_S \phi_S + a_E \phi_E + a_W \phi_W + a_U \phi_P^o + S_U + Q_U \quad (4.3.2)$$

where

$$a_p = a_N + a_S + a_E + a_W + a_U - S_p - Q_p$$

and the a 's denote the combined contributions of convection and diffusion at the control volume surfaces to the balance of ϕ_P at the cell center.

Depending upon the differencing scheme chosen for the ϕ 's over a cross-stream plane, the expressions for a 's, Q_U and Q_p take the different

forms given below.

For the HYBRID scheme:

$$a_E = \left[\left[-C_e, D_e - \frac{C_e}{2} \right], 0 \right]$$

$$a_W = \left[\left[C_w, D_w + \frac{C_w}{2} \right], 0 \right]$$

$$a_N = \left[\left[-C_n, D_n - \frac{C_n}{2} \right], 0 \right]$$

$$a_S = \left[\left[C_s, D_s + \frac{C_s}{2} \right], 0 \right]$$

$$a_U = C_u$$

$$Q_P = Q_U = 0$$

where [] stands for "the largest quantities compared".

For the QUICK scheme:

$$a_N = D_n - \frac{1}{2} C_n$$

$$a_S = D_s + \frac{1}{2} C_s$$

$$a_E = D_e - \frac{1}{2} C_e$$

$$a_W = D_w + \frac{1}{2} C_w$$

$$a_U = C_u$$

$$Q_P = C_w \alpha_w - C_e \alpha_e + C_s \alpha_s - C_n \alpha_n$$

$$Q_U = C_w \beta_w - C_e \beta_e + C_s \beta_s - C_n \beta_n$$

Equation (4.3.2) represents the general form of the finite difference equation to be solved. The solution procedure adopted for the present study will be outlined after a brief description in the next section of the boundary conditions prescribed numerically.

4.4 Numerical Prescriptions of Boundary Conditions

Symmetry of the flow configuration with respect to the plane $z = 0$ allowed the performance of calculations over one symmetrical half of the duct cross-section. The specification of required boundary conditions is summarized below.

At the inlet plane, which is chosen at $5 D_H$ upstream of the bend section, U_x , U_y , $\overline{u_x^2}$, $\overline{u_y^2}$ and $\overline{u_x u_y}$ were interpolated from measurements at the same station; U_z , $\overline{u_z^2}$ and $\overline{u_x u_z}$ were deduced from symmetry considerations; and, in the absence of any reliable information, $\overline{u_x u_z}$ was set to zero. The distribution of ϵ was prescribed by setting

$$\epsilon = C_\mu^{3/4} k^{3/2} / \ell_m$$

with ℓ_m , the mixing length, found from a generalization of the straight pipe formula of Nikuradse [1932] to a square duct geometry. The formula used was

$$\ell_m = \kappa D_H [\beta_z (1 - 1.2 \beta_z) \cdot \beta_y (1 - 1.2 \beta_y)]^{1/2}$$

with

$$\beta_z = \frac{z}{D_H} \left(1 - \frac{z}{D_H}\right) \quad \text{and} \quad \beta_y = \frac{y}{D_H} \left(1 - \frac{y}{D_H}\right)$$

At the exit plane, chosen at $5 D_H$ downstream of the bend exit, $\partial U_x / \partial x = 0$ was imposed.

Along the symmetry plane at $z = 0$, the derivatives of U_x , U_y , P , k and ϵ as well as U_z itself were set to zero.

At solid walls, the wall-function approach outlined in Launder and

Spalding [1974] was adopted. This, in essence, consists in specifying boundary conditions near the walls rather than at the walls. The first calculation node, P, is placed at a distance y_p away from a wall in a region where the logarithmic law of the wall prevails and in which the turbulence is in a state of local equilibrium and the shear stress τ_p is approximately equal to that of the wall, τ_w . Within this equilibrium layer, it can be shown that

$$\tau_w = \kappa \rho C_\mu^{1/4} k_p^{1/2} U_p / \ln(E y_p C_\mu^{1/4} k_p^{1/2} / \nu)$$

$$k_p = U_\tau^2 / C_\mu^{1/2} \quad \text{and} \quad \epsilon_p = U_\tau^3 / \kappa y_p$$

where

$$U_\tau = (\tau_w / \rho)^{1/2} \quad \text{and} \quad E = 9.793 .$$

These were the conditions imposed near wall. Since there are no reliable experimental correlations for the form of the law of the wall, if exists at all, for complex, three-dimensional skewed boundary layer flows, the lateral velocities U_r and U_z were assumed to follow the same logarithmic relation as that for U_θ outlined above.

4.5 Solution Algorithm

In the present study the elliptic numerical procedure of Humphrey [1977] was modified, according to the guidelines of Prataap [1975], to perform partially-parabolic calculations. The pertinent features of the solution algorithm are:

1. Calculation is performed by marching through the flow domain along

the main flow direction as many times as is required for a predetermined convergence criterion to be achieved.

2. The pressure distribution is always stored in a three-dimensional array for the entire flow field so that it can be corrected and updated during each sweep of the flow domain.
3. The remaining flow variables are continuously recalculated and are stored temporarily in two-dimensional arrays at the current computing station and, for velocity components only, at the corresponding upstream station. Because of this practice, nonlinear convection terms in the momentum equations are linearized with respect to their values at the upstream station (rather than their values at the current station from the previous sweep).
4. The hydrodynamic variables are solved by a slightly modified version of the SIMPLE procedure. For a detailed account of the SIMPLE procedure, see Patankar [1980].
5. The discretized equations are solved by a line-by-line iterative procedure--the tridiagonal matrix algorithm (TDMA).

The major calculation steps are summarized below:

1. Assign initial guessed values to the pressure field.
2. Solve the momentum equations for the cross-stream velocity components U_r and U_z .
3. Solve the U_θ momentum equation. Note that U_θ is located ahead of the plane containing U_r and U_z (see Figure 4.2).
4. Update the pressure and velocity distributions according to the modified SIMPLE algorithm.
5. Solve the remaining transport equations (k and ϵ).

6. Calculate the Reynolds stresses from the ASM relations (ASM only).
7. March to the next downstream station and repeat Steps 2 to 6 until the exit plane of the calculation domain is reached.
8. Repeat Steps 2 to 7 with the most recent, more correct pressure distribution as the new initial guess until convergence is achieved.

The immediate advantage of the partially-parabolic procedure over the elliptic one is that the storage requirement for the same grid density is drastically reduced for the former. Due to this tremendous savings on computer memory, it becomes, in principle, feasible to compute three-dimensional flows on a grid system refined enough to render numerical diffusion an insignificant portion of the numerical accuracy. For a more detailed exposition of the partially-parabolic procedure, see the Ph.D. dissertation of Pratap [1975].

CHAPTER 5. VALIDATION

5.1 Introduction

The finite-difference forms of the governing equations, together with the appropriate boundary conditions were coded, following the guidelines of Pratap [1975], into a computer program which solves three-dimensional, partially-parabolic flows in cylindrical/rectangular coordinates. Prior to predicting the main flow of interest to the present study, rigorous testing was performed against several flows with either known analytical or reliable numerical solutions or generationally accepted experimental information.

The purpose of testing was twofold:

1. To check the correctness of the procedure.

The present algorithm was obtained by modifying the elliptic procedure of Humphrey [1977]. In order to ensure that the modifications had been carried out properly, predictions of laminar flows in the following geometries were performed:

- i two-dimensional straight channel;
- ii two-dimensional curved channel;
- iii straight duct of square cross-section with one wall moving at a constant speed normal to the main flow direction;
- iv 90° bend of square cross-section with a long straight duct preceding it.

The results of the testing are summarized and discussed in Section 5.2.

2. To evaluate the performance of the $k-\epsilon$ model and the ASM closures adopted for this study.

Numerous examples of predictions obtained with these two models have already been published in the literature (see, for example, the review of Rodi [1978]). The present tests were conducted to ensure that there were no coding errors in the portion of the program concerning the turbulence models and, more importantly, to evaluate the performance of these models within the framework of a partially-parabolic procedure. The test geometries selected were a two-dimensional straight channel and a two-dimensional curved channel. The results of these turbulent flow tests will be discussed in Section 5.3.

5.2 Laminar Flow Tests

In this section, the four laminar flow test cases are described and their results briefly discussed. The two-dimensional flow tests of *i* and *ii* were predicted by imposing two symmetry conditions along the third (*z*) direction of the three-dimensional code. Calculations of cases *i*, *ii* and *iii* were carried out by using a plug flow profile as the inlet condition, whereas a fully developed velocity profile was imposed at the inlet plane in case *iv*.

Case i Developing flow in a two-dimensional straight channel

A HYBRID scheme calculation on a ($y = 17$) \times ($x = 101$) equally spaced grid was performed over a symmetrical half of the channel. As shown in Figure 5.1 the calculated fully developed velocity profile follows the analytical solution almost identically, with the maximum

deviation, which occurs at the first node next to the channel wall, being less than 2%.

Case ii Developing flow in a two-dimensional strongly curved channel.

In order to test the appropriateness of the concept of partially-parabolic flows, a strongly curved channel was purposefully chosen. Figure 5.2 shows the calculated fully developed velocity distribution as compared to the exact solution (Goldstein [1965]). Agreement is excellent and the maximum deviation from the analytical solution, which occurs at the first node next to the inner wall at $r = r_i$, is less than 3.5%. This calculation was performed with the HYBRID scheme using a $(r = 22) \times (\theta = 183)$ uniformly spaced grid.

Case iii Developing flow in a straight duct of square cross-section with one wall sliding normal to the main flow direction at a constant speed.

This flow was calculated with both the HYBRID and the QUICK schemes on an equally spaced grid of $(y = 15) \times (z = 15) \times (x = 121)$. The calculation of Burggraf [1966] was chosen as the standard for comparison. Figure 5.3 demonstrates clearly the superiority of the QUICK scheme over the HYBRID scheme. In fact, a calculation with the QUICK scheme using a $(y = 8) \times (z = 8) \times (x = 121)$ grid produced results similar to those generated in the aforementioned HYBRID calculation.

Case iv Flow in a 90° bend of square cross-section with fully developed velocity profile close to the inlet of the bend.

The particular flow calculated corresponds to the measurements of Humphrey et al. [1981] at $Re = 790$ and $De = 368$. Both the HYBRID and

the QUICK schemes were used on a $(r = 17) \times (z = 11) \times (\theta = 36)$ uniformly spaced grid. The agreement with measurements was generally very good at bend angles of 0° , 30° and 90° , with discrepancies of U_θ up to 30% being found at $\theta = 60^\circ$. Figure 5.4 compares the calculated longitudinal velocity profiles at $Z = 0.5 D_H$ and $\theta = 90^\circ$ (refer to Figure 2.1 for coordinate system) with experimental results. The QUICK scheme calculation again yielded better overall agreement with the measured data.

5.3 Testing of Turbulence Models

The laminar flow tests presented in the previous section have demonstrated the applicability of the partially-parabolic procedure for predicting internal flows of characteristics similar to the present study. This section provides further validation on the turbulence models used.

Case i Flow in a two-dimensional straight channel.

This is the simplest possible, yet very informative test that can be performed by using the current computer program with minor modifications. For the purpose of comparison, the experiment of Laufer [1950] at $Re = 123,200$ was simulated on an unequally spaced grid of $(y = 18) \times (x = 241)$ over a symmetrical half of the channel. Following the experimental correlation of Laufer, the log-wall constants of $\kappa = 0.33$ and $E = 6.14$ were used instead.

Figures 5.5 and 5.6 show the calculated distributions, using $k-\epsilon$ model, of the mean longitudinal velocity, U_x , and the turbulence energy, k , as compared with the experimental measurements. A preliminary check

on the "correctness" of the ASM was made by substituting the calculated values of U_x , k and ϵ into the ASM relations given in Section 3.3.3 and solving for the Reynolds stresses. It can be seen from Figure 5.7 that, assuming U_x , k and ϵ as calculated by the k - ϵ model were correct, the ASM closure is capable of predicting broadly satisfactory distributions of the Reynolds stresses.

Direct computation using the ASM closure, however, yielded mean velocity and Reynolds stresses in poor agreement with the measurements. In particular, the level of $\overline{u_z u_z}$ was twice as high compared to the data. The alternative approach of employing the isotropic k and ϵ equations [equations (3.3.1.11) and (3.3.1.12)], as has been done by many of the ASM users, produced better results. Figures 5.8 to 5.10 show that the general trend of the predictions were satisfactory, with the most serious discrepancies being:

1. Very close to the wall the value of $\overline{u_x u_x}$ falls off instead of rising as suggested by the data.
2. The differences between $\overline{u_y u_y}$ and $\overline{u_z u_z}$ are too large.

In order to check the sensitivity of the model to the model constants, a further run with $C_1' = 0.35$ and $C_2' = 0.20$ was carried out. Figures 5.8 to 5.10 show that better agreement was achieved with the new constants, especially for the distributions of $\overline{u_y u_y}$ and U_x . Since the same change of C_1' and C_2' did not produce appreciable overall improvement in the 2D curved channel case, the originally recommended values of $C_1' = 0.5$ and $C_2' = 0.3$ were used in the final computations described in Chapter 6.

Case ii Flow in a two-dimensional curved channel.

The development of turbulent shear flows on curved surfaces is characterized by a strong sensitivity of the turbulence structure to streamline curvature (Bradshaw [1973]). Attempts to predict such flows by using eddy viscosity transport closures, such as the $k-\epsilon$ model, have not been very successful unless empirical means to account for curvature effects are incorporated into the models. Approaches of this type have been reported by, among others, Launder et al. [1977] and Humphrey and Pourahmadi [1982] with some success for moderately curved channels. It is argued (Gibson [1978]) that only turbulence models based upon the calculation of Reynolds stresses directly from their transport equations can account for the streamline curvature effects correctly.

In order to test the capability of the ASM closure for predicting the curvature effects mentioned above, the measurements of Eskinazi and Yeh [1956] in a curved rectangular duct of large aspect ratio was simulated on a $(r = 24) \times (\theta = 184)$ unequally spaced grid. Figures 5.11 and 5.12 compare the calculated (HYBRID scheme only) distributions of U_θ , $\overline{u_\theta u_\theta}$, $\overline{u_r u_r}$ and $\overline{u_r u_\theta}$ with the experimental data. While the ASM closure tends to overpredict the turbulence intensities $\overline{u_\theta u_\theta}$ and $\overline{u_r u_r}$ near the convex (stabilizing) wall and underpredict the values of U_θ and $\overline{u_r u_\theta}$ near the concave (destabilizing) wall, predictions are, in general, in good agreement with the data of Eskinazi and Yeh.

The idea of using a non-symmetric wall-proximity function f [equations (3.3.2.6)-(3.3.2.8)], first proposed by Humphrey and Pourahmadi [1982], was also tested. This correction produced very little changes

on the distribution of $U_\theta/U_{\theta,\max}$ and its effect on $\overline{u_\theta u_\theta}$ and $\overline{u_r u_r}$ is shown in Figures 5.11 and 5.12. Since this non-symmetric f-function did not yield results in better overall agreement with the data, the original (symmetric) f-function [equation (3.3.2.8)] was retained.

CHAPTER 6. RESULTS AND DISCUSSION

6.1 Introduction

In this chapter, detailed measurements of developing turbulent flow in a square cross-section 180° bend and its upstream and downstream tangents are presented and discussed. These data are compared with corresponding predictions by both the $k-\epsilon$ model and the algebraic stress model at selected streamwise stations. Section 6.2 considers the measurements and the $k-\epsilon$ model predictions. Both the HYBRID and the QUICK schemes were used in the calculations. When QUICK and HYBRID results coincide, a single profile is shown in the figures. Otherwise, HYBRID results are plotted as continuous lines and QUICK as dashed lines. It should be noted that dashed lines have also been used in some graphs for plotting best fits to experimental data with a larger than normal degree of scatter at the $2z/D_H = 0.75$ and 0.875 spanwise locations. Section 6.3 presents the predictions with the ASM closure. Since it has not been successful in producing converged results with QUICK scheme at the time of writing, only HYBRID calculations are included. Two simplified "experimental" tests of the ASM closure are also presented in this section.

6.2 Turbulent Flow Measurements and the $k-\epsilon$ Model Calculations

The calculation presented in this section was performed on an unequally spaced grid consisting of the following distributions of nodes:

($z = 14$) \times ($r = 25$) \times ($\theta = 45$) in the bend, and ($z = 14$) \times ($r = 25$) \times ($x = 20$) in the upstream and downstream tangents, both of length $5 D_H$. The grid distribution over a cross-stream plane is listed in Table 6.1. The convergence criterion was that the maximum of the normalized residual summations at every cross-sectional plane be less than 10^{-3} .

Measurements of the flow in the upstream tangent, taken at $X_H = -5$ and -1 are shown in Figures 6.3 and 6.4 respectively. Comparing the data at these two stations, particularly the Reynolds stress measurements shown in Figure 6.14, suggests that the flow is still developing at $X_H = -5$, after travelling a distance of $30 D_H$ from the uniformizing section. Figures 6.2 and 6.14 provide comparisons of the measurements at $X_H = -1$ with corresponding profiles interpolated from the data obtained by Melling and Whitelaw [1976] at 36.8 hydraulic diameters in a straight duct of square cross-section. The two data sets are in agreement to within the experimental error of the measurements. Since the measurements by Melling and Whitelaw correspond to an essentially developed flow, the differences shown in Figure 6.2 for the radial (transverse) velocity component are attributed mainly to the elliptic influence of the bend on the flow in the tangent. Similar observations on the influence of a bend on its upstream tangent flow have been noted by Humphrey et al. [1981] and Taylor et al. [1982] in the same 90° bend configuration but with differing inlet conditions. Taylor et al. found that in a turbulent flow with relatively thin boundary layers the bend influenced the measurements taken at $X_H = -0.75$, their furthest upstream location. Measurements at $X_H = -2.5$ taken by Humphrey et al. with essentially fully developed flow conditions in the upstream tangent suggested

only a weak elliptic effect of the bend on the flow at this location. However, these authors did not measure the transverse velocity component; their commentary is based on the unchanged appearance of streamwise velocity and turbulence intensity contours between $X_H = -1$ and $X_H = -2.5$. By contrast, for the conditions of the present experiment, the velocity data suggests that the favorable streamwise pressure gradient along the inner wall of the bend (see Figure 6.1) induces a mean transverse flow directed at the inner wall which is already noticeable at $X_H = -5$. Although weak ($U_r/U_B \approx 0.02$), it appears that the transverse flow induced by pressure forces in the upstream duct overcomes the weaker stress-driven cross-stream motion (shown clearly in the measurements of Melling and Whitelaw), and results in U_r profiles whose shapes, and variations of shape with z location, agree qualitatively with a simple superposition of the pressure-induced and stress-driven cross-stream flows.

Calculations of U_r at $\theta = 3^\circ$ (and between this location and $X_H = -5$, not given here) always showed the flow moving towards the convex wall-side of the test section. Because the turbulence model is insensitive to stress-driven secondary motions, this result, and the calculated displacement of the maximum in U_θ towards the convex wall, clearly support the experimental finding that elliptic effects are transmitted from the bend into the upstream tangent via the pressure field, farther than has previously been observed. As with the U_r velocity component, the discrepancies shown between calculated and measured turbulent stresses at $\theta = 3^\circ$ arise from the assumption of isotropy in the turbulence model. To predict more accurately the cross-stream motion and

turbulent stresses in the upstream tangent requires modeling of important anisotropic flow characteristics such as near-wall pressure-strain effects. These effects cannot be dealt with by isotropic viscosity models of any kind.

The mean velocity and turbulent stress data taken at different streamwise locations in the bend are plotted in Figures 6.5-6.9 and 6.15. The pressure drop measured at the side wall of the bend is shown in Fig. 6.1. In general, the sense of the flow up to $\theta = 90^\circ$ is in agreement with earlier observations of, for example, Humphrey et al. [1981] and Taylor et al. [1982]. Closer inspection of the plots reveals additional interesting features. The measurements of the pressure coefficient C_p show the opposing pressure gradient initially expected at the concave wall and the favorable gradient at the convex. In contrast to the data measured by Taylor et al. for a 90° bend, the maximum and minimum values of C_p do not coincide at the same streamwise location. In this work the value of C_p maximizes at the concave wall at $\theta \approx 45^\circ$, and attains its minimum value at the convex wall at $\theta \approx 177^\circ$. As of $\theta \approx 45^\circ$, the streamwise pressure gradient is favorable throughout most of the bend. At $\theta \approx 3^\circ$ the streamwise velocity profiles all shown their maximum values displaced towards the inner radius wall, due to the favorable streamwise pressure gradient there. The radial component of velocity is everywhere directed towards the inner wall except for a small flow region about the symmetry plane. This region marks the inception of secondary flow, driven by the transverse pressure gradient which arises due to lateral curvature of the main flow in the bend. The secondary flow is more intense at $\theta = 45^\circ$ as shown in Figure 6.6. At $\theta = 45^\circ$,

the profile for U_r near the side wall ($2z/D_H = 0.75$) shows a large negative velocity, while the profiles at the other z locations are large and positive. The sense of motion is from the convex to the concave surface along the symmetry plane, and back to the convex surface along the side walls of the bend. As of $\theta = 45^\circ$, measurements of U_r at all z locations show this component always positive (directed from the convex to the concave surface). This means that the cross-stream plane return flow adjacent to a flat wall in the bend is confined to a narrow region less than $D_H/8$ in width. A simplified mass balance at $\theta = 90^\circ$ suggests that the radial component of velocity in this narrow region varies between 0 at the wall and a maximum of about $0.40 \times U_B$ at the peak location. This result is in qualitative agreement with the observations of Taylor et al. [1982]. The highest return flow measured by them ($0.40 \times U_B$) was found at $2z/D_H = 0.95$ and $\theta = 60^\circ$ in a 90° bend with $Re = 40,000$ and $R_C/D_H = 2.3$. Calculations of the present flow gave a peak value of $U_r/U_B = 0.30$ at $2z/D_H = 0.95$, at the 90° plane.

Between $\theta = 3^\circ$ and 90° , the influence of destabilizing curvature raises the levels of all the measured Reynolds stresses at the concave wall of the bend. The effect is particularly noticeable in the plots for the stresses at $\theta = 45^\circ$, and has decreased by the time the flow reaches the $\theta = 90^\circ$ plane. Similar observations have been made by Eskinazi and Yeh [1956] in a two-dimensional curved channel flow, and by Humpnrey et al. [1981] and Taylor et al. [1982] in their respective curved duct flows. In particular, Eskinazi and Yeh demonstrate the strong generation of $\overline{u_r^2}$ near a concave wall and its correspond suppression near a convex wall. While at $\theta = 45^\circ$ the present flow is already three-

dimensional, the results for \bar{u}_r/U_B are in qualitative agreement with the observations of Eskinazi and Yeh. Destabilizing and stabilizing curvature effects at the respective concave and convex walls of the present flow are responsible for producing large levels of anisotropy. For example, at $\theta = 45^\circ$, $\overline{u_\theta^2}/\overline{u_r^2} \approx 2$ near the concave wall. Wall-dampening of radial fluctuations in the flow, coupled with pressure redistribution and turbulent diffusion of energy between the normal stresses, account for the larger levels of $\overline{u_\theta^2}$.

At $\theta = 90^\circ$ and 130° , plots of the two velocity components and their corresponding normal stresses show striking variations in the radial coordinate direction. These take the form of relatively large decelerations in the mean flow components at about $\eta = 0.4$ and are accompanied by relatively large increases in \bar{u}_θ and decreases in \bar{u}_r respectively at the same locations. The streamwise deceleration of U_θ and U_r is due to the "pumping" of low speed fluid from the peripheral region of the duct into the core of the flow. Whereas viscous effects provide the mechanism for flow retardation at the walls, it is the inviscid mechanism of lateral flow curvature which drives the cross-stream motion. The phenomenon has been analyzed and described in depth by Hawthorne [1951], and Horlock and Lakshminarayana [1973] discuss it extensively in the context of turbomachinery aerodynamics. In particular, the latter authors provide general expressions for the generation of streamwise vorticity including the influence of Bernoulli surface rotation and viscous effects. Hawthorne shows that in flows where the angle, ϕ , between the direction of normal acceleration and the normal to the Bernoulli surface (a surface of constant total pressure) is not 0, streamwise

vorticity is induced. For a small bend deflection angle θ in a flow with initial uniform vorticity Ω_0 in the plane of the bend, the expression derived by Hawthorne [1951] is:

$$\xi_\theta = -2 \Omega_0 \theta$$

The same result was obtained by Squire and Winter [1951] using a different analytical approach and is valid for Bernoulli surfaces which remain undisturbed during passage through bend ($\phi = \text{constant}$).

It is important to realize that the inviscid mechanism acts over the entire cross-section of the flow (provided $\phi \neq 0$). For the kind of flow of interest here, the distortion of Bernoulli surfaces during passage of the flow around the bend cannot be neglected. A first approximation accounting for this distortion leads to an equation for α , the angle by which the Bernoulli surfaces turn. The result derived by Hawthorne [1951] is:

$$\left(\frac{D_H}{R_C}\right) \frac{d^2 \alpha}{d\theta^2} = \cos \alpha$$

This equation is analogous to that governing the motion of a pendulum and, as shown by Hawthorne, predicts that the flow through a bend should oscillate between $\alpha = 0$ and $\alpha = \pi$ with a period (or bend angle) for a complete oscillation approximately equal to $2\pi/\sqrt{R_C/D_H}$. The secondary motion is analogous to the kinetic energy of the pendulum and also oscillates with the same period, passing through zero after each $\pi\sqrt{D_H/R_C}$ radians of turn. For the present flow a complete oscillation corresponds to about 197° . This means that at about 98° the inviscid mechanism

starts working to *oppose* the original sense of the cross-stream motion, with a maximum negative amplitude at $\theta = 148^\circ$. The result, as shown in Figures 6.8 and 6.9 for $\theta = 130^\circ$ and 177° , is for high speed fluid to be restored to the core of the flow.

For $\theta = 90^\circ$ and 130° , plots of the Reynolds stresses show large changes at the radial positions where U_θ and U_r have been decelerated. Transport equations for the turbulent stresses can be obtained (Bryant and Humphrey [1976]), and for $\overline{u_\theta^2}$ and $\overline{u_r^2}$ they take the forms given below:

$$\frac{D}{Dt} \left(\frac{\overline{u_\theta^2}}{2} \right) = - \overline{u_\theta u_r} \frac{\partial U_\theta}{\partial r} - \overline{u_\theta^2} \left(\frac{1}{r} \frac{\partial U_\theta}{\partial \theta} + \frac{U_r}{r} \right) - \overline{u_\theta u_z} \frac{\partial U_\theta}{\partial z} + P_\theta^S + D_\theta \quad (6.2.1)$$

$$\frac{D}{Dt} \left(\frac{\overline{u_r^2}}{2} \right) = - \overline{u_r^2} \frac{\partial U_r}{\partial r} + \overline{u_\theta u_r} \left(\frac{U_\theta}{r} - \frac{1}{r} \frac{\partial U_r}{\partial \theta} \right) - \overline{u_r u_z} \frac{\partial U_r}{\partial z} + P_r^S + D_r \quad (6.2.2)$$

In the above equations, P_θ^S and P_r^S represent pressure strain redistribution terms, D_θ and D_r denote the effects of turbulent diffusion and dissipation, and viscous diffusion is neglected. The terms written out explicitly on the right-hand side of these two equations represent generation of the stress component and, hence, of the kinetic energy of turbulence, k . Analysis of the normal stress equations, including the effects due to pressure strain, turbulent diffusion and dissipation, while desirable, is hampered by the unavailability of appropriate experimental data; hence, the contributions of the latter terms to the respective balances cannot presently be established. Nevertheless, simplified analysis of the generation terms alone provides a basis for checking consistency in the measurements and can shed light on the behavior of

the flow. In the vicinity of the bend symmetry plane, symmetry considerations support the notion that the generation terms in equations (6.2.1) and (6.2.2) involving the z coordinate direction should be small relative to those involving variations in the r and θ directions. Approximate balances for $\overline{u_\theta^2}$ and $\overline{u_r^2}$ are then given by:

$$\frac{D}{Dt} \left(\frac{\overline{u_\theta^2}}{2} \right) = - \underbrace{\overline{u_\theta u_r} \frac{\partial u_\theta}{\partial r}}_A + \overline{u_\theta^2} \left[\underbrace{-\frac{1}{r} \frac{\partial u_\theta}{\partial \theta}}_B - \underbrace{\frac{U_r}{r}}_C \right]$$

$$\frac{D}{Dt} \left(\frac{\overline{u_r^2}}{2} \right) = - \underbrace{\overline{u_r^2} \frac{\partial u_r}{\partial r}}_D + \overline{u_\theta u_r} \left[\underbrace{\frac{U_\theta}{r}}_E - \underbrace{\frac{1}{r} \frac{\partial u_r}{\partial \theta}}_F \right]$$

At 90° $\overline{u_\theta u_r}$ is positive everywhere and, except for a small region $0.2 \leq \eta \leq 0.4$ where $\partial u_\theta / \partial r$ is negative, term A represents a negative contribution to the balance of $\overline{u_\theta^2}$. From $\theta = 45^\circ$ to 90° the streamwise velocity component U_θ is decelerated between $\eta \approx 0.2$ and 0.5 by the inviscid mechanism explained above. The result is for term B in equation (6.2.3) to contribute positively (together with term A) to the balance of $\overline{u_\theta^2}$. At all radial locations near the symmetry plane, term C represents a reduction in the magnitude of $\overline{u_\theta^2}$, but because of the small values of the ratio U_r/r , the contribution of this term relative to A and B is small. As shown in Figure 6.7, the net result is to produce a local increase in the magnitude of $\overline{u_\theta}$ between $\eta = 0.4$ and 0.5 approximately.

In a similar manner, the localized minimum in $\overline{u_r}$ at $\eta \approx 0.4$ in the 90° plane can be explained. At all radial locations term E in equation (6.2.4) contributes positively to the balance of $\overline{u_r^2}$, although weakly near

the position of the minimum in \tilde{u}_r because of the small magnitude of $\overline{u_\theta u_r}$ there. Between $\theta = 45^\circ$ and 90° the plots for U_r show that, as for U_θ , U_r has also been decelerated leading to a positive contribution of term F to the balance of $\overline{u_r^2}$. However, the relatively strong streamwise deceleration in U_r induces large radial variations in its profiles producing regions in the flow where $\partial U_r / \partial r$ is large and positive. As shown in Fig. 6.7, this occurs between $\eta \approx 0.2$ (at $2z/D_H = 0.75$) and 0.7 (at $2z/D_H = 0$) and leads to a negative contribution of term D to the balance of $\overline{u_r^2}$. Since term D is the only one contributing negatively to $\overline{u_r^2}$ it must be the cause for the local minima in the profiles for $\overline{u_r^2}$ at $\theta = 90^\circ$. Therefore, the effect of this term in the balance must be large. It appears that the two terms, B in equation (6.2.3) and D in equation (6.2.4), are the principle source and sink for $\overline{u_\theta^2}$ and $\overline{u_r^2}$ respectively in this simplified analysis. The gradual disappearance of the maxima in \tilde{u}_θ and the minima in \tilde{u}_r between $\theta = 130^\circ$ and 177° is due to the inviscid oscillatory nature of the flow since, by restoring high speed fluid to the core of the flow (see Figures 6.8 and 6.9), the respective roles of terms B and D in equations (6.2.3) and (6.2.4) are reversed.

The anisotropic effects in $\overline{u_\theta^2}$ and $\overline{u_r^2}$ discussed above can not be reproduced by the calculations. Nor is it surprising that the minima observed in the experimental profiles for the mean velocity components at $\theta = 90^\circ$ and 130° are not predicted. The assumption of local isotropy in the turbulence model produces such large levels of *false physical diffusion* as to preclude an accurate spatial resolution of the flow. For example, at $\theta = 90^\circ$ in the symmetry plane of the bend, estimates of v_t/v from the measurements suggest that the ratio is less than 10 between

$\eta = 0.1$ and 0.9 . However, calculations of this ratio at the same $z = 0$ location vary from 40 ($0 \leq \eta \leq 0.4$) to 300 ($0.4 < \eta \leq 0.95$). Although *numerical diffusion* compounds the problem, the fact that it is the more accurate QUICK scheme results which show *worse* agreement with the measurements at this location, strongly supports the contention that the source of false diffusion is more physical in nature (due to the model) than it is numerical (due to the differencing scheme). In fact, the higher levels of numerical diffusion in the HYBRID scheme distort physical diffusion in the turbulence model and lead to the incorrect impression of better predictions at various streamwise locations!

In general, the QUICK scheme calculations of mean radial velocity show better qualitative agreement with the measurements than the HYBRID results. Both schemes yield calculated values of k which are in reasonably good agreement with estimates of k from the measurements; with k_{meas} approximated as $k_{\text{meas}} = \frac{1}{2}(\overline{u_{\theta}^2} + 2\overline{u_r^2})$. However, the agreement is misleading. When summed, the experimentally determined maxima in $\overline{u_{\theta}^2}$ and the minima in $\overline{u_r^2}$ compensate to yield fairly uniform radial distributions of k_{meas} . To indicate clearly the inadequacy of the model, the plots provided show comparisons between predicted values of \tilde{u}_{θ} and \tilde{u}_r (calculated assuming $\overline{u_{\theta}^2} = \overline{u_r^2} = \frac{2}{3}k_{\text{calc}}$) and direct measurements of these stresses at $2z/D_H = 0$ and 0.5 .

In several of the plots, both of the profiles given for U_{θ} at $2z/D_H = 0$ and 0.5 respectively show larger values of this component than were actually measured, suggesting different values for the experimental and computed mass flows in the streamwise direction. In fact, predictions of U_{θ} nearer the wall, not shown here, yielded values smaller than

those measured and gave the required mass balance.

Numerical experiments showed that a smaller length scale specification in equation (4.4.1) ($\lambda_m \approx 0.01 D_H$) at the inlet plane ($X_H = -5$) led to considerably reduced levels of the predicted turbulent kinetic energy. As a consequence, even though there was much worse agreement between predicted and estimated values of k , in the vicinity of $\theta = 90^\circ$ profiles of U_θ (but not of U_r) showed the local minima displayed by the measurements. Again, this type of partial agreement is misleading since it is artificially *reduced physical diffusion* (through the specification of a larger dissipation at the inlet plane) which yields the result. In general, much better overall predictions were obtained by prescribing an inlet plane length scale variations as outlined in section 4.4

At $\theta = 177^\circ$ the flow in the bend shows all the maxima in the U_θ profiles displaced towards the concave wall in the presence of relatively large levels of transverse flow. Even though the radial velocity component has been decreasing steadily from about $\theta = 90^\circ$ due to the oscillatory inviscid flow mechanism, there is no evidence in the U_r profiles at any location in the bend of a Dean instability in the vicinity of the concave wall. The instability is of the type found by Taylor in concentric cylinder flows (Dean [1928]) and has been observed experimentally by, for example, Cheng et al. [1979]. It has been predicted numerically only in laminar flow regime (Cheng et al. [1975], Joseph and Smith [1975], and Ghia and Sohkey [1977]). Conceivably, in a bend of larger deflection angle than the present one, the inviscid flow oscillation could also induce an extra pair of vortices in the vicinity of the concave wall. There is supporting evidence for this conjecture in

Figure 8 (Station 12) of Hawthorne's paper [1951] and in the measured results of this work at $X_H = 1$. At this location the inviscid flow mechanism has not ceased to apply completely because of the persistence of streamline curvature in the flow. Such a mechanism for generating an extra pair of vortices in the cross-stream plane is distinct from the Dean instability which is associated with destabilizing curvature effects. At $\theta = 177^\circ$ both of the normal stresses display a surprising degree of uniformity and the shear stress is small, implying that the flow is well-mixed and relatively isotropic at this location. Except for U_r , at this station the calculations are in very good agreement with the measurements. Although inaccurate in terms of absolute values, QUICK scheme predictions of U_r are vastly superior to those obtained with the HYBRID scheme. The QUICK scheme faithfully reproduces the measured profile curvatures while the HYBRID scheme predicts negative values where none exist in the measurements!

At $X_H = 1$ (Figure 6.10) the secondary flow emerging from the bend has experienced a drastic change in both its magnitude and sense. The radial velocity component has been reduced to less than about 4% and a transverse flow appears near the concave wall, opposite in sense to that existing within the bend at the same radial location. A similar observation was made by Taylor et al. [1982] in their laminar flow measurements at $X_H = 2.5$. As mentioned above, the phenomenon is attributed to the persistence of the inviscid flow mechanism downstream of the bend. Because of the fairly uniform and similar levels of the normal stress components measured at $\theta = 177^\circ$ and $X_H = 1$, it is unlikely that gradients of these stresses are altering significantly the intensity and pattern

of the cross-stream flow at these stations.

As of $X_H = 0$ the flow in the downstream tangent reverts slowly to a straight duct flow condition, with the maximum in the U_θ component tending towards the duct center. However, the maximum has moved only a small amount, from $\eta \approx 0.9$ to a value of about 0.65 over a duct length of $20 D_H$. Similar indications of developing straight duct flow also appear in the profiles for the longitudinal turbulence intensity \bar{u}_θ/U_B and the shear stress at $X_H = 5, 10$ and 20 (see Figures 6.11-6.13 and 6.16). By contrast, the transverse components of mean velocity and turbulence intensity do not show the same rates of adjustment to the new flow conditions. The profiles for U_r indicate that as of $X_H = 5$ a cross-stream flow pattern, similar but much weaker to that in the bend, arises in the downstream tangent. At $X_H = 2.5$, their furthest downstream station, Taylor et al. observed the same result in their turbulent flow measurements.

The resurgence of a bend-like secondary motion in the downstream tangent is surprising and, at present, not fully understood. Calculations of the flow between $X_H = 0$ and 5 , using the QUICK scheme are in qualitative agreement with the measurements. In particular, the transverse variations of U_r at $2z/D_H = 0$ and 0.5 are correctly simulated by QUICK but incorrectly simulated by HYBRID. The persistence of a peak in U_θ near the convex-wall side of the duct at $2z/D_H = 0.50$ (see Fig. 6.11) is due to turbulence model deficiencies. Because of smearing by numerical diffusion, this is not reflected in the HYBRID calculation.

Predicted cross-section vector plots and streamwise velocity contours of the flow at $\theta = 177^\circ$ using the two differencing schemes are

given in Fig. 6.17. The results show that the HYBRID scheme predicts two large vortices per half-symmetry plane in the bend while the QUICK scheme predicts essentially one, with a second, much smaller counter-rotating vortex, at the convex wall. The HYBRID results are in blatant disagreement with the measurements, the QUICK results are in qualitative agreement and this situation persists up to the exit plane at $X_H = 5$.

6.3 The ASM Predictions

In this section predictions of the flow using the ASM closure are presented and discussed. The amount of available core memory in the CDC 7600 computer at the Lawrence Berkeley Laboratory required performing the computations on a grid different from that reported in Section 6.2. For the present case, the unequally spaced grid distribution initially adopted was: $(z = 12) \times (r = 22) \times (x = 20)$ in the upstream tangent of $5 D_H$; $(z = 12) \times (r = 22) \times (\theta = 45)$ in the bend; and $(z = 12) \times (r = 22) \times (x = 15)$ in the downstream tangent of $4.2 D_H$. The distribution of grid nodes over a cross-stream plane is given in Table 6.2. Recent computations using a finer grid size in the bend along the main flow direction yielded somewhat better results. Accordingly, 60 equally spaced planes along the main flow direction was distributed in the bend, a 1/3 increase from what was used in all previous calculations.

As mentioned earlier, it has not yet been possible to obtain stable and converged results with the QUICK scheme, so that only HYBRID predictions are reported here. For comparison purpose, new calculations using the $k-\epsilon$ model (HYBRID only) with an identical grid are also included. Transverse distributions of the predictions at $z/D_H = 0$ and $z/D_H = 0.25$

for several streamwise planes are plotted in Figures 6.18 to 6.37. In these figures, solid lines represent best curve fits to the experimental data discussed earlier, dot-dash lines are the ASM predictions, and dot-dot-dash lines are the corresponding $k-\epsilon$ model predictions.

From an overall inspection of the results, several observations concerning the ASM predictions can be made. They are:

1. The mean flow results are not better than those predicted with the $k-\epsilon$ model. In fact, at $\theta = 90^\circ$ (Figure 6.22), it is the $k-\epsilon$ model which produces better agreement with the data!
2. The ASM predicts a slower development of the secondary motion in the bend than that predicted by the $k-\epsilon$ model.
3. Although capable of predicting turbulence anisotropy as shown in the plots of \bar{u}_r/U_B and \bar{u}_θ/U_B , the ASM predictions failed to reproduce the experimentally observed local extrema in U_θ , U_r , \bar{u}_θ , \bar{u}_r and $\overline{u_r u_\theta}$ around $\eta = 0.4$ and $\theta = 90^\circ$.

Since the equation system describing the flow is highly non-linear and strongly coupled, it is very difficult to single out the causes for the poor agreement revealed in Figures 6.18 to 6.37. Faced with these discouraging results, one might well ask whether or not the ASM closure proposed in Section 3.3.2, which was developed with 2D flows in mind, is capable of predicting such a complex, three-dimensional, highly anisotropic turbulent flow as the present one. To answer this question, or to at least bear light on the problem, two simplified "experimental" tests were conducted as explained below.

First, the measurements of U_r , U_θ along the symmetry plane at $\theta = 90^\circ$ (where the predictions were the worst), together with the $k-\epsilon$

model estimates of k , ϵ , and p were substituted into the ASM relations given in Section 3.3.3.* Solving the resultant equation system yielded the distributions plotted in Figures 6.23, 6.25 and 6.38 as the dashed lines. It is seen that, except for \tilde{u}_r , the ASM is capable of predicting the correct trends of the flow anisotropy provided that accurate spatial resolution of the mean velocities is presented to the equation system.

A second, more direct test was also performed. In addition to U_r and U_θ , the measurements of \tilde{u}_r and \tilde{u}_θ were also used. Substituting these measured quantities, together with the k - ϵ model estimates of k , ϵ , and P into equation (3.3.3.4) and solving for $\overline{u_r u_\theta}$ yielded the much better distribution plotted in Figure 6.38 as the dotted line.

As a result of these two tests, it is now believed that the ASM closure proposed in Section 3.3.2 is indeed adequate for predicting complex anisotropic 3D turbulent flows of the present kind, provided that accurate spatial resolution of the mean velocities is achieved. Previous calculations using the k - ϵ model suggested, however, that substantially refined grid would be required to significantly improve the numerical accuracy of the present predictions. Computation costs and memory availability simply prohibited the use of finer grids to reduce the numerical diffusion. The alternative of using higher order differencing such as the QUICK scheme is probably a better course to pursue.

During the course of the research, three variations of the log-wall function approach were tested: the standard TEACH code method (Gosman

*In the absence of information concerning streamwise and spanwise variations of the velocity components, terms containing these quantities, including $\partial U_\theta / \partial \theta$, $\partial U_r / \partial \theta$ and $\partial U_z / \partial z$, were neglected.

and Ideriah [1976]); the Chieng and Launder [1979] method; and the method used by, among others, Naot and Rodi [1981]. As a consequence, it was found that the flow pattern, especially the secondary flow velocity components U_r and U_z , is sensitive to the way the near wall flow is treated. However, no one of the three methods produced results in better overall agreement with the data than the others. Because of its simplicity, the treatment of Naot and Rodi was chosen for the calculations presented above.

CHAPTER 7. CONCLUSIONS AND RECOMMENDATIONS

The new measurements provided here for the mean flow in strongly curved 180° bends reveal features which are in qualitative agreement with results obtained from inviscid flow analysis. Measurements of the turbulence characteristics of the flow at $\theta = 90^\circ$ and 130° show striking variations in the radial direction which appear to be due to large shearing motions induced by the inviscid mechanism in the core of the flow. Within the context of an interpretation which neglects turbulence diffusion and pressure redistribution effects, the velocity gradients induced in the core of the flow work locally on the turbulent stresses to increase the longitudinal stress component ($\overline{u_\theta^2}$) and decrease the radial stress component ($\overline{u_r^2}$).

Between $\theta = 0^\circ$ and 45° , stabilizing and destabilizing curvature effects at the convex and concave wall respectively are responsible for generating relatively large levels of anisotropy near these surfaces. As of $\theta = 45^\circ$, the cross-stream motion contributes to the production of a more complicated anisotropic pattern in the turbulent stresses. For example, regions of negative production of turbulent kinetic energy arise at $\theta = 90^\circ$. Between $\theta = 130^\circ$ and 177° the anisotropy in the measured normal stresses is reduced, due to the uniformizing influence of the secondary motion in the flow.

Measurements of U_r in the bend show that, except for around $\theta = 45^\circ$, the return flow in the cross-stream plane is restricted to fairly narrow bands of width $\approx D_H/8$ adjacent to each of the side walls. The measure-

ments of U_r did not reveal vortex structures at the convex wall in the bend, nor at the concave wall where they might be expected to arise due to the Dean instability. However, the sense of the cross-stream flow at $X_H = 1$ does suggest a brief appearance of this type of instability in the exit tangent. Between $\theta = 0^\circ$ and $X_H = 20$ there was no evidence in the measurements of a significant Reynolds stress driven secondary motion.

In this investigation the influence of the bend on the upstream tangent flow is already noticeable at $X_H = -5$. Although weak, a transverse flow is set up at this location (and at $X_H = -1$) of characteristics which correspond with the simple notion of a superposition of two cross-stream motions: the first induced by Reynolds stress gradients in the cross-stream plane; the second due to the favorable streamwise pressure gradient arising at the convex wall in the bend. In the downstream tangent secondary motions are drastically decreased between $\theta = 180^\circ$ and $X_H = 1$. The decrease is related to the oscillating nature of the secondary motion which, as shown by inviscid flow theory and supported by the present results, as of $\theta = 90^\circ$ has started opposing the initial source of circulation set up by the transverse pressure gradient in the bend. Between $X_H = 1$ and 20 the flow reestablishes characteristics typical of straight ducts. However, the measurements show the persistence of a weak secondary motion in the downstream tangent with the same sense of rotation as the flow in the bend and a slow recovery of the radial normal stress compared to the longitudinal component.

Predictions of the experimental flow were first made with a $k-\epsilon$ model of turbulence using a partially-parabolic numerical procedure. Two

finite differencing techniques were used with global accuracies of first order (HYBRID) and second order (QUICK). Testing and predictions with QUICK in the laminar flow regime clearly showed it to be superior to HYBRID. The differences between the results obtained using the two schemes in turbulent flow are notable. Of the two, only QUICK reproduces correctly the trends in the measured cross-stream flow. The HYBRID scheme gives the incorrect impression of better streamwise component velocity predictions. This is due to numerical diffusion which smears out the spacial variation of this component. Although QUICK scheme predictions for U_θ differ more from the measurements, this is explained by the fact that with numerical diffusion reduced, it is the false physical diffusion in the $k-\epsilon$ model which is revealed by the computed results.

Numerical experiments confirmed a fairly strong sensitivity of the model to the inlet plane specification of dissipation. Fixing a small-but incorrect dissipation length scale at the inlet plane led to somewhat improved predictions of the U_θ component at $\theta = 90^\circ$, where this component shows large changes in the transverse direction. However, predictions of U_r and of k were much less satisfactory.

In an earlier study (Chang et al. [1982]) it was reported that predictions of turbulent flow in a 90° bend were mildly sensitive to the sense of cross-stream flow fixed at the inlet boundary condition. The effect was too small to alter significantly the streamwise evolution of the flow. In this study, insignificant differences were observed between predictions of the flow with the cross-stream motion set equal to zero, and predictions with the cross-stream motion specified from

the measurements. The insensitivity of the flow in a bend to the inlet plane streamwise component of vorticity is explained by reference to the general form of the equation for the variation of this quantity along a streamline (Horlock and Lakshminarayana [1973]):

$$\frac{\partial}{\partial s} \left(\frac{\xi_{\theta}}{V} \right) = - \frac{2\xi_r}{VR} + \frac{v \nabla^2 \xi_{\theta}}{V^2}$$

In the case of a flow entering a bend from a straight duct, generally $\xi_r \gg \xi_{\theta}$, especially near the side walls. As a consequence, the equation shows that along streamlines curving through the bend, the streamwise development of vorticity is due primarily to deflection of transverse vorticity. Viscous diffusion of streamwise vorticity, even in turbulent flows, is of secondary importance.

Subsequent predictions with the ASM closure did not yield better agreement with measurements than did the $k-\epsilon$ results. Consequently, two "experimental" tests were carried out to check indirectly the predicting ability of the ASM closure. It was found that the approximations proposed in Section 3.3.2 are indeed capable of resolving the anisotropy of the turbulence correctly, provided that the mean velocity field is known accurately; i.e. with good spatial resolution.

The following recommendations are offered for continuing work:

1. Laminar flow measurements should be performed in the bend and downstream tangent to establish definitively the superior performance of QUICK for predicting curved duct flows and for verifying the various vortical structures predicted by this scheme.
2. More detailed turbulent flow measurements are required to under-

AD-R132 845

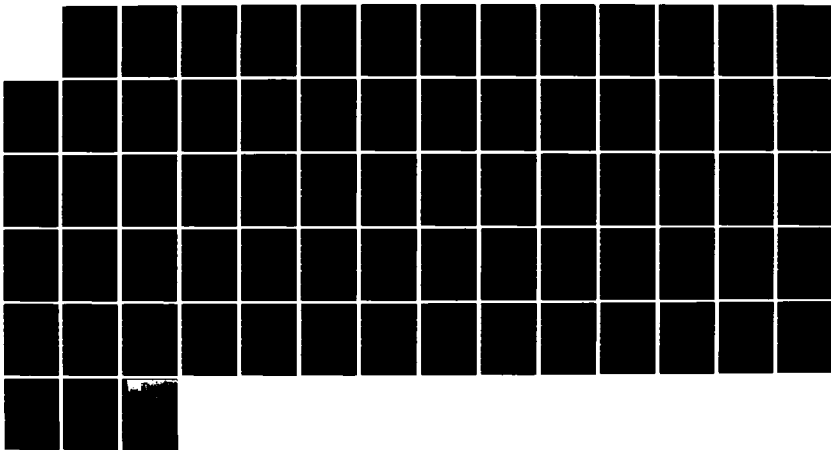
TURBULENT FLOW IN PASSAGE AROUND A 180 DEG BEND; AN
EXPERIMENTAL AND NUME. (U) CALIFORNIA UNIV BERKELEY
DEPT OF MECHANICAL ENGINEERING J A HUMPHREY SEP 83
UCB/FM-83-7 N00014-80-C-0031

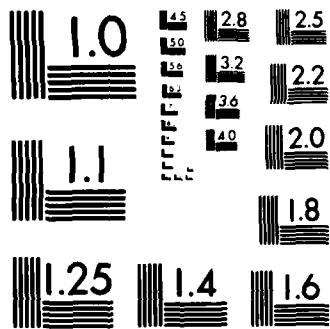
2/2

UNCLASSIFIED

F/G 20/4

NL





MICROCOPY RESOLUTION TEST CHART
NATIONAL BUREAU OF STANDARDS-1963-A

stand the relaxation processes taking place in the downstream tangent.

3. Modeling at the full stress equation closure level will certainly be required to predict wall interactions accurately, including curvature effects.
4. Fine grid calculation with the QUICK scheme using the ASM closure is recommended. This could allow more definite conclusions to be drawn concerning the behavior of the ASM closure.
5. It is believed that the present specifications of the log-wall relations along all three walls are inaccurate. Since they are essential to produce reliable predictions by means of schemes which invoke these relations, more detailed experimental work concerning these laws in 3D turbulent walls flows is strongly recommended.
6. In parallel to the experimental work mentioned above in 5., numerical experiments on the sensitivity of the flow to the model constants κ and E are recommended. In particular, the constant E should be made functions of pressure gradients along the main flow direction for U_θ and over a cross-sectional plane for U_r and U_z .

REFERENCES

1. Bergeles, G. (1976), "Three-Dimensional Discrete-Hole Cooling Processes. An Experimental and Theoretical Study," Ph.D. thesis, University of London.
2. Boussinesq, J. (1877), "Théorie de l'écoulement Tourbillant," Mém. Près. Acad. Sci., 23, p. 46, Paris.
3. Bradshaw, P. (1973), "Effects of Streamline Curvature on Turbulent Flow," AGARDograph, No. 169.
4. Briley, W.R. and McDonald, H. (1979), "Analysis and Computation of Viscous Subsonic Primary and Secondary Flows," AIAA Paper No. 79-1453, 4th AIAA-CFD Conference, Williamsburg, Virginia.
5. Brundrett, E. and Baines, W.D. (1964), "The Production and Diffusion of Vorticity in Duct Flow," J. Fluid Mech., 19, p. 375.
6. Bruun, H.H. (1979), "An Experimental Investigation of Secondary Flow Losses in Bends with Rectangular Cross Sections," CUED/A - Turbo/TR 95, Dept. of Engr., Univ. of Cambridge.
7. Bryant, D. and Humphrey, J.A.C. (1976), "Conservation Equations for Laminar and Turbulent Flows in General Three-Dimensional Curvilinear Coordinates," Rep No. CHT-76-6, Imperial College of Science & Technology.
8. Buchhave, P. (1975), "Biasing Errors in Individual Particle Measurements with the LDV--Counter Signal Processor," Proc. LDV Symposium Copenhagen, Technical Univ. of Denmark, p. 258.
9. Buchhave, P. (1979), "The Measurement of Turbulence with the Burst-Type Laser Doppler Anemometer - Errors and Correction Methods," Ph.D. thesis, State Univ. of New York at Buffalo.
10. Buggeln, R.C., Briley, W.R., and McDonald, H. (1980), "Computation of Laminar and Turbulent Flow in Curved Ducts, Channels, and Pipes using the Navier-Stokes Equations," Rep R80-920006-F, prepared for the Office of Naval Research.
11. Burggraf, O.R. (1966), "Analytical and Numerical Studies of the Structure of Steady Flows," J. Fluid Mech., 24, p. 113.
12. Chang, S.M., Han, T., and Humphrey, J.A.C. (1982), "Prediction of Case 512 for the 1981-82 AFOSR-HTTM-Stanford Conference on Complex Turbulent Flows," Vol. III, p. 1375.

13. Cheng, K.C., Lin, R-C., and Ou, J-W. (1975), "Graetz Problem in Curved Rectangular Channels with Convective Boundary Condition--The Effect of Secondary Flow on Liquid Solidification-Free Zone," Int. J. Heat Mass Transfer, 18, p. 996.
14. Chieng, C.C. and Launder, B.E. (1979), "Calculation of Turbulent Heat Transport Downstream from an Abrupt Pipe Expansion," Mech. Engr. Dept., Rep. TF/10/79, Univ. of California, Davis.
15. Dean, W.R. (1928), "Fluid Motion in a Curved Channel," Proc. Roy. Soc. London, Ser. A, 121, p. 402.
16. Drain, L.E. (1980), "The Laser-Doppler Technique," John Wiley and Sons Ltd., New York.
17. Durst, F., Melling, A., and Whitelaw, J.H. (1976), "Principles and Practices of Laser-Doppler Anemometry," Academic Press, London.
18. Eichenberger, H.P. (1952), "Shear Flow in Bends," Tech. Rep. No. 2, Mass. Inst. Tech., Cambridge, Mass.
19. Eichenberger, H.P. (1953), "Secondary Flow within a Bend," J. Math. and Phys., 32, p. 34.
20. Eskinazi, S. and Yeh, H. (1956), "An Investigation on Fully Developed Turbulent Flows in a Curved Channel," J. Aero. Sci., 23, p. 23.
21. George, W.K. (1975), "Limitations to Measurement Accuracy Inherent in the Laser Doppler Signal," Proc. LDV Symposium Copenhagen, Tech. Univ. of Denmark, p. 20.
22. Gessner, F.B. and Emery, A.F. (1982), "The Numerical Prediction of Developing Turbulent Flow in Rectangular Ducts," to appear in J. Fluid Engr.
23. Ghia, K.N. and Sokhey, J.S. (1977), "Laminar Incompressible Viscous Flows in Curved Ducts of Regular Cross-Sections," J. Fluid Engr., 99, p. 640.
24. Gibson, M.M. (1978), "An Algebraic Stress and Heat-Flux Model for Turbulent Shear Flow with Streamline Curvature," Int. J. Heat Mass Transfer, 21, p. 1609.
25. Gibson, M.M. and Launder, B.E. (1978), "Ground Effects on Pressure Fluctuations in the Atmospheric Boundary Layer," J. Fluid Mech., 86, p. 491.
26. Goldstein, S. (ed.) (1965), "Modern Developments in Fluid Dynamics," Vol. I, Dover Publications, Inc., New York.

27. Gosman, A.D. and Ideriah, F.J.K. (1976), "TEACH-2E: A General Computer Program for Two-Dimensional, Turbulent, Recirculating Flows," Dept. Mech. Engr., Imperial College of Science and Technology, London.
28. Han, T., Humphrey, J.A.C. and Launder, B.E. (1981), "A Comparison of Hybrid and Quadratic-Upstream Differencing in High Reynolds Number Elliptic Flows," *Comput. Meths. Appl. Mech. Engr.*, 29, p. 81.
29. Hanjalić, K. and Launder, B.E. (1972), "A Reynolds Stress Model of Turbulence and Its Application to Thin Shear Flows," *J. Fluid Mech.*, 52, p. 609.
30. Hawthorne, W.R. (1951), "Secondary Circulation in Fluid Flow," *Proc. Roy. Soc. London, Ser. A*, 206, p. 374.
31. Hawthorne, W.R. (1963), "Flow in Bent Pipes," *Proc. Seminar in Aero. Sci., National Aero. Lab., Bangalore, India*, p. 305.
32. Horlock, J.H. and Lakshminarayana, B. (1973), "Secondary Flows: Theory, Experiment, and Application in Turbomachinery Aerodynamics," *Ann. Rev. Fluid Mech.*, 5, p. 247.
33. Huang, P.G., Launder, B.E. and Leschziner, M.A. (1983), "Discretization of Non-Linear Convection Processes: A Broad Range Comparison of Four Schemes," TFD/83/1, Mech. Engr. Dept., Univ. of Manchester Inst. Sci. Tech., England.
34. Humphrey, J.A.C. (1977), "Flow in Ducts with Curvature and Roughness," Ph.D. thesis, Univ. of London.
35. Humphrey, J.A.C. and Pourahmadi, F. (1982), "A Generalized Algebraic Relation for Predicting Developing Curved Channel Flow with a $k-\epsilon$ Model of Turbulence," Lawrence Berkeley Lab. Rep. LBL-12009 Rev. 2, Univ. of California, Berkeley.
36. Humphrey, J.A.C., Taylor, A.M.K. and Whitelaw, J.H. (1977), "Laminar Flow in a Square Duct of Strong Curvature," *J. Fluid Mech.*, 83, p. 509.
37. Humphrey, J.A.C., Whitelaw, J.H. and Yee, G. (1981), "Turbulent Flow in a Square Duct with Strong Curvature," *J. Fluid Mech.*, 103, p. 443.
38. Johnston, J.P. (1978), "Internal Flows," in *Turbulence*, ed. by Bradshaw, P., *Topics in Applied Physics*, 12, Springer-Verlag, p. 109.
39. Jones, W.P. and Launder, B.E. (1972), "The Prediction of Laminarization with a Two-Equation Model of Turbulence," *Int. J. Heat Mass Transfer*, 15, p. 301.

40. Joseph, B., Smith, E.P. and Alder, R.J. (1975), "Numerical Treatment of Laminar Flow in Helically Coiled Tubes of Square Cross-Section," *AICHE J.* 21, No. 5, p. 965.
41. Joy, W. (1950), "Experimental Investigation of Shear Flow in Rectangular Bends," M.Sc. thesis, Mass. Inst. Tech., Cambridge, Mass.
42. Kreskovsky, J.P., Briley, W.R. and McDonald, H. (1980), "Prediction of Laminar and Turbulent Primary and Secondary Flows in Strongly Curved Ducts," Rep. R80-900007-12, prepared for the NASA Lewis Res. Center.
43. Laufer, J. (1950), "Investigation of Turbulent Flow in a Two-Dimensional Channel," TN-2123, NACA, USA.
44. Launder, B.E. (1971), "An Improved Algebraic Stress Model of Turbulence," Dept. Mech. Engr., Rep. No. TM/TN/A/9, Imperial College.
45. Launder, B.E. (1980), "Turbulence Transport Models for Numerical Computation of Fluid Flow," class notes for ME-213, Dept. Mech. Engr., Univ. of California, Davis.
46. Launder, B.E., Priddin, C.H. and Sharma, B.I. (1977), "The Calculation of Turbulent Boundary Layers on Spinning and Curved Surfaces," *J. Fluid Engr.*, 99, p. 231.
47. Launder, B.E., Reece, G.J. and Rodi, W. (1975), "Progress in the Development of a Reynolds-Stress Turbulence Closure," *J. Fluid Mech.*, 68, p. 537.
48. Launder, B.E. and Spalding, D.B. (1972), "Mathematical Models of Turbulence," Academic Press.
49. Launder, B.E. and Spalding, D.B. (1974), "The Numerical Computation of Turbulent Flows," *Comput. Meths. Appl. Mech. Engr.*, 3, p. 269.
50. Leonard, B.P. (1979), "A Stable and Accurate Convective Modelling Procedure Based on Quadratic Upstream Interpolation," *Comput. Meths. Appl. Mech. Engr.*, 19, p. 59.
51. McLaughlin, D.K. and Tiederman, W.G. (1973), "Biasing Correction for Individual Realization Laser Anemometry Measurements in Turbulent Flows," *Phys. of Fluids*, 16, No. 12, p. 2082.
52. McNally, W.D. and Sockol, P.M. (1981), "Computational Methods for Internal Flows with Emphasis on Turbomachinery," NASA-TM-82764, presented at the Symposium on Computers in Flow Predictions and Fluid Dynamics Experiments at the ASME Winter Annual Meeting, Washington, D.C.

53. Melling, A. (1975), "Investigation of Flow in Non-Circular Ducts and Other Configurations by Laser-Doppler Anemometry," Ph.D. thesis, Univ. of London.
54. Melling, A. and Whitelaw, J.H. (1976), "Turbulent Flow in a Rectangular Duct," *J. Fluid Mech.*, 78, p. 289.
55. Nikuradse, J. (1932), "Gesetzmässigkeit der turbulenten Stromung in glatten Rohren," *Forsch. Arb. Ing. Wes.*, 356.
56. Naot, D. and Rodi, W. (1981), "Numerical Simulation of Secondary Currents in Open Channel Flow with an Algebraic Stress Turbulence Model," SFB 80/T/187, Univ. of Karlsruhe.
57. Patankar, S.V. (1980), "Numerical Heat Transfer and Fluid Flow," McGraw-Hill.
58. Perkins, H.J. (1970), "The Formation of Streamwise Vorticity in Turbulent Flow," *J. Fluid Mech.*, 44, p. 721.
59. Pratap, V.S. (1975), "Flow and Heat Transfer in Curved Ducts," Ph.D. Thesis, Imperial College, London.
60. Pratap, V.S. and Spalding, D.B. (1975), "Numerical Computations of the Flow in Curved Ducts," *Aero. Quart.*, 26, p. 219.
61. Reece, G.J. (1977), "A Generalized Reynolds-Stress Model of Turbulence," Ph.D. thesis, Univ. of London.
62. Reynolds, W.C. (1976), "Computation of Turbulent Flows," *Ann. Rev. Fluid Mech.*, 8, p. 183.
63. Rodi, W. (1976), "A New Algebraic Relation for Calculating the Reynolds Stresses," *Mech. Fluid, ZAMM*, 56, T219-T221.
64. Rodi, W. (1978), "Turbulence Models and Their Application in Hydraulics--A State-of-the-Art Review," SFB 80/T/127, Univ. of Karlsruhe.
65. Rotta, J.C. (1951), "Statistische theorie nichthomogener turbulenz," *Z. Phys.*, 129, p. 547.
66. Shamroth, S.J. and Gibeling, H.J. (1979), "The Prediction of the Turbulent Flow Field About an Isolated Airfoil," AIAA paper 79-1543.
67. Shir, C.C. (1973), "A Preliminary Numerical Study of Atmospheric Turbulent Flows in the Idealized Planetary Boundary Layer," *J. Atmos. Sci.*, 30, p. 1327.

68. Spalding, D.B. (1972), "A Novel Finite Difference Formulation for Differential Expressions Involving Both First and Second Derivatives," *Int. J. Num. Meths. Engr.*, 4, p. 551.
69. Squire, H.B. (1954), "Note on Secondary Flow in a Curved Circular Pipe," Unpublished British Aero. Res. Council Rep. No. 16601.
70. Taylor, A.M.K.P., Whitelaw, J.H. and Yanneskis, M. (1982), "Measurements of Laminar and Turbulent Flow in a Curved Duct with Thin Inlet Boundary Layers," NASA-CR-3367, USA.
71. Tennekes, H. and Lumley, J.L. (1972), "A First Course in Turbulence," MIT Press.

<u>Quantity</u>	<u>Range of Maximum Systematic Error + (deviation %)</u>	<u>Maximum Random Error⁺⁺ (r.m.s. %)</u>
U_{θ}/U_B	- 1% to 2%	$\pm 2\%$
U_r/U_B	- 1% to 2%	$\pm 2\%$ to $\pm 3\%$
\tilde{u}_{θ}/U_B	- 2% to 2%	$\pm 2\%$ to $\pm 3\%$
\tilde{u}_r/U_B	- 2% to 2%	$\pm 2\%$ to $\pm 4\%$
$\overline{u_{\theta}u_r}/U_B^2$	- 2% to 2%	$\pm 3\%$ to $\pm 7\%$

+ Error confined mainly to near wall flow regions; does not include angular uncertainty discussed in text.

++ Largest errors confined to small flow regions; does not include a small positioning uncertainty of probe volume in the flow.

Table 2.1 Estimated maximum measurement errors

ϕ_i	α_i	β_i	C_i
$\phi_e = \frac{1}{2}(\phi_E + \phi_p) + \alpha_e \phi_p + \beta_e$	$\frac{\delta_1}{8\Delta_1} (1 + \frac{\delta_1}{\delta_{1-1}})$ $-\frac{\delta_1}{8\Delta_{1+1}}$	$-\frac{(\delta_1)^2}{8\Delta_1} (\frac{\phi_E}{\delta_1} + \frac{\phi_W}{\delta_{1-1}})$ $-\frac{(\delta_1)^2}{8\Delta_{1+1}} (\frac{\phi_{EE} - \phi_E}{\delta_{1+1}} - \frac{\phi_E}{\delta_1})$	$C_e > 0$ $C_e < 0$
$\phi_w = \frac{1}{2}(\phi_p + \phi_w) + \alpha_w \phi_p + \beta_w$	$-\frac{\delta_{1-1}}{8\Delta_{1-1}}$ $\frac{\delta_{1-1}}{8\Delta_1} (1 + \frac{\delta_{1-1}}{\delta_1})$	$\frac{(\delta_{1-1})^2}{8\Delta_{1-1}} (\frac{\phi_W}{\delta_{1-1}} + \frac{\phi_W - \phi_{WW}}{\delta_{1-2}})$ $-\frac{(\delta_{1-1})^2}{8\Delta_1} (\frac{\phi_E}{\delta_1} + \frac{\phi_W}{\delta_{1-1}})$	$C_w > 0$ $C_w < 0$
$\phi_n = \frac{1}{2}(\phi_n + \phi_p) + \alpha_n \phi_p + \beta_n$	$\frac{\delta_j}{8\Delta_j} (1 + \frac{\delta_j}{\delta_{j-1}})$ $-\frac{\delta_j}{8\Delta_{j+1}}$	$-\frac{(\delta_j)^2}{8\Delta_j} (\frac{\phi_N}{\delta_j} + \frac{\phi_S}{\delta_{j-1}})$ $-\frac{(\delta_j)^2}{8\Delta_{j+1}} (\frac{\phi_{NN} - \phi_N}{\delta_{j+1}} - \frac{\phi_N}{\delta_j})$	$C_n > 0$ $C_n < 0$
$\phi_s = \frac{1}{2}(\phi_p + \phi_s) + \alpha_s \phi_p + \beta_s$	$-\frac{\delta_{j-1}}{8\Delta_{j-1}}$ $\frac{\delta_{j-1}}{8\Delta_j} (1 + \frac{\delta_{j-1}}{\delta_j})$	$\frac{(\delta_{j-1})^2}{8\Delta_{j-1}} (\frac{\phi_S}{\delta_{j-1}} + \frac{\phi_S - \phi_{SS}}{\delta_{j-2}})$ $-\frac{(\delta_{j-1})^2}{8\Delta_j} (\frac{\phi_H}{\delta_j} + \frac{\phi_S}{\delta_{j-1}})$	$C_s > 0$ $C_s < 0$

Table 4.1 QUICK scheme formulae for convective terms over a cross-stream plane

	$(r-r_i)/(r_o-r_i)$	$x/(D_H/2)$
1	.020	.050
2	.040	.150
3	.070	.250
4	.110	.350
5	.151	.450
6	.200	.550
7	.249	.635
8	.300	.715
9	.351	.785
10	.400	.850
11	.449	.900
12	.500	.950
13	.551	
14	.600	
15	.649	
16	.700	
17	.751	
18	.800	
19	.849	
20	.890	
21	.930	
22	.960	
23	.980	

Table 6.1 Grid distribution over a cross-stream plane for the k- ϵ model calculations

	$(r-r_i)/(r_o-r_i)$	$x/(D_H/2)$
1	.020	.064
2	.060	.192
3	.100	.311
4	.142	.423
5	.188	.527
6	.236	.625
7	.289	.716
8	.344	.801
9	.404	.881
10	.468	.960
11	.532	
12	.596	
13	.656	
14	.711	
15	.764	
16	.812	
17	.858	
18	.900	
19	.940	
20	.980	

Table 6.2 Grid distribution over a cross-stream plane for the algebraic stress model calculations

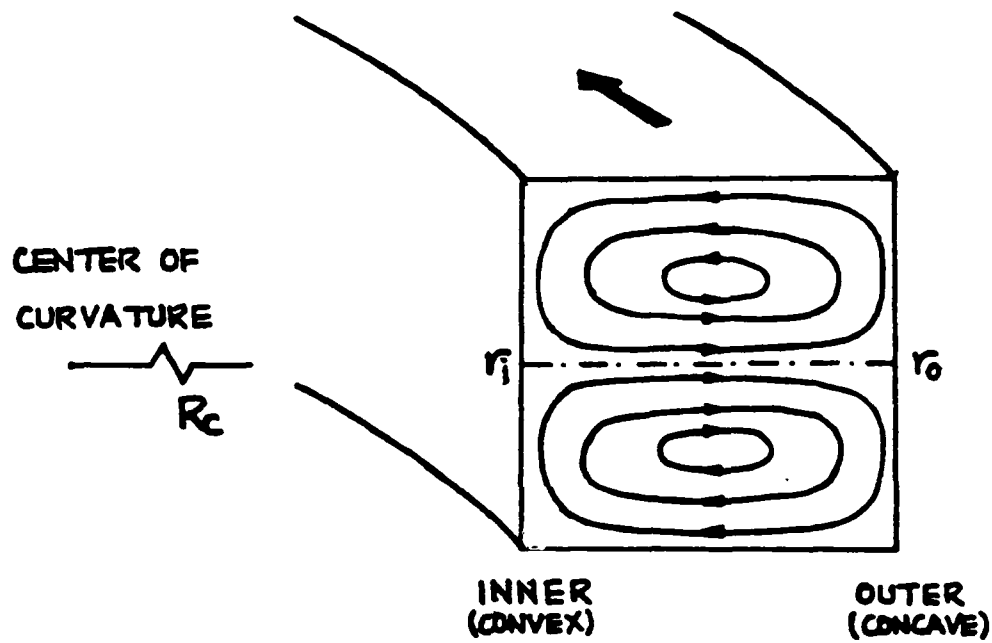


Figure 1.1 General flow pattern of the secondary motion of the first kind in a curved duct of square cross-section.

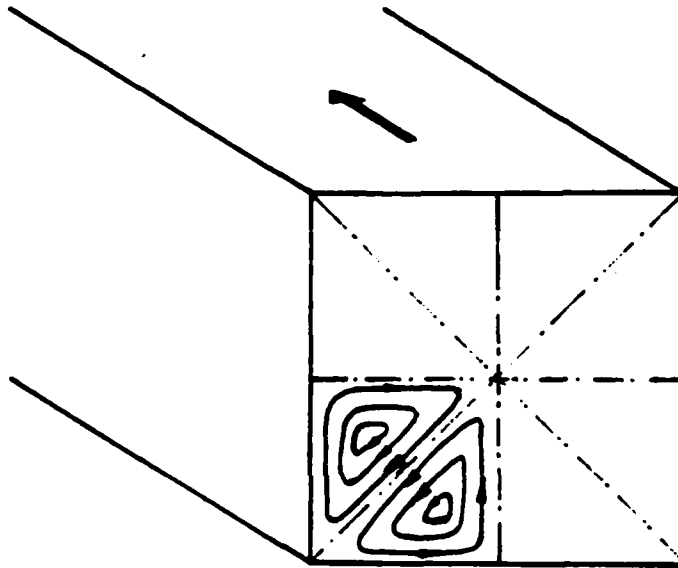


Figure 1.2 General flow pattern of the secondary motion of the second kind in a straight duct of square cross-section.

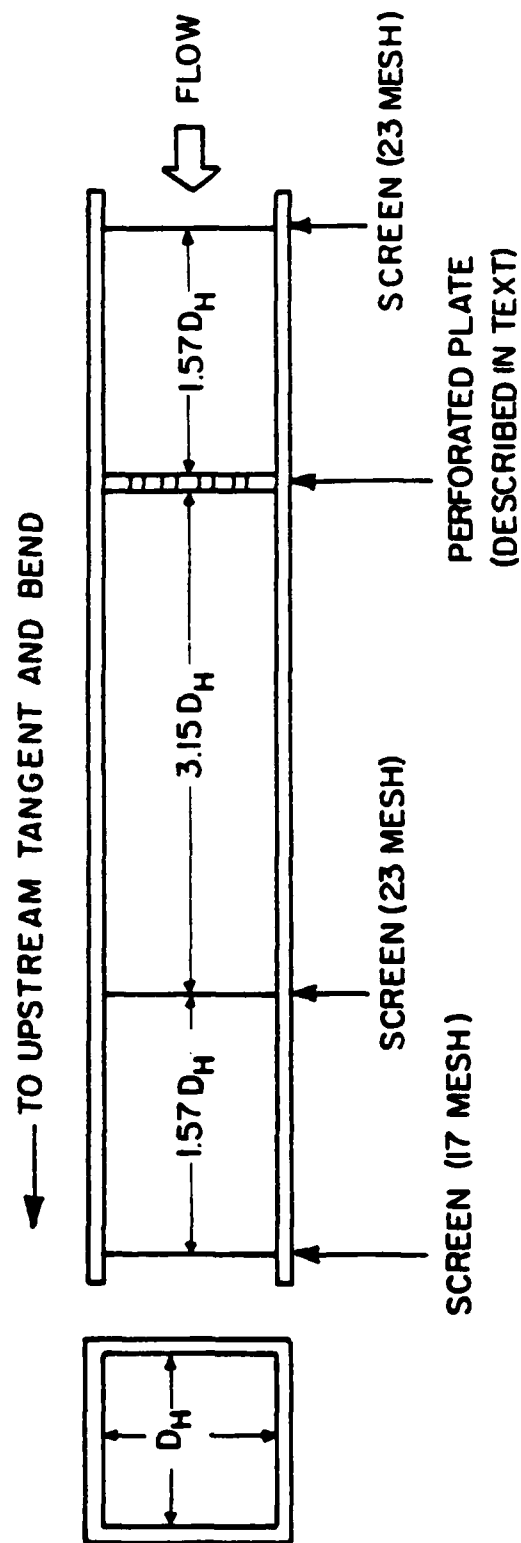


Figure 2.2 Optimum experimental arrangement of stainless steel screens and perforated plate in the flow-uniforming section preceding the upstream tangent.

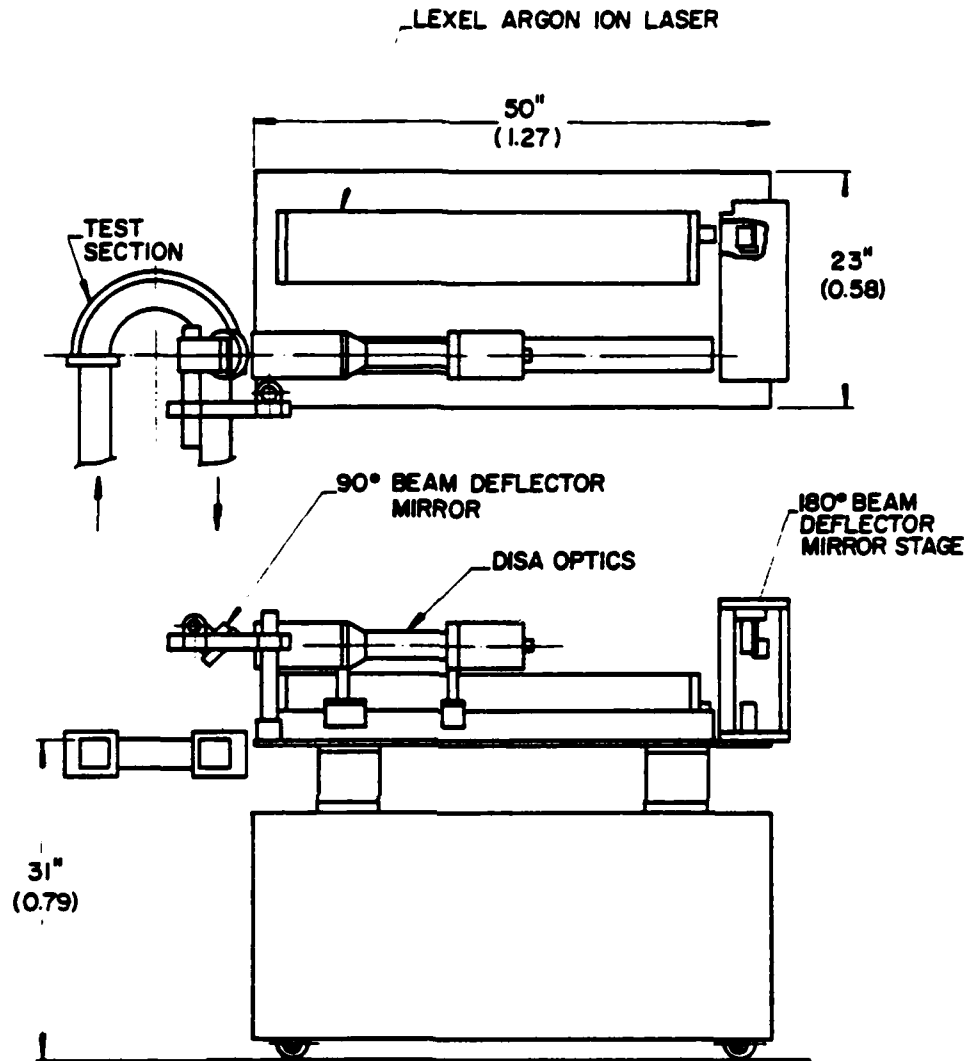
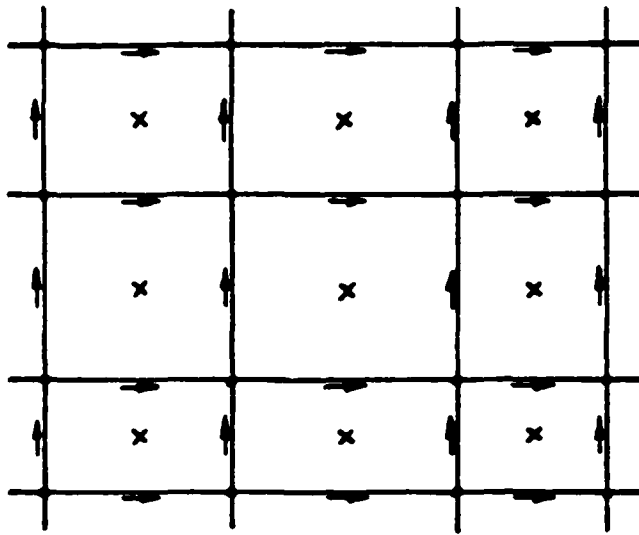
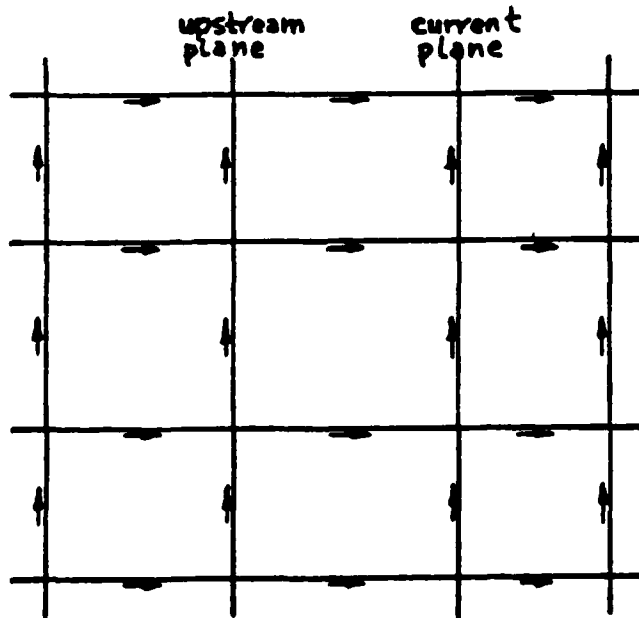


Figure 2.3 Top and side view of laser-Doppler velocimeter aligned for measurements at a bend angle $\theta = 180^\circ$. Traversing mechanism details are not shown.



(r-z) plane

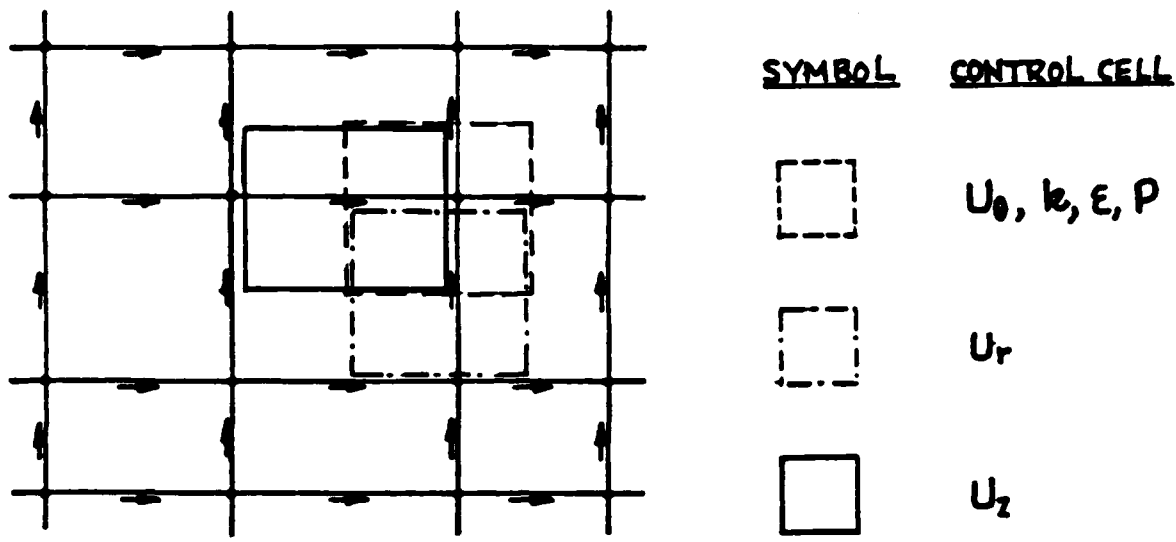
<u>SYMBOL</u>	<u>VARIABLE</u>
→	$U_z, \overline{U_0 U_z}$
↑	$U_r, \overline{U_r U_0}$
x	$\overline{U_r U_z}$
•	P, k, ϵ, U_0 $\overline{U_r U_r}, \overline{U_\theta U_\theta}, \overline{U_z U_z}$



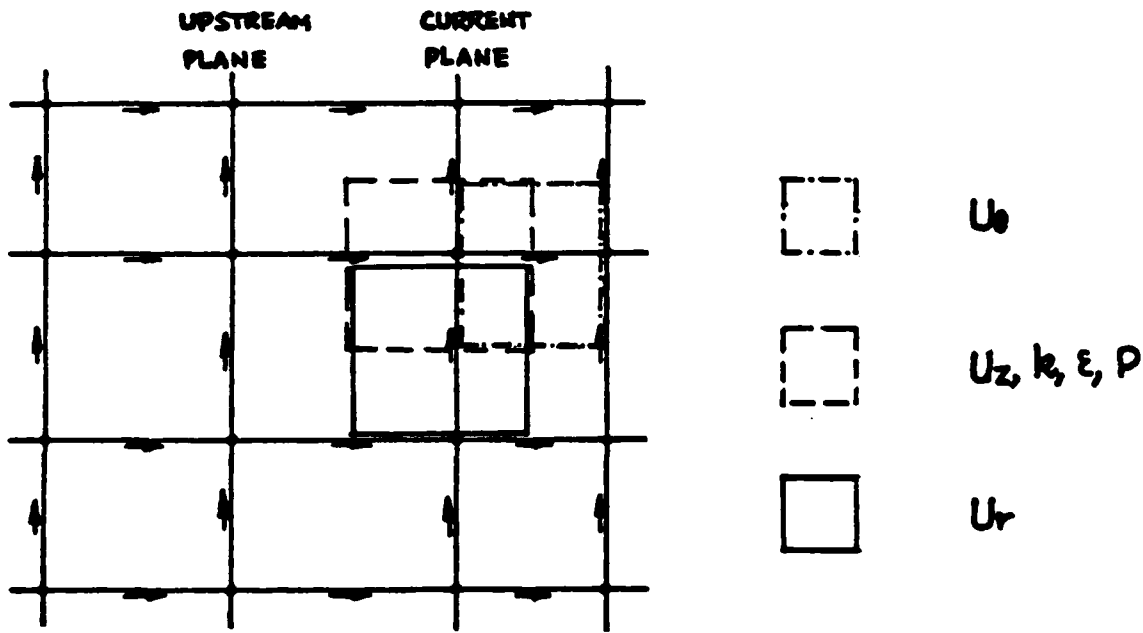
(r-θ) plane

<u>SYMBOL</u>	<u>VARIABLE</u>
→	U_θ
↑	$U_r, \overline{U_r U_\theta}$

Figure 4.1 Location of variables on the calculation grid.



(r-z) PLANE



(r-θ) PLANE

Figure 4.2 Definition of control volumes.

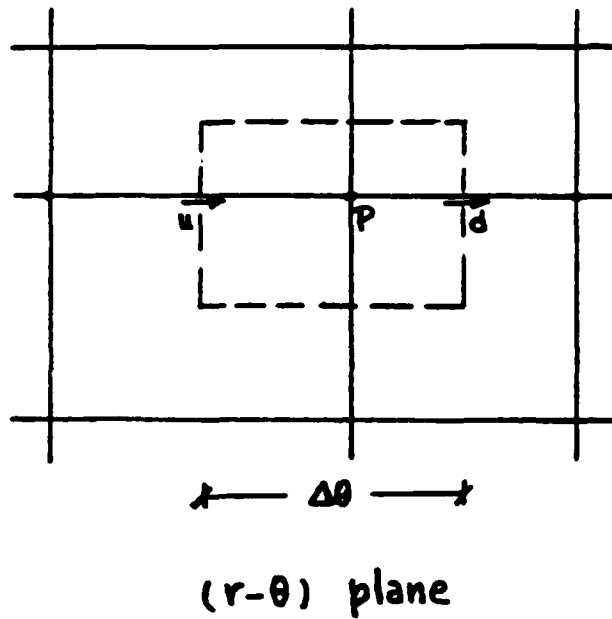
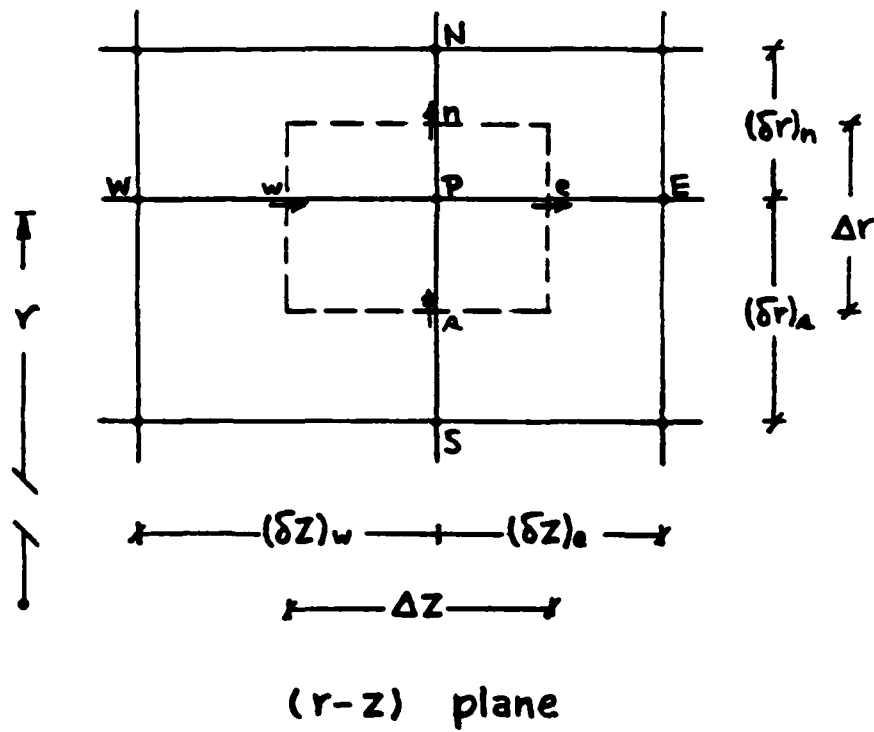


Figure 4.3 Definition of dimensions and subscripts appearing in equation (4.3.1).

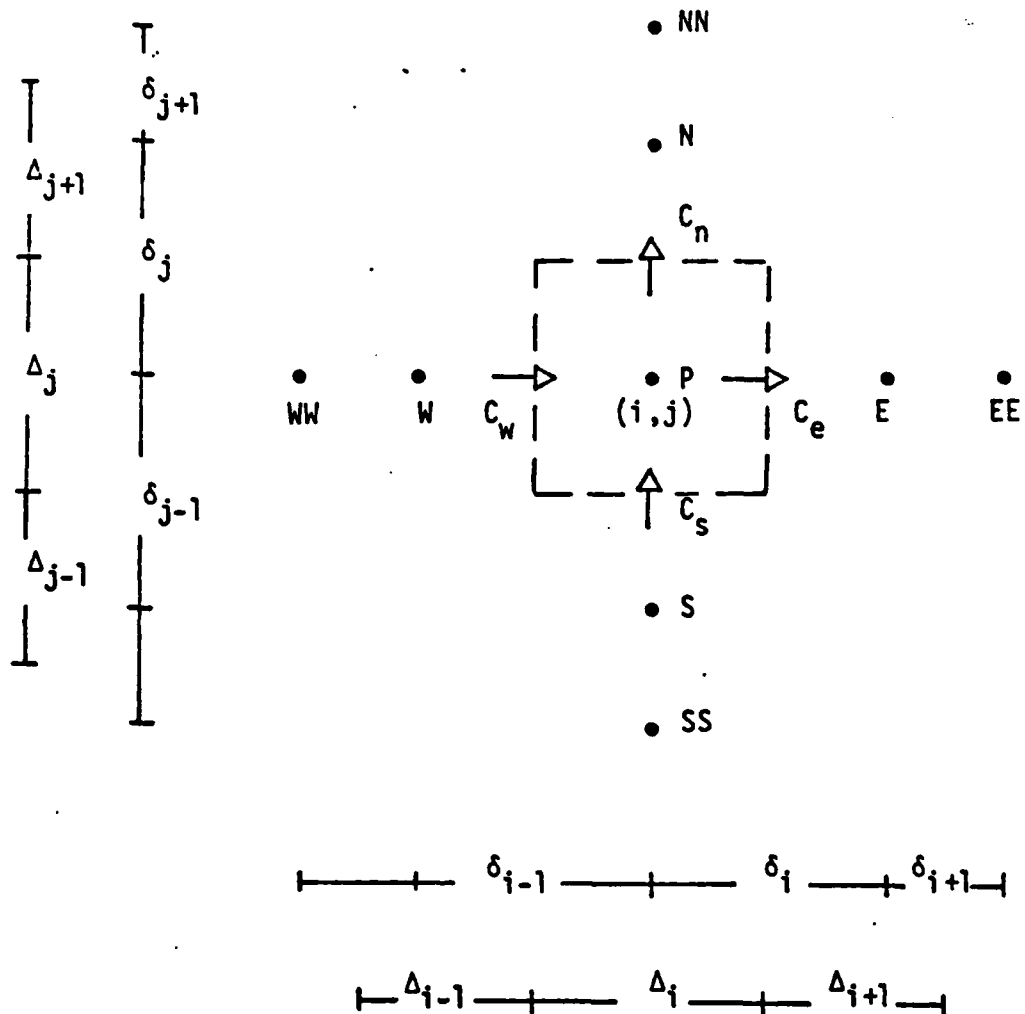


Figure 4.4 Definition of dimensions and subscripts used in the formulation of the QUICK scheme.

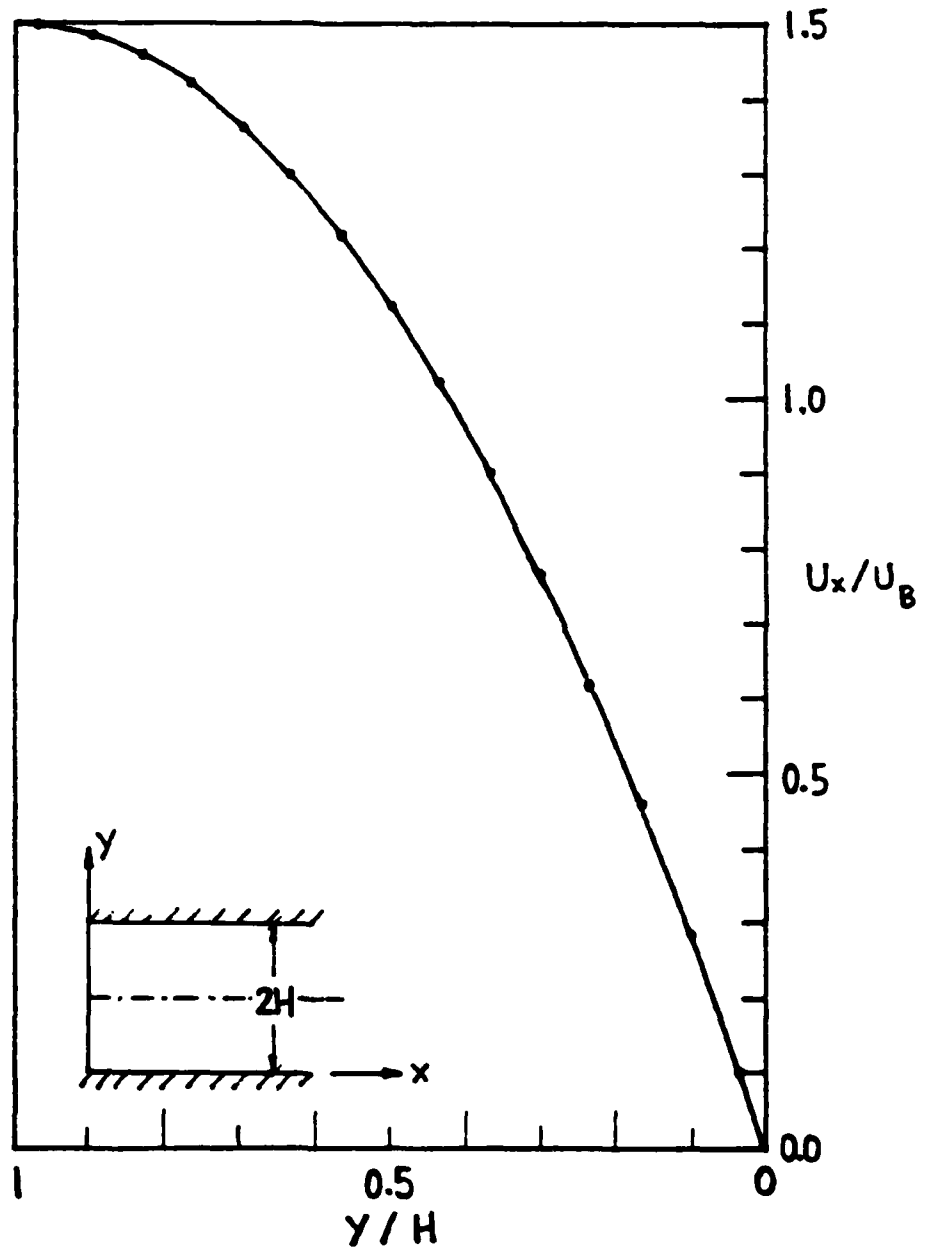


Figure 5.1 Fully developed laminar flow in a 2D straight channel. (·) HYBRID calculation; (—) exact solution.

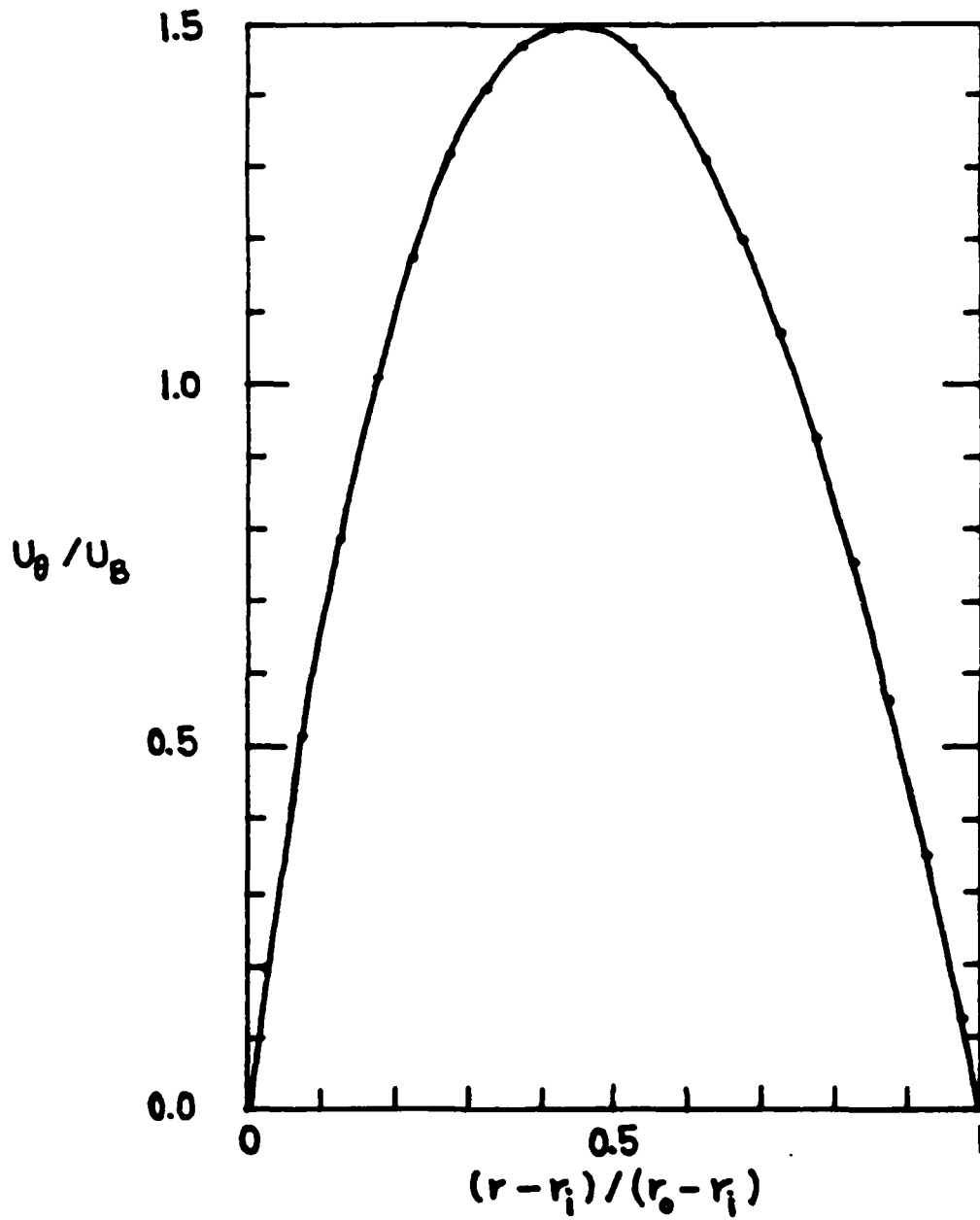


Figure 5.2 Fully developed laminar flow in a 2D curved channel of $(r_o - r_i) / r_i = 1.0$. (·) HYBRID calculations; (—) exact solution.

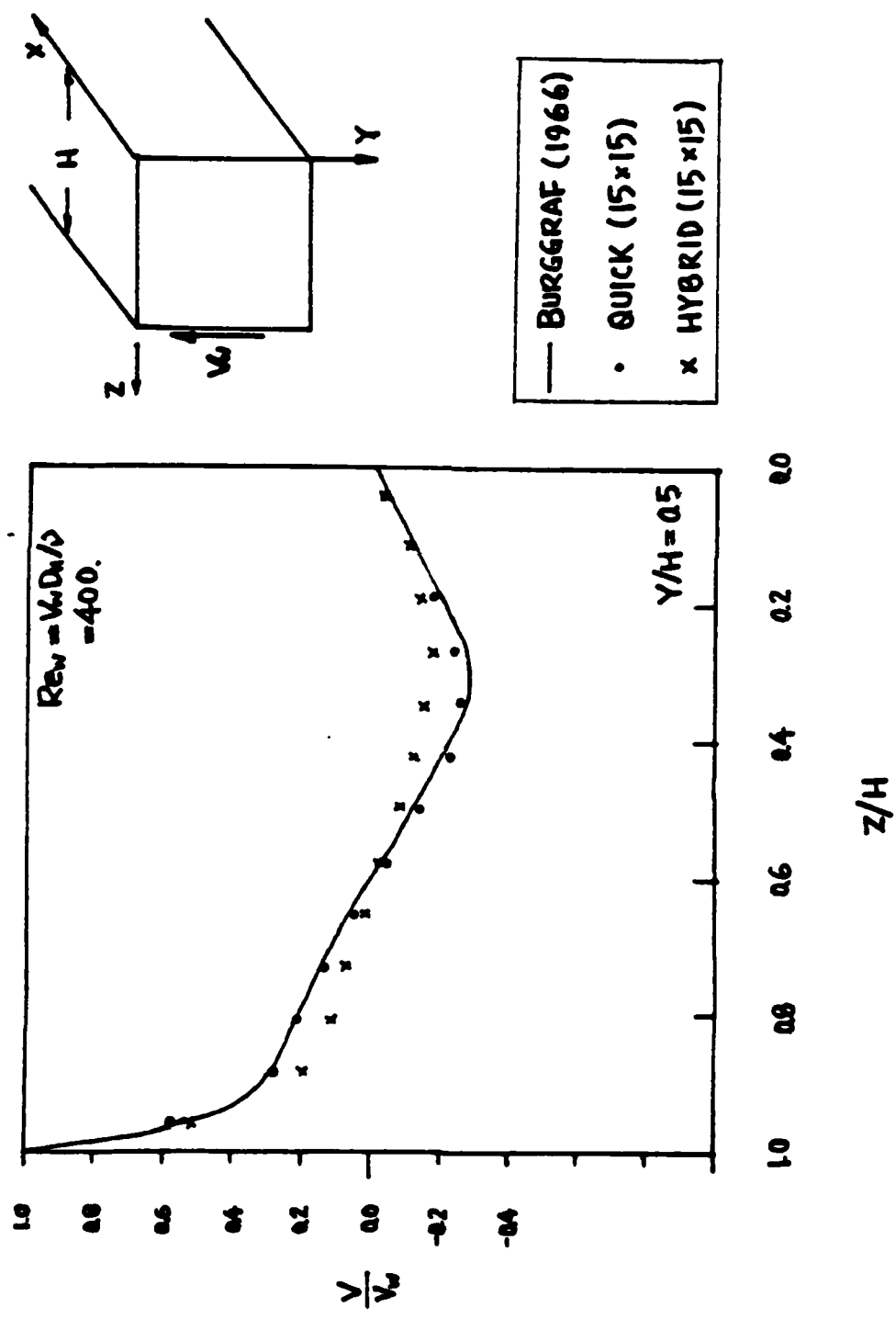


Figure 5.3 Fully developed laminar flow in a straight duct with one wall moving at a constant speed normal to the main flow direction.

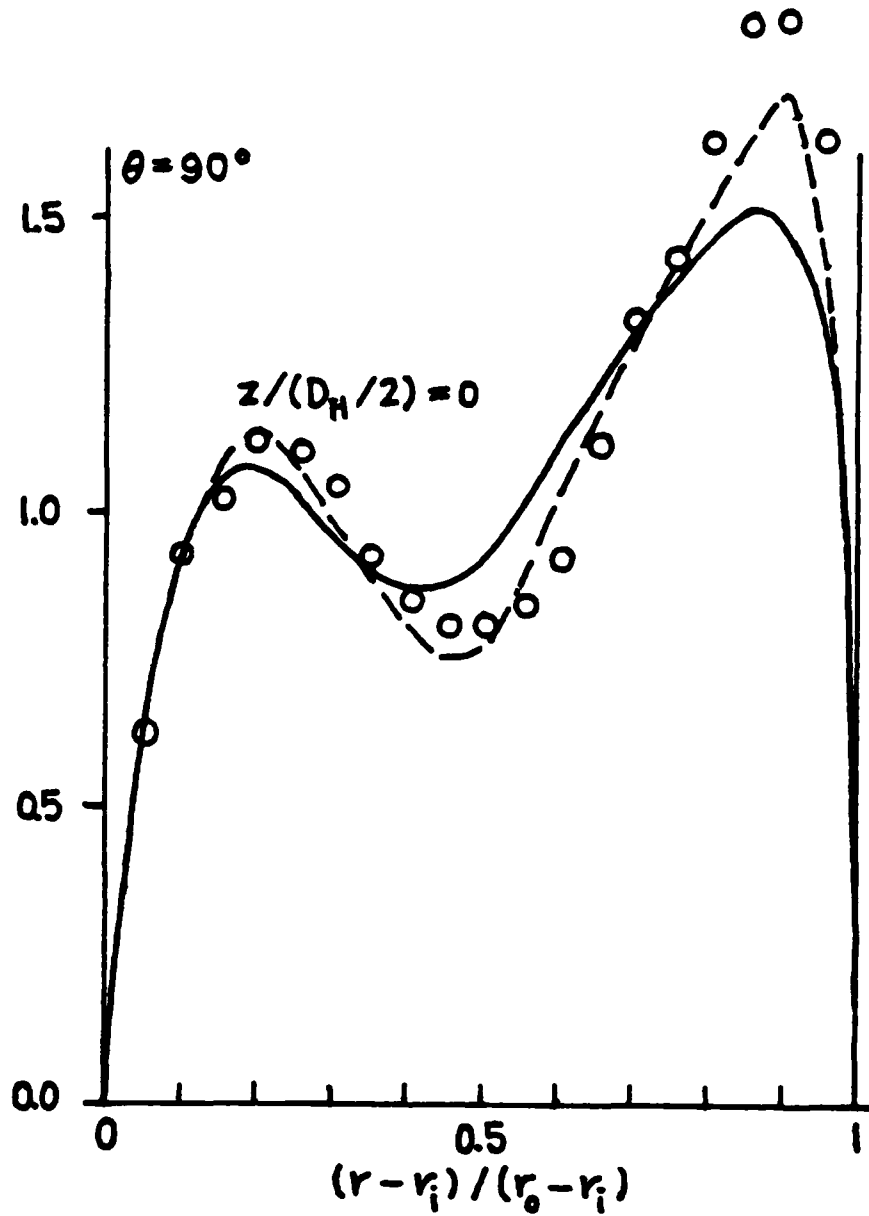


Figure 5.4 Laminar flow in a 90° curved duct of square cross-section with fully developed velocity profile near the inlet plane to the bend. (---) QUICK; (—) HYBRID; (o) measurements of Humphrey et al. [1977].

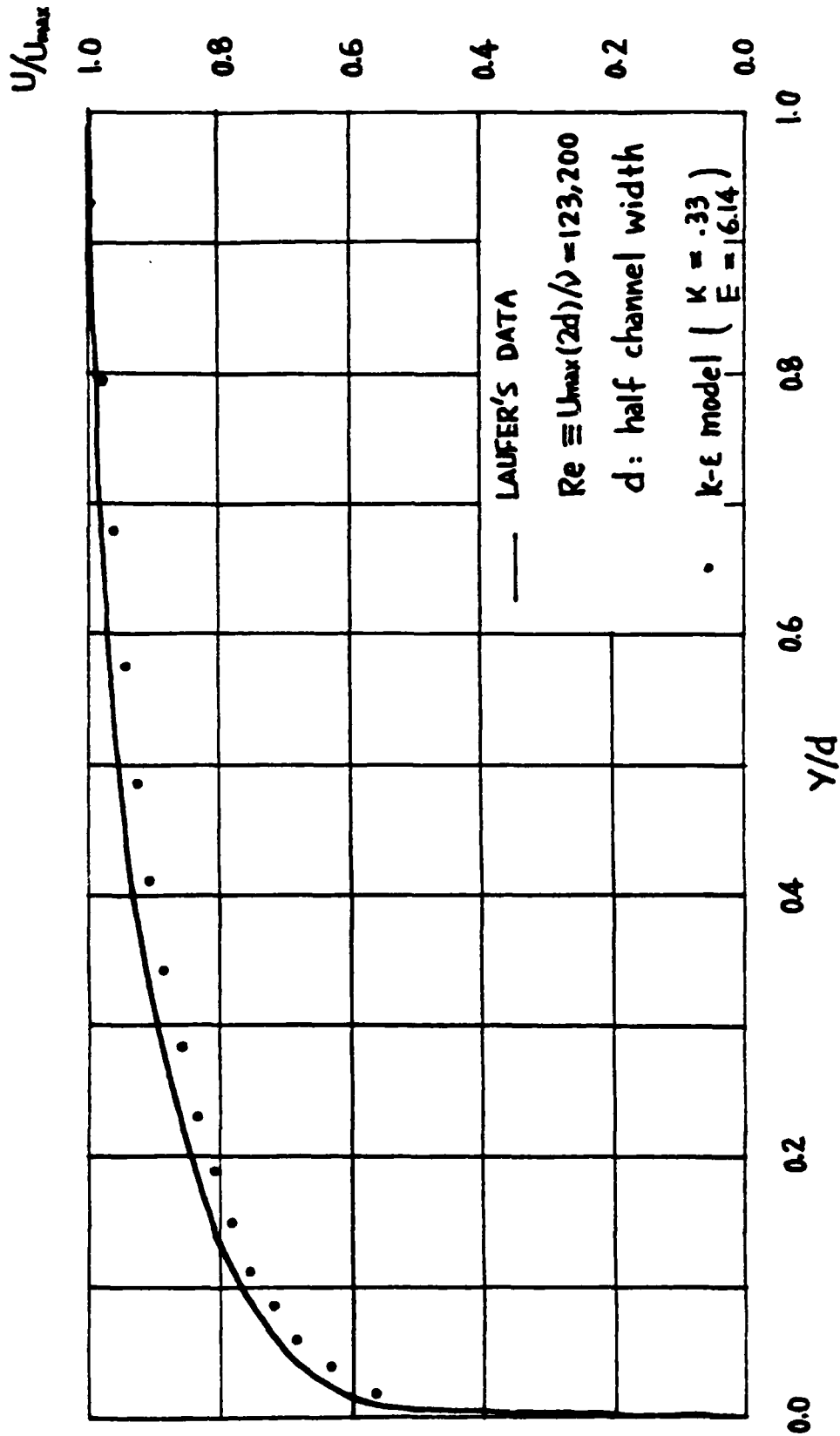


Figure 5.5 k- ϵ model calculation of fully-developed turbulent flow in a 2D straight channel; mean longitudinal velocity U/U_{max} .

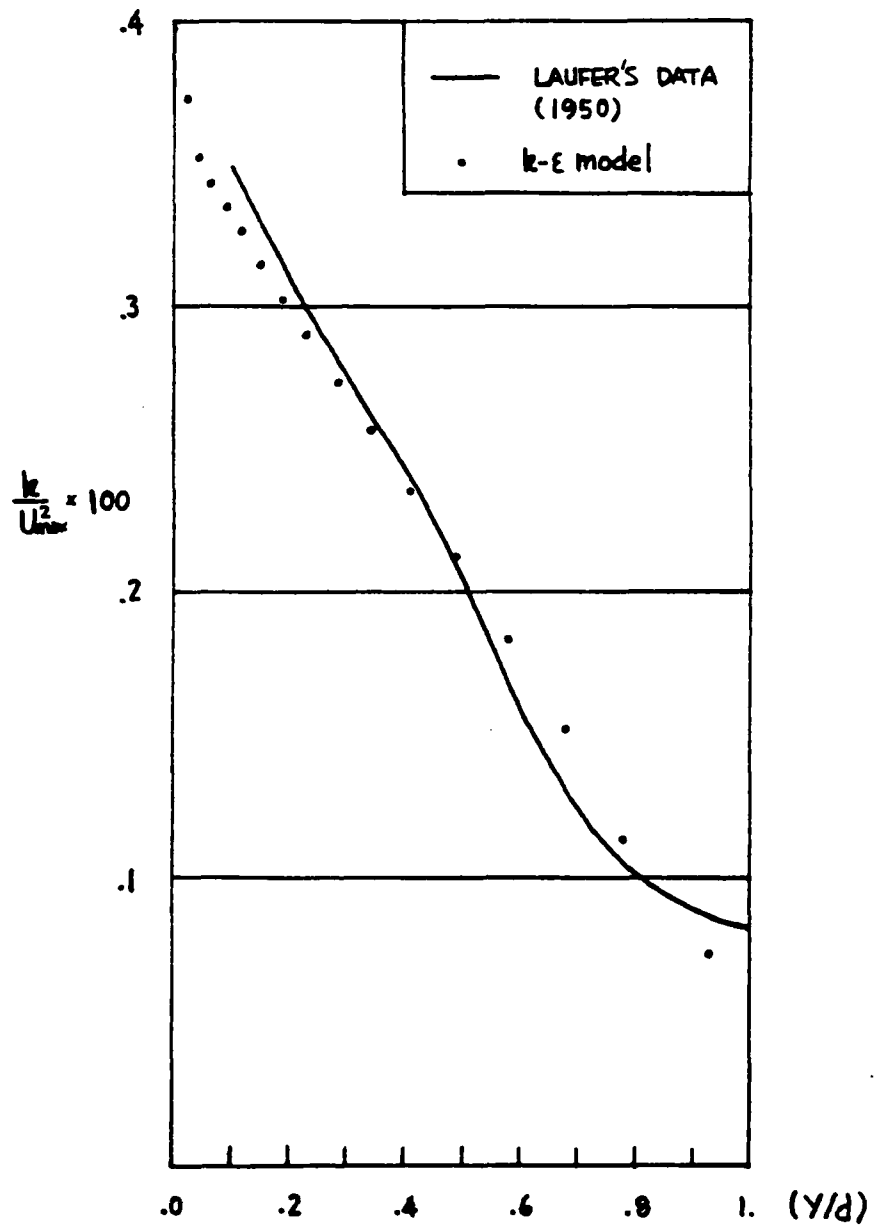


Figure 5.6 $k-\epsilon$ model calculation of fully developed turbulent flow in a 2D straight channel; turbulent energy $(k/U_{max}^2) \times 100$.

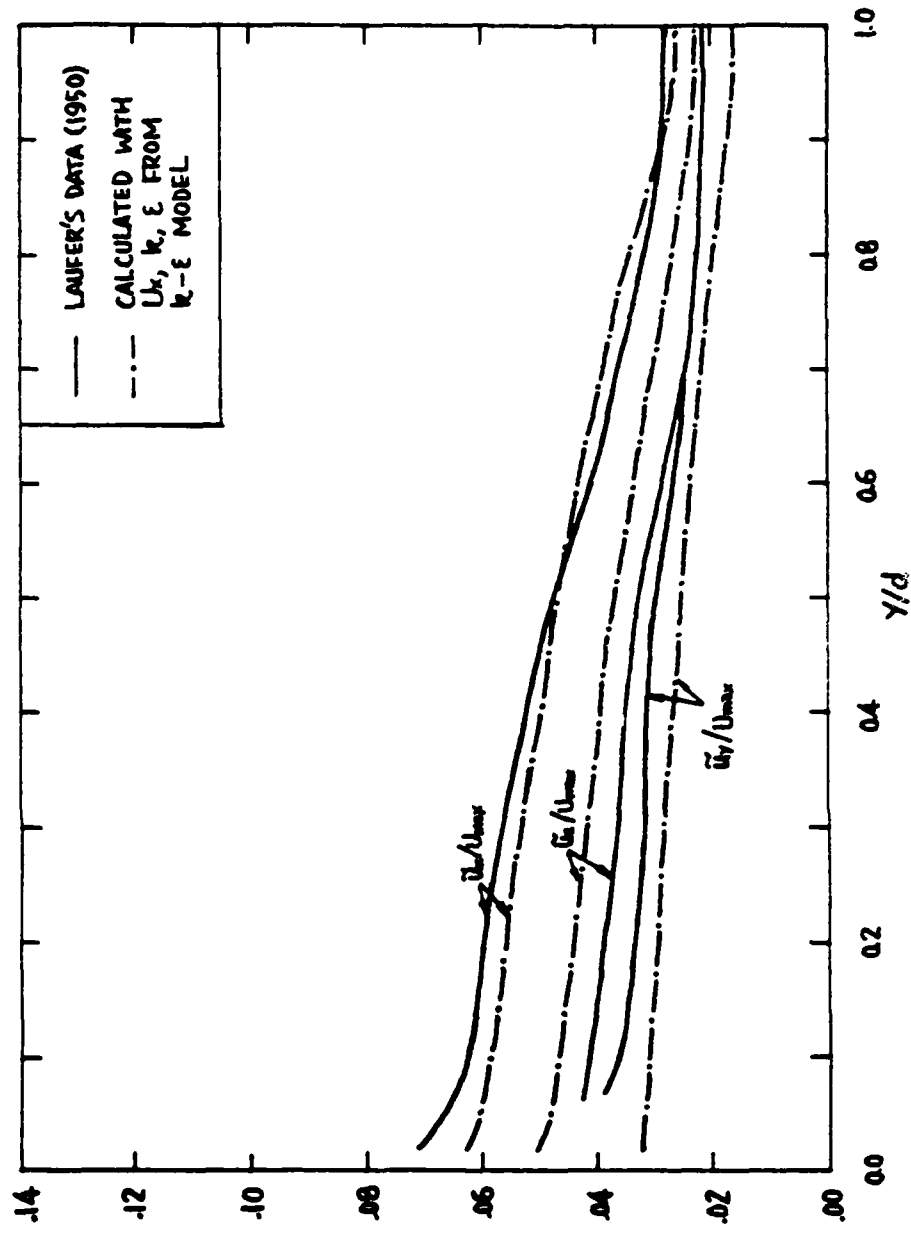


Figure 5.7 Fully developed turbulent flow in a 2D straight channel; distributions of \bar{u}_x , \bar{u}_y and \bar{u}_z calculated by using the ASM relations and U_x , k , y and ϵ from the $k-\epsilon$ model calculation.

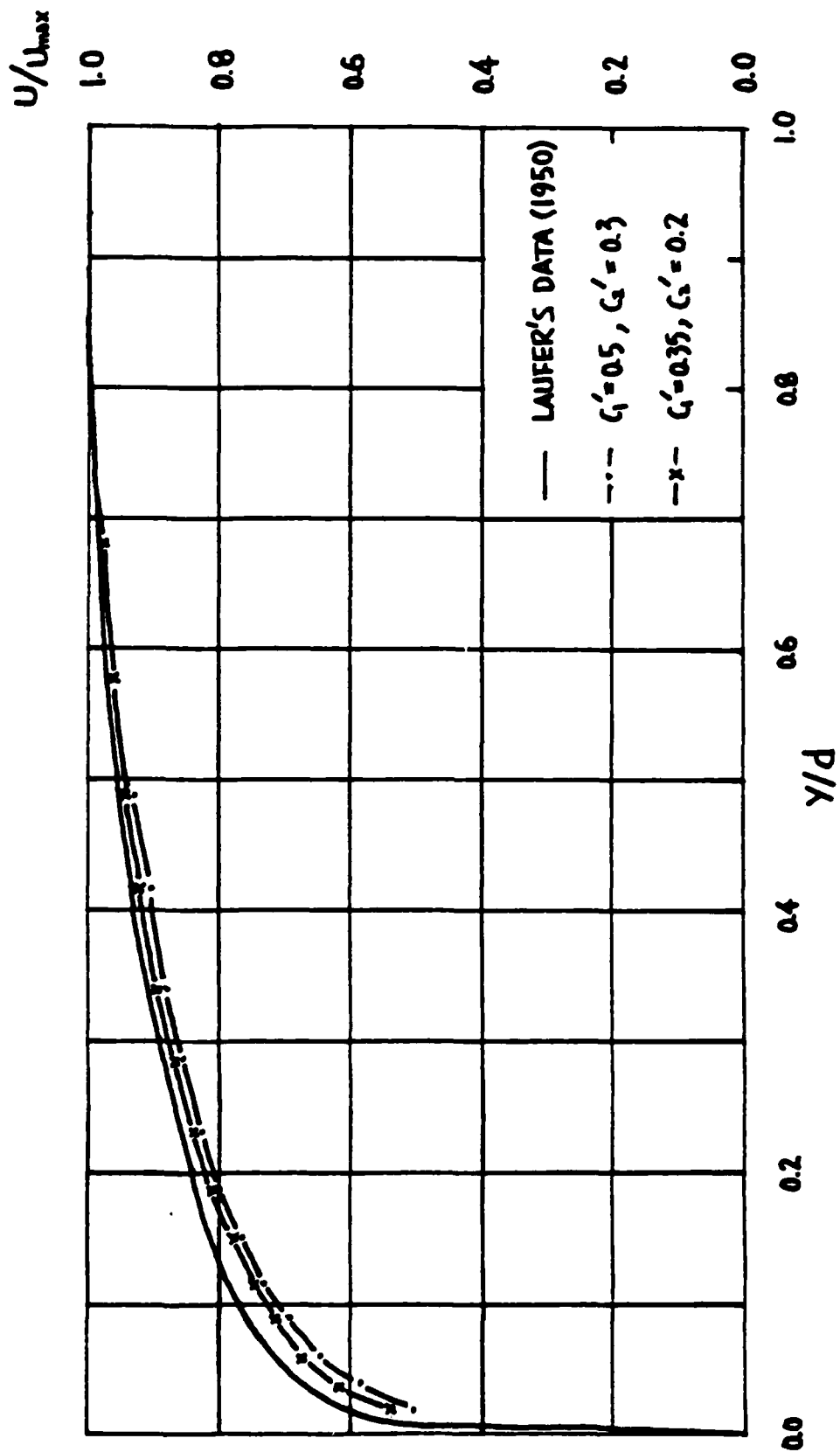


Figure 5.8 ASM calculation of fully developed turbulent flow in a 2D straight channel; mean longitudinal velocity U/U_{max} .

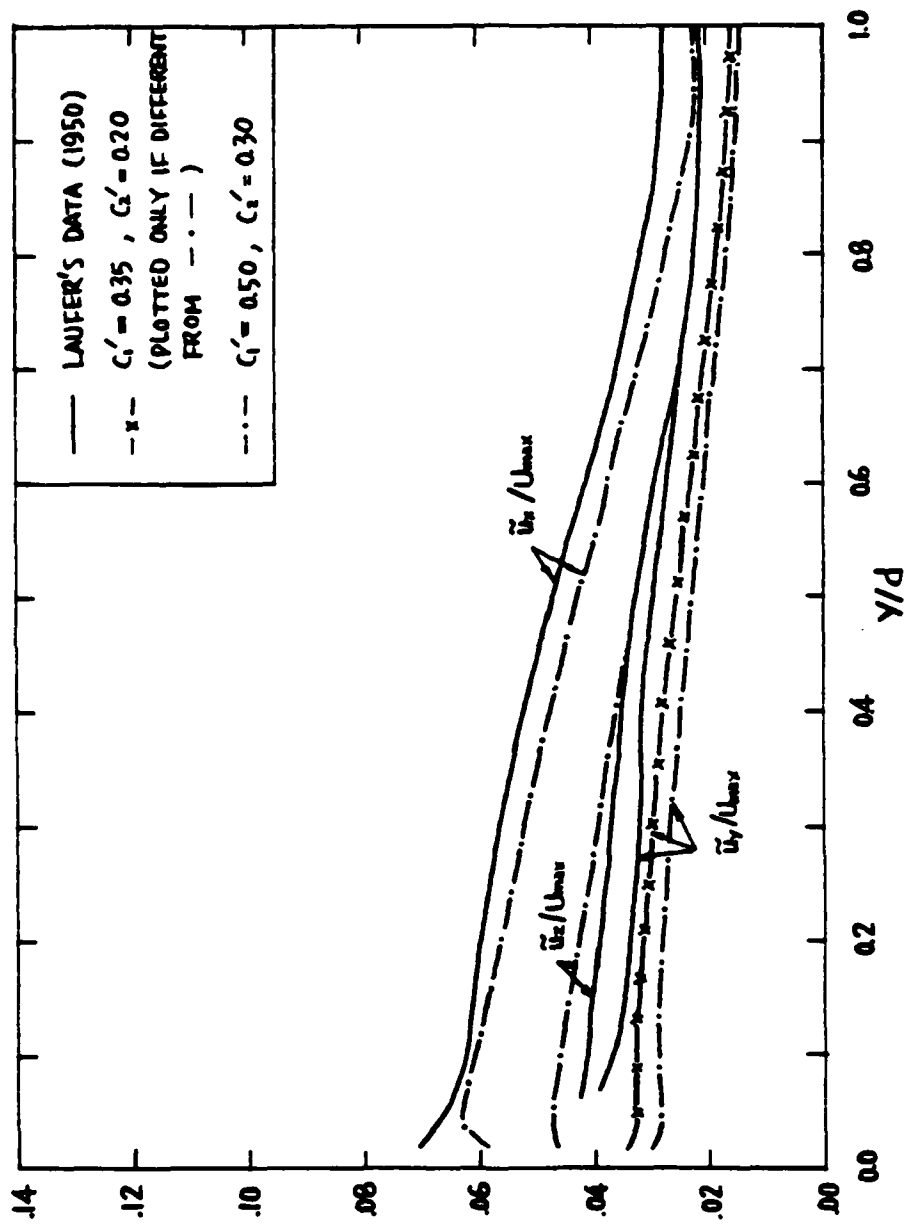


Figure 5.9 ASM calculation of fully developed turbulent flow in a 2D straight channel; \bar{u}_x/U_{max} , \bar{u}_y/U_{max} and \bar{u}_z/U_{max} .

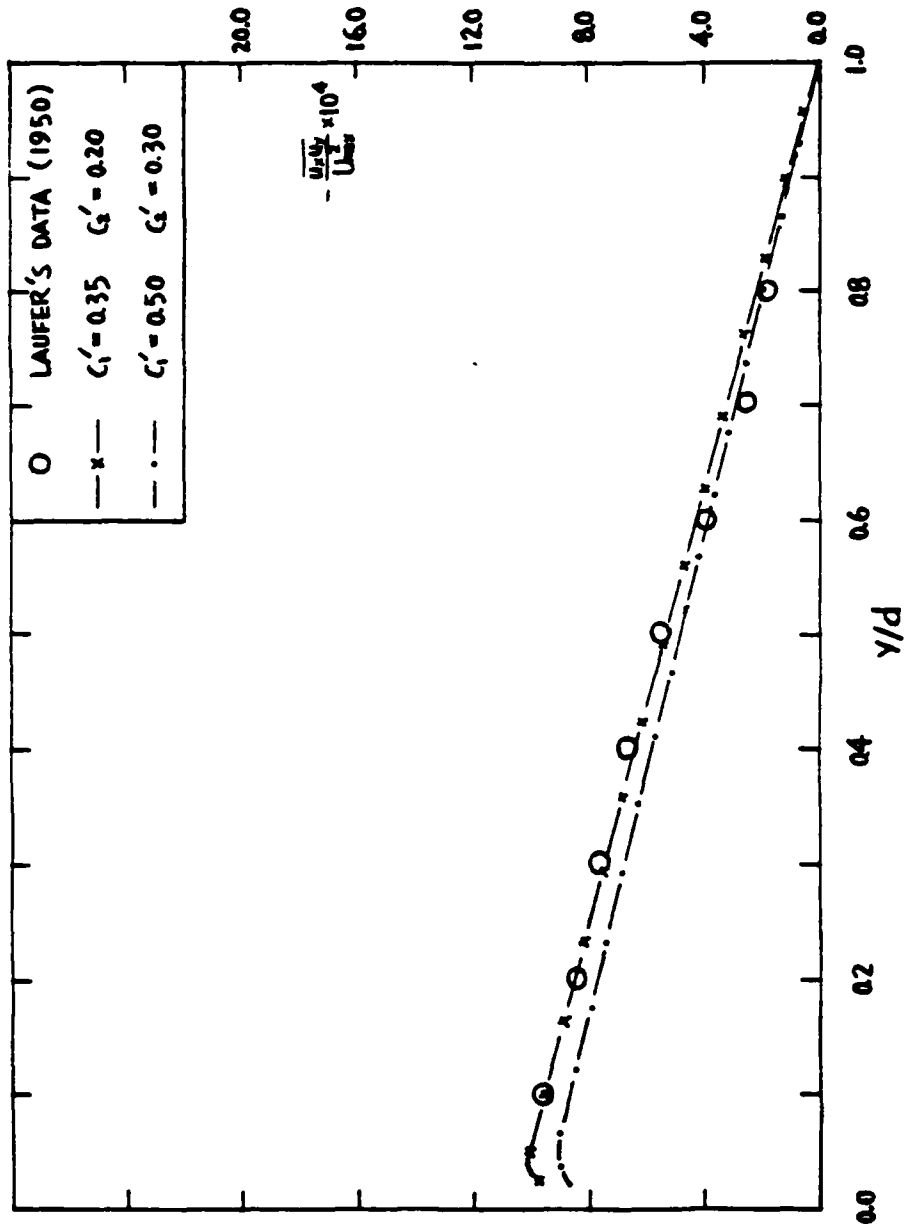


Figure 5.10 ASM calculation of fully developed turbulent flow in a 2D straight channel; $\frac{u_x' y'}{U_{max}^2}$.

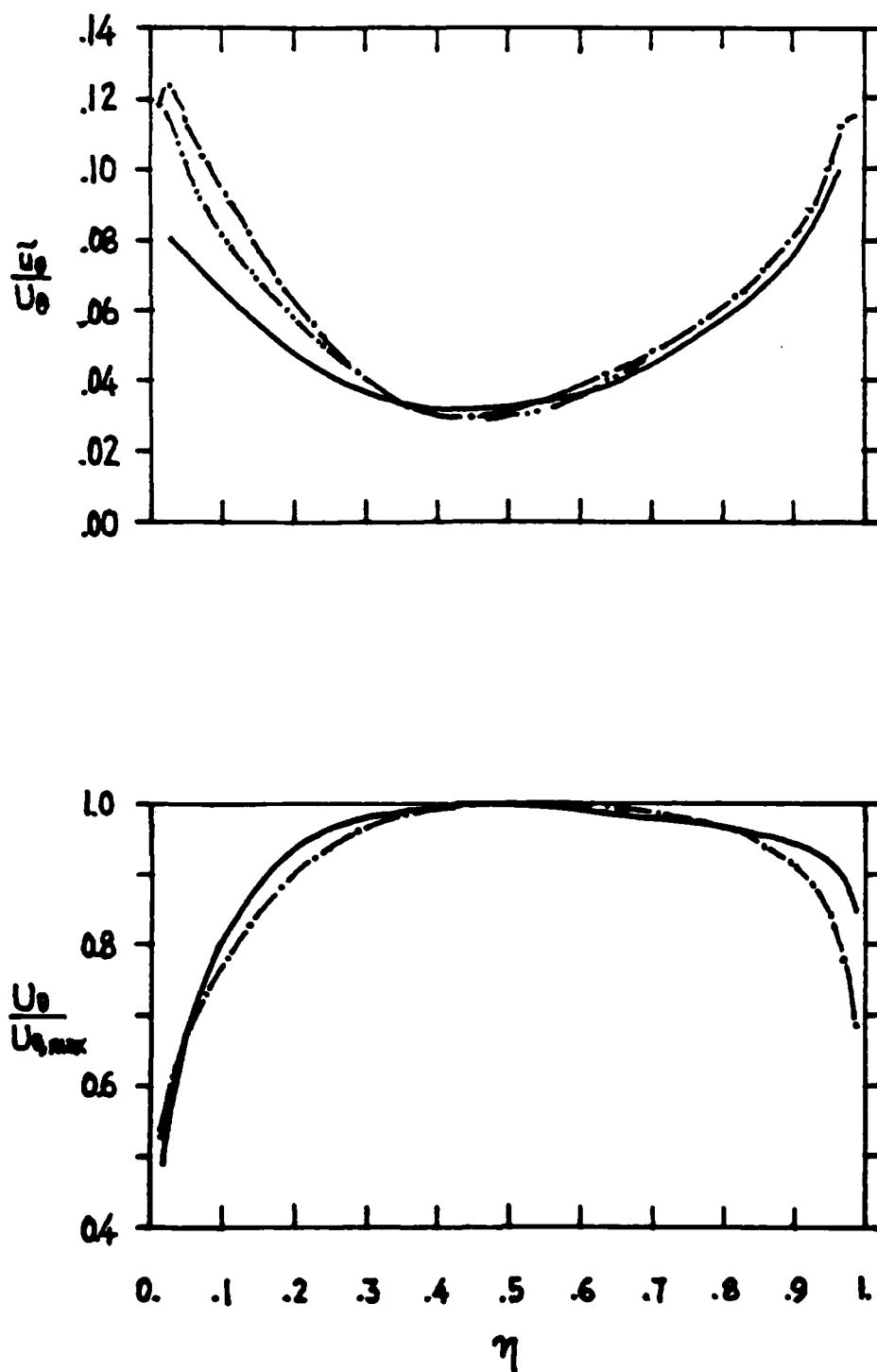


Figure 5.11 ASM calculation of fully developed turbulent flow in a 2D curved channel; \bar{u}_θ/U_θ and $U_\theta/U_{\theta,max}$: (—) measurements of Eskinazi and Yeh [1956]; (---) ASM calculation; (-.-) ASM calculation with non-symmetric f-function of Humphrey and Pourahmadi [1982].

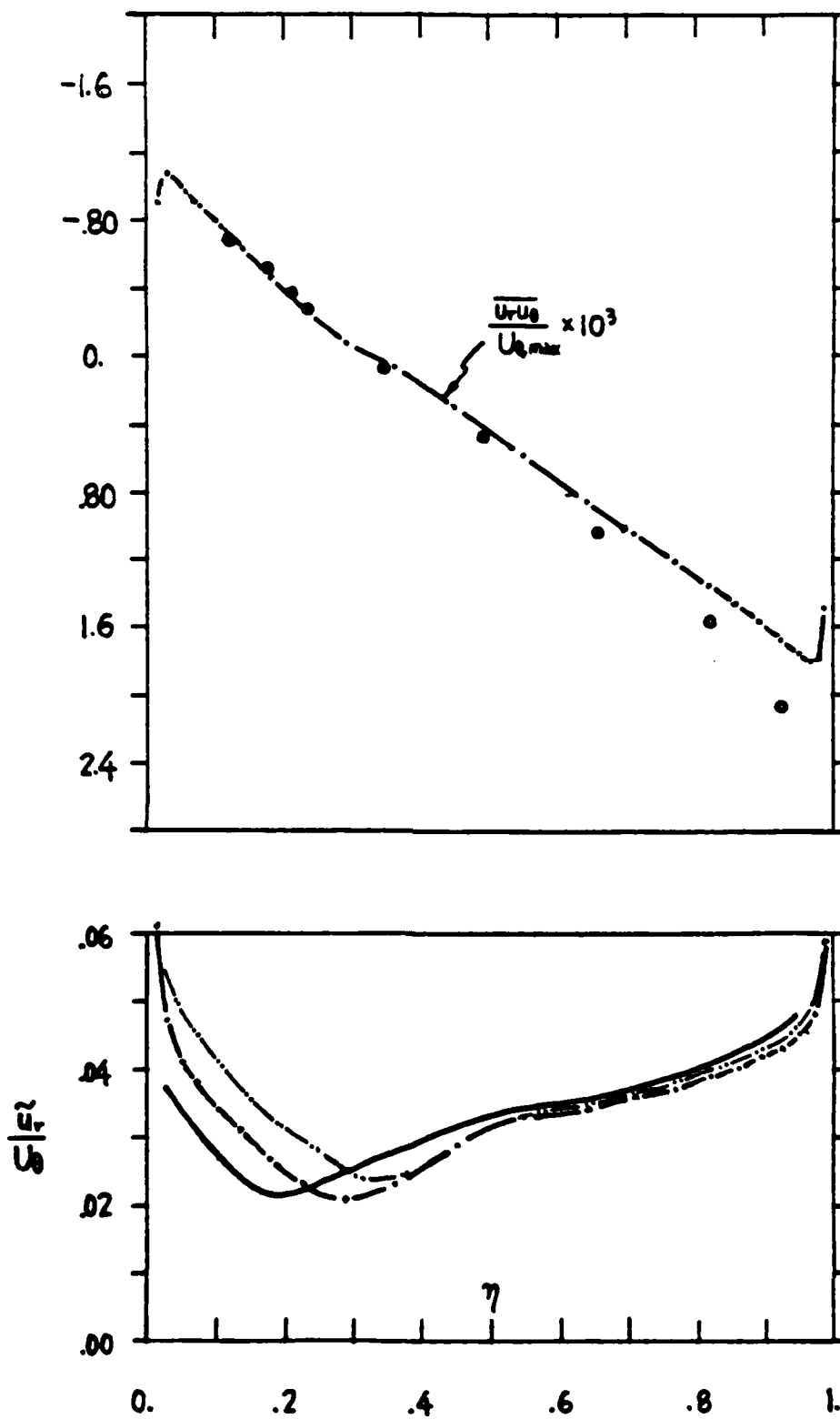


Figure 5.12 ASM calculation of fully developed turbulent flow in a 2D curved channel; $\frac{\overline{u_r u_\theta}}{U_{\theta, \max}}$ and $\frac{\overline{u_r}}{U_\theta}$: (— and o) measurements; (---) ASM calculation; (-.-) ASM calculation with non-symmetric f-function of Humphrey and Pourahmadi [1982].

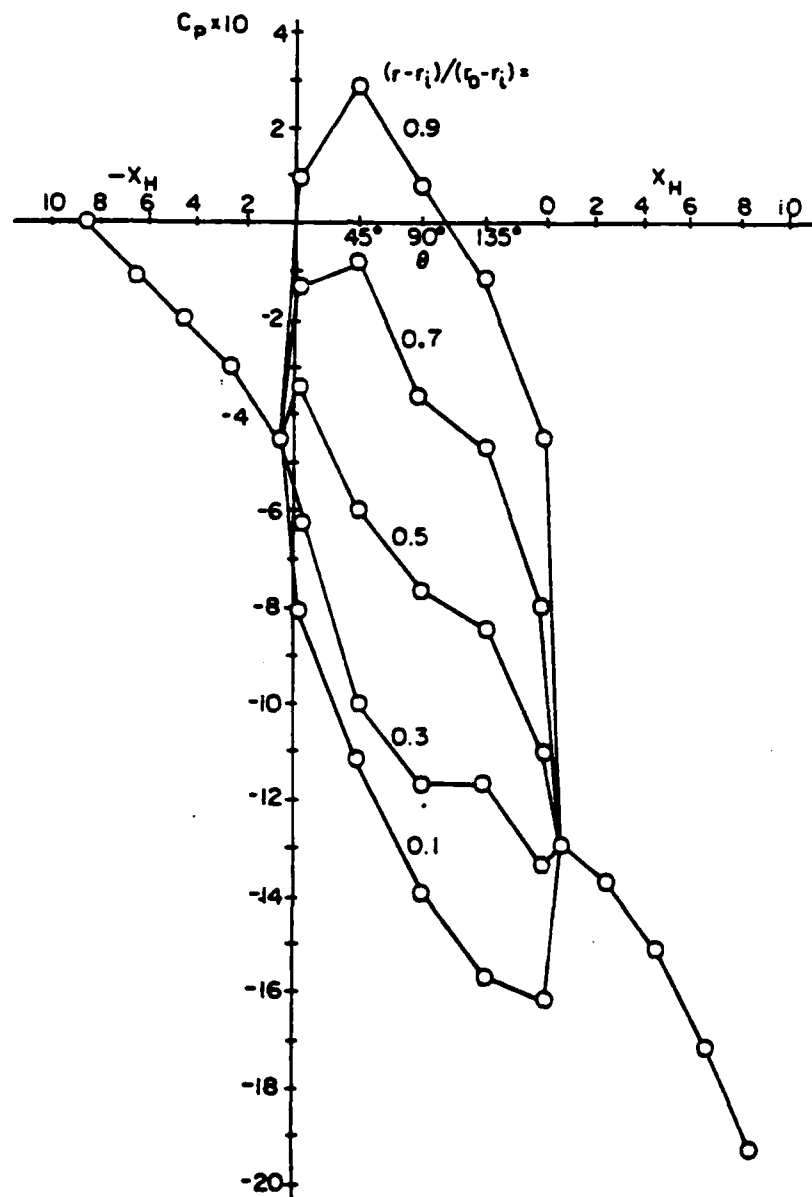


Figure 6.1 Distribution of pressure coefficient ($C_p = \Delta P / \rho U_B^2$) in the bend and tangents for conditions of the experiment: $Re = 56,700$, $R_c/D_H = 3.35$ and $De = 21,900$. Measurements made through pressure taps on side walls of test section components.

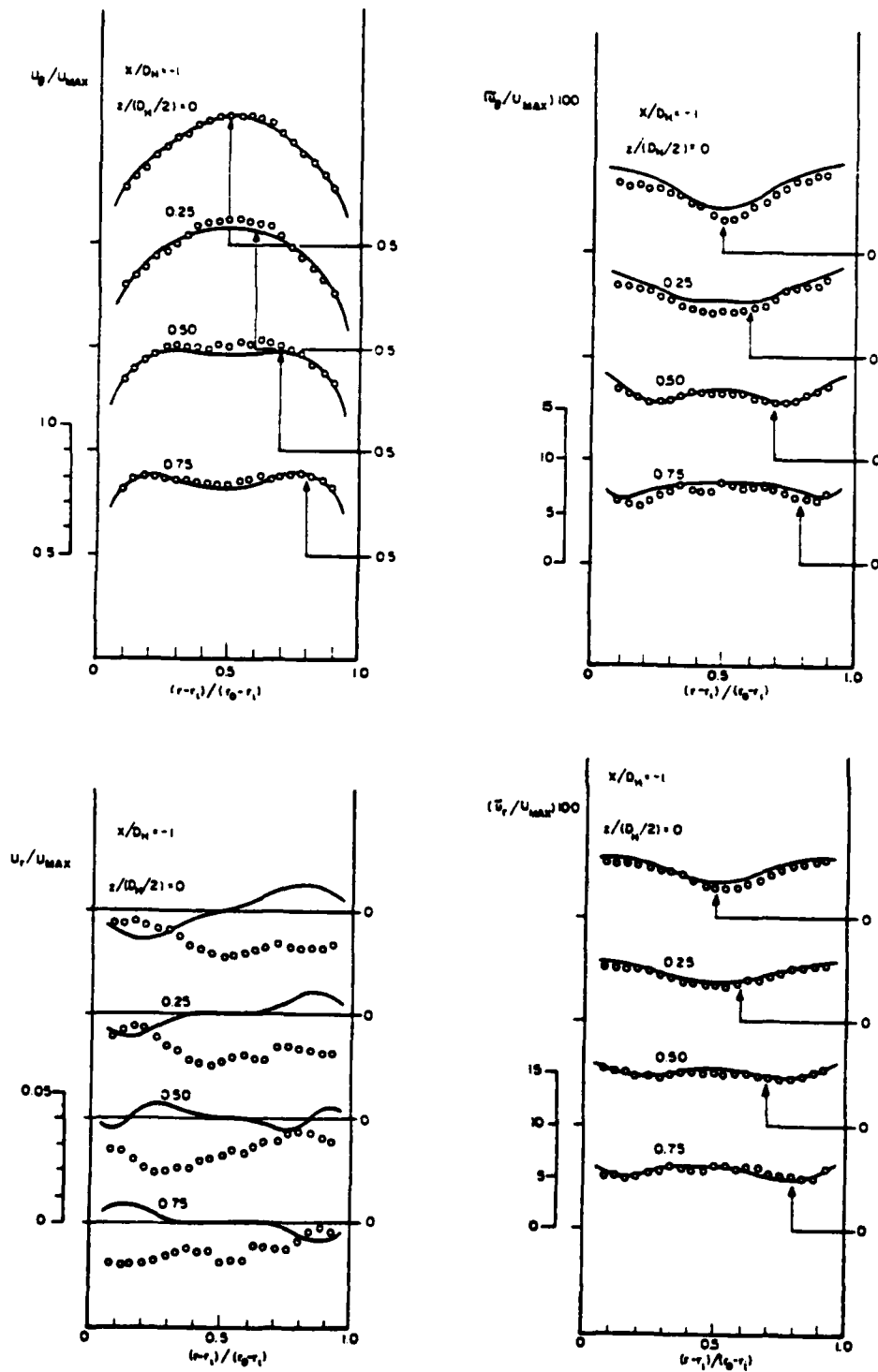


Figure 6.2 Comparison between turbulent flow measurements of mean velocity and normal stress from this work (o) at $X_H = -1$ and measurements by Melling and Whitelaw (—) after a development length of $36.8 D_H$.

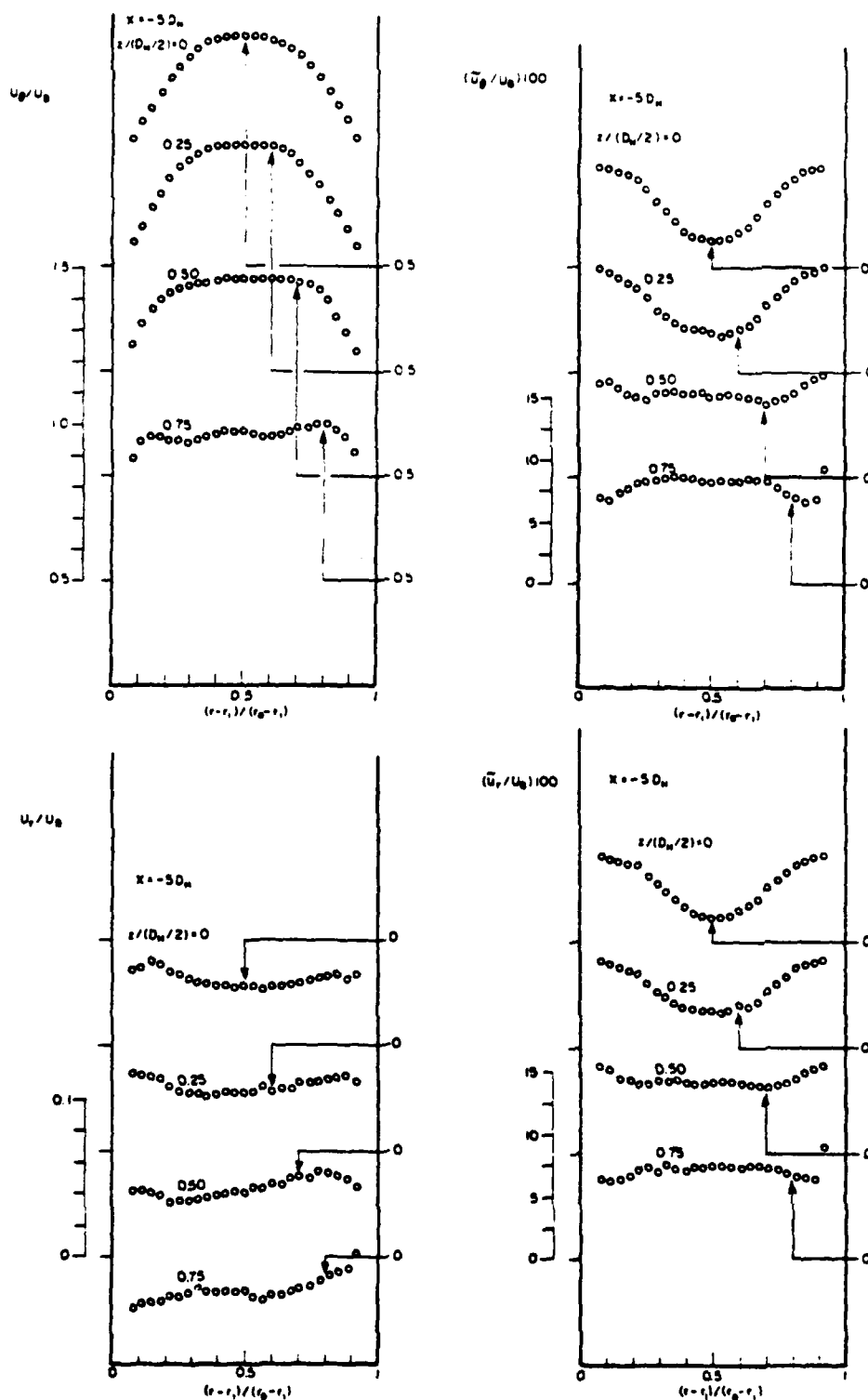


Figure 6.3 Turbulent flow measurements of mean velocity and normal stress in the upstream tangent at $X_H = -5$.

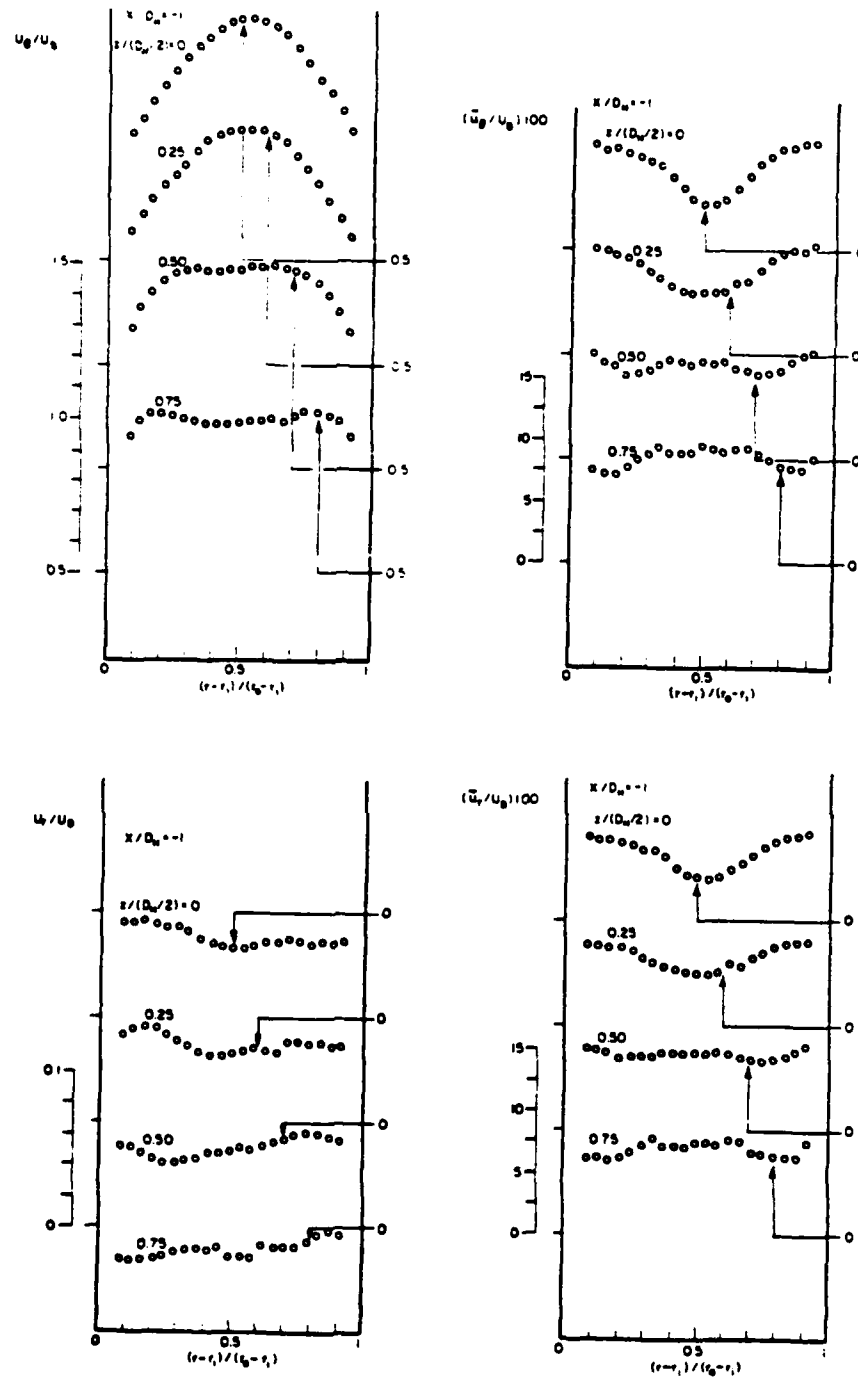


Figure 6.4 Turbulent measurements of mean velocity and normal stress in the upstream tangent at $X_H = -1$.

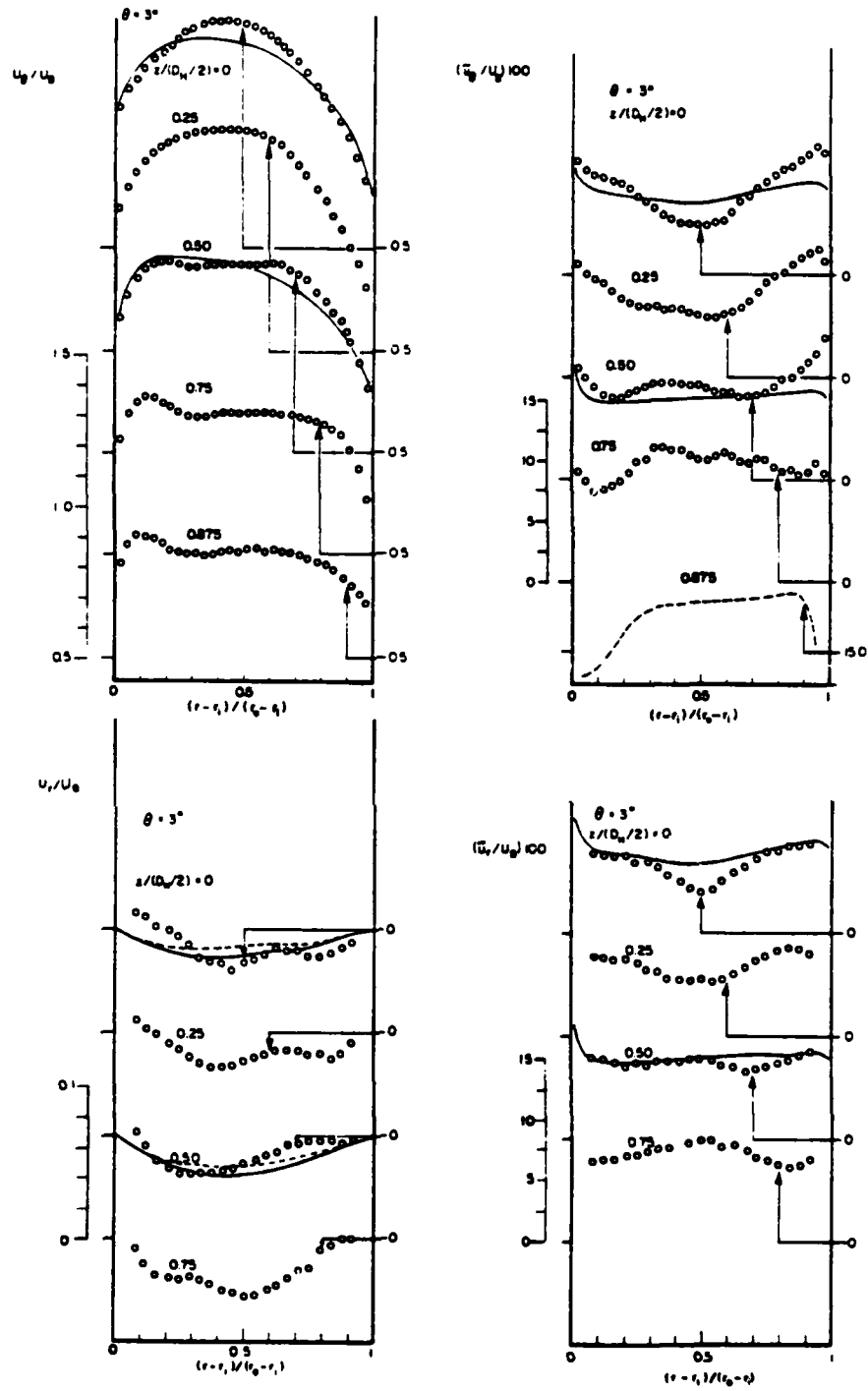


Figure 6.5 Turbulent flow measurements and k- ϵ model calculations of mean velocity and normal stress in the bend at $\theta = 3^\circ$: (—) HYBRID, (---) QUICK; dashed line at 0.875 is best fit to measurements.

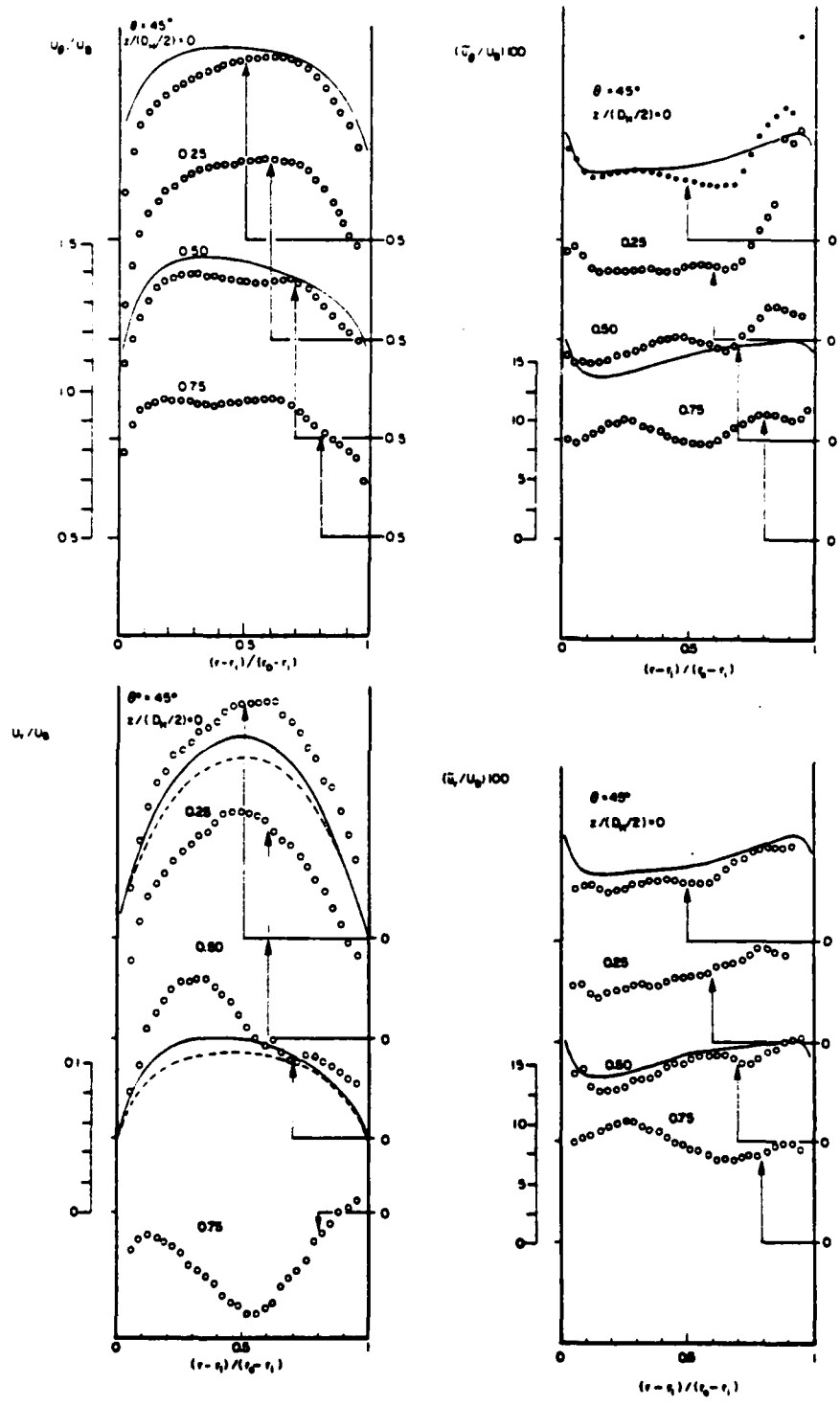


Figure 6.6 Turbulent flow measurements and k- ϵ model calculations of mean velocity and normal stress in the bend at $\theta = 45^\circ$: (—) HYBRID, (---) QUICK.

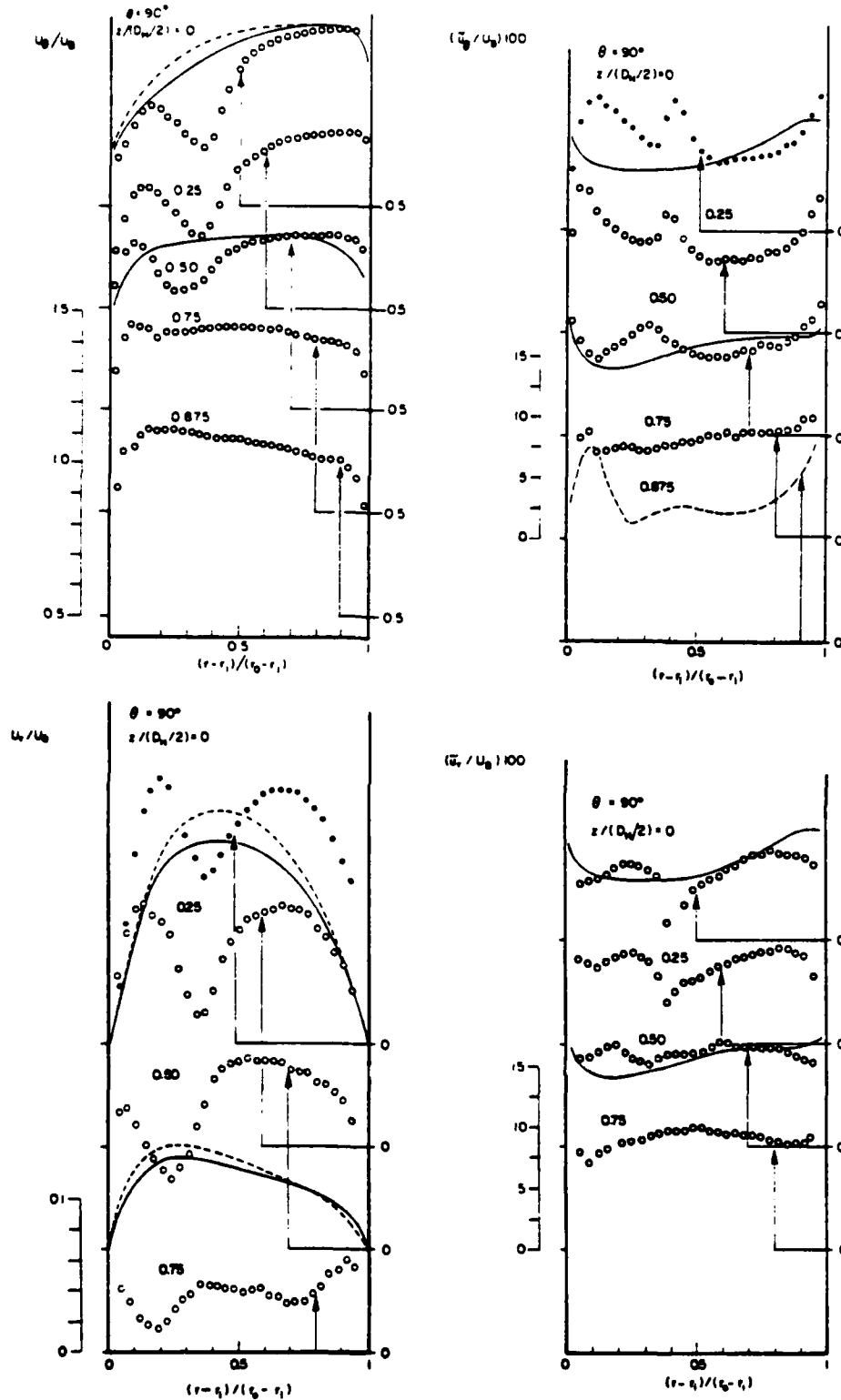


Figure 6.7 Turbulent flow measurements and k- ϵ model calculations of mean velocity and normal stress in the bend at $\theta = 90^\circ$: (—) HYBRID, (---) QUICK; dashed line at 0.875 is best fit to measurements.

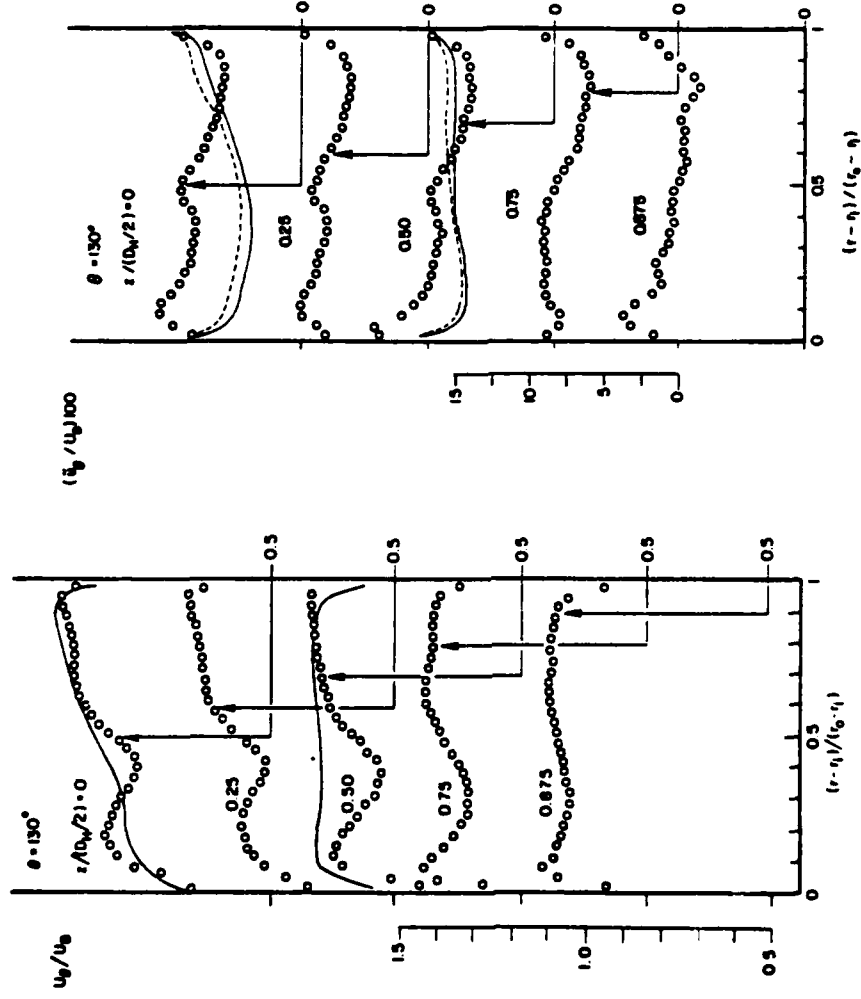


Figure 6.8 Turbulent flow measurements and k-ε model calculations of mean velocity and normal stress in the bend at $\theta = 130^\circ$; (—) HYBRID, (---) QUICK.

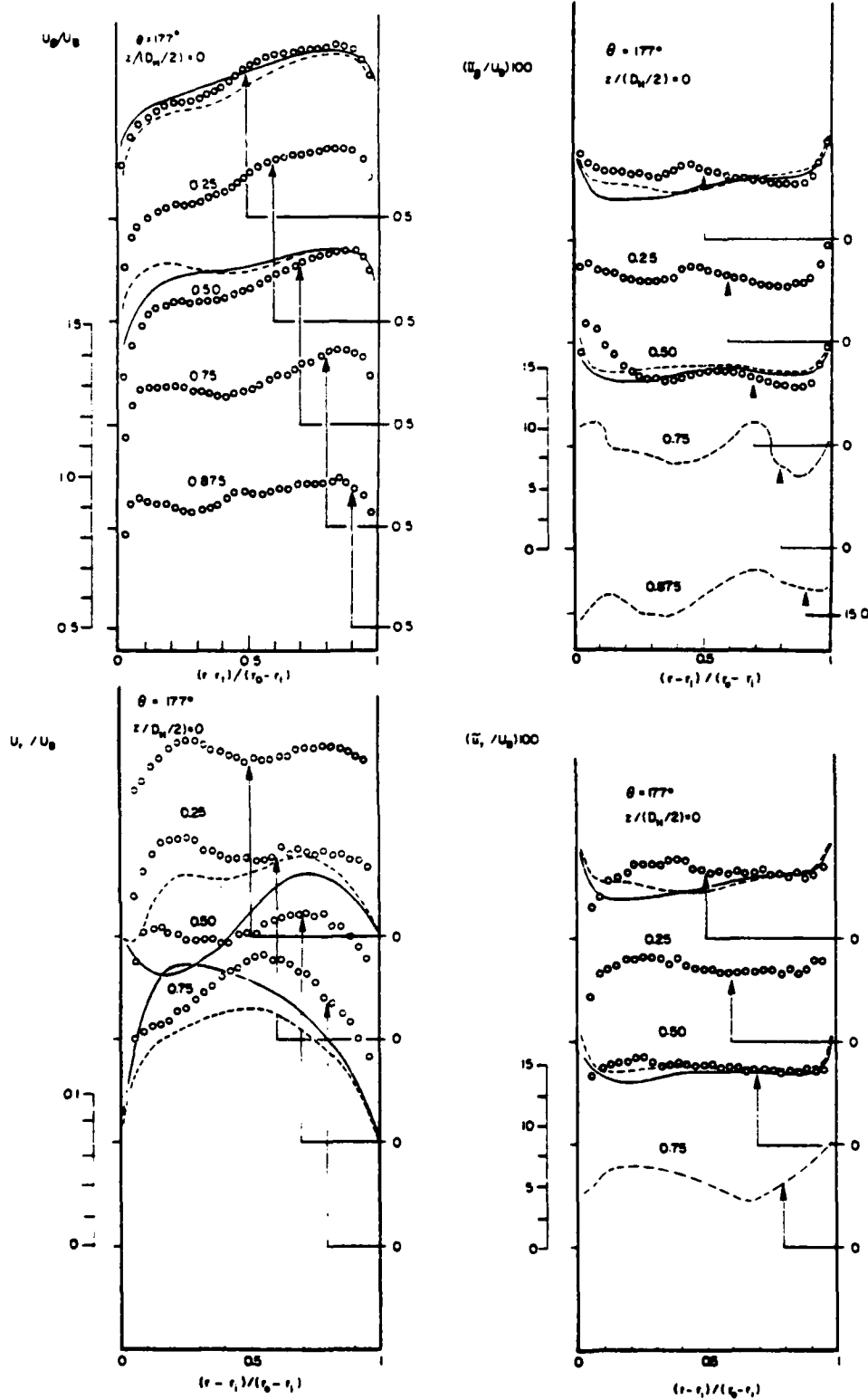


Figure 6.9 Turbulent flow measurements and $k-\epsilon$ model calculations of mean velocity and normal stress in the bend at $\theta = 177^\circ$; (—) HYBRID, (---) QUICK; dashed lines at 0.75 and 0.875 are best fits to measurements.

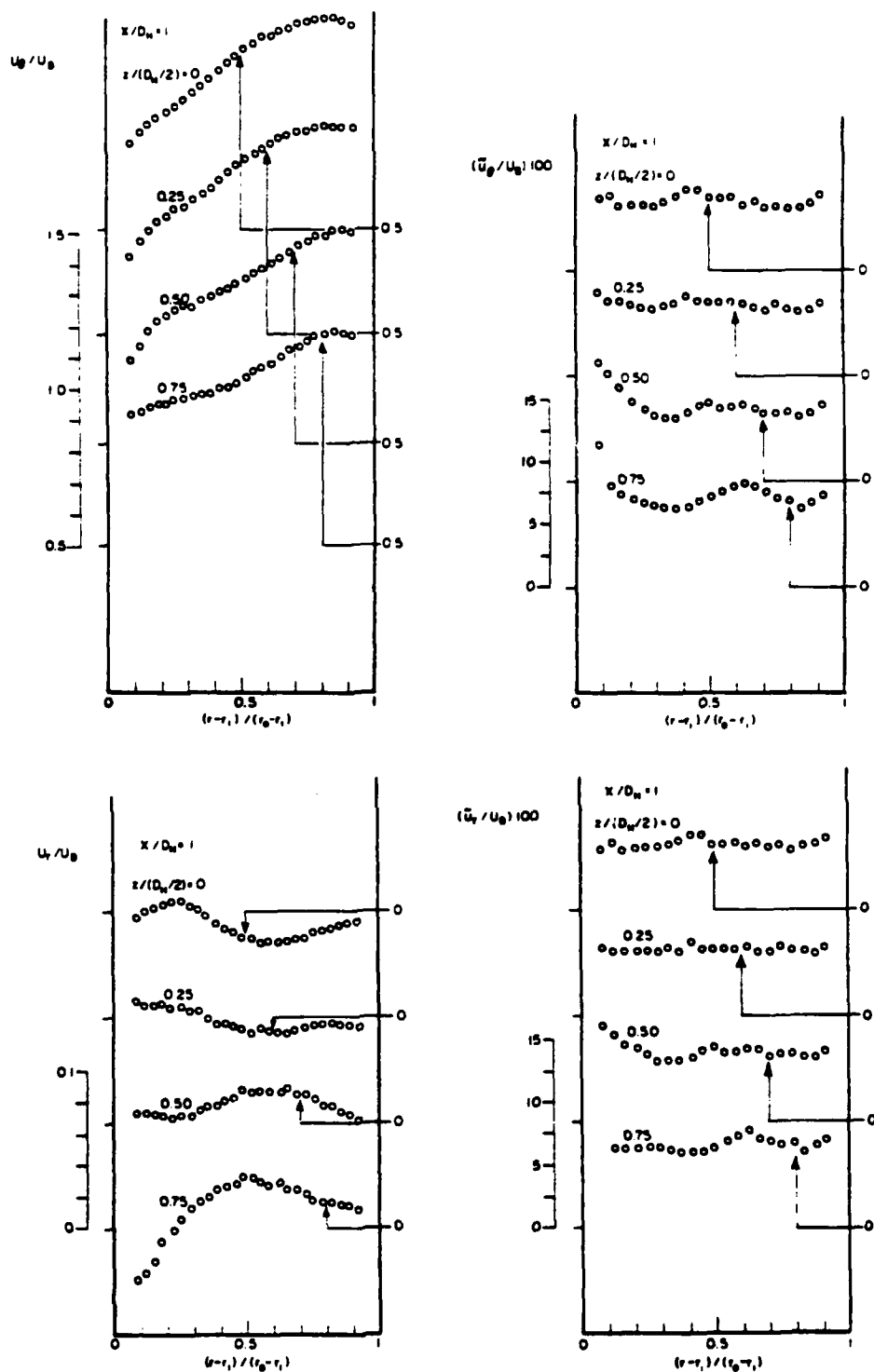


Figure 6.10 Turbulent flow measurements of mean velocity and normal stress in the downstream tangent at $X_H = 1$.

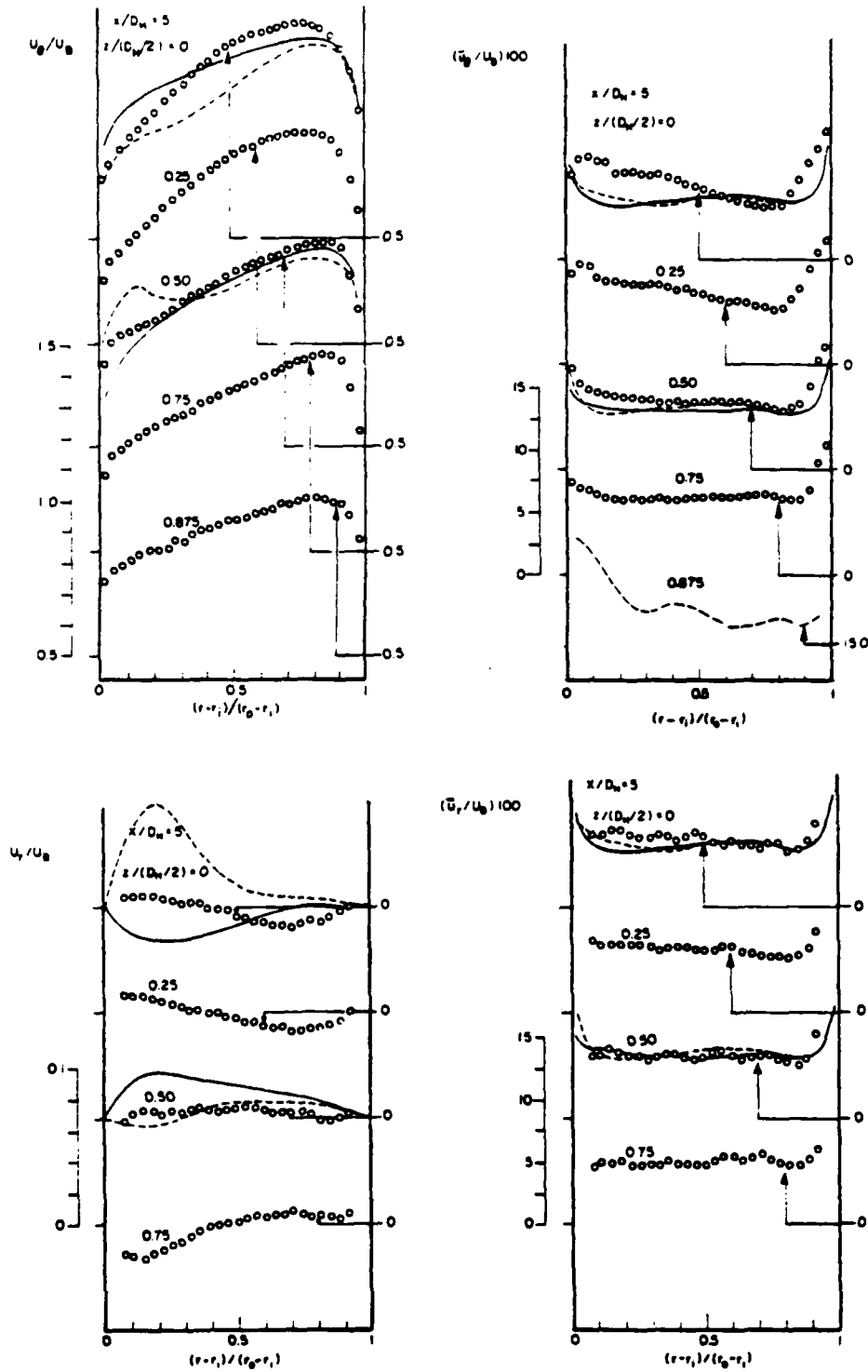


Figure 6.11 Turbulent flow measurements and $k-\epsilon$ model calculations of mean velocity and normal stress in the downstream tangent at $X_H = 5$: (—) HYBRID, (---) QUICK; dashed line at 0.875 is best to fit measurements.

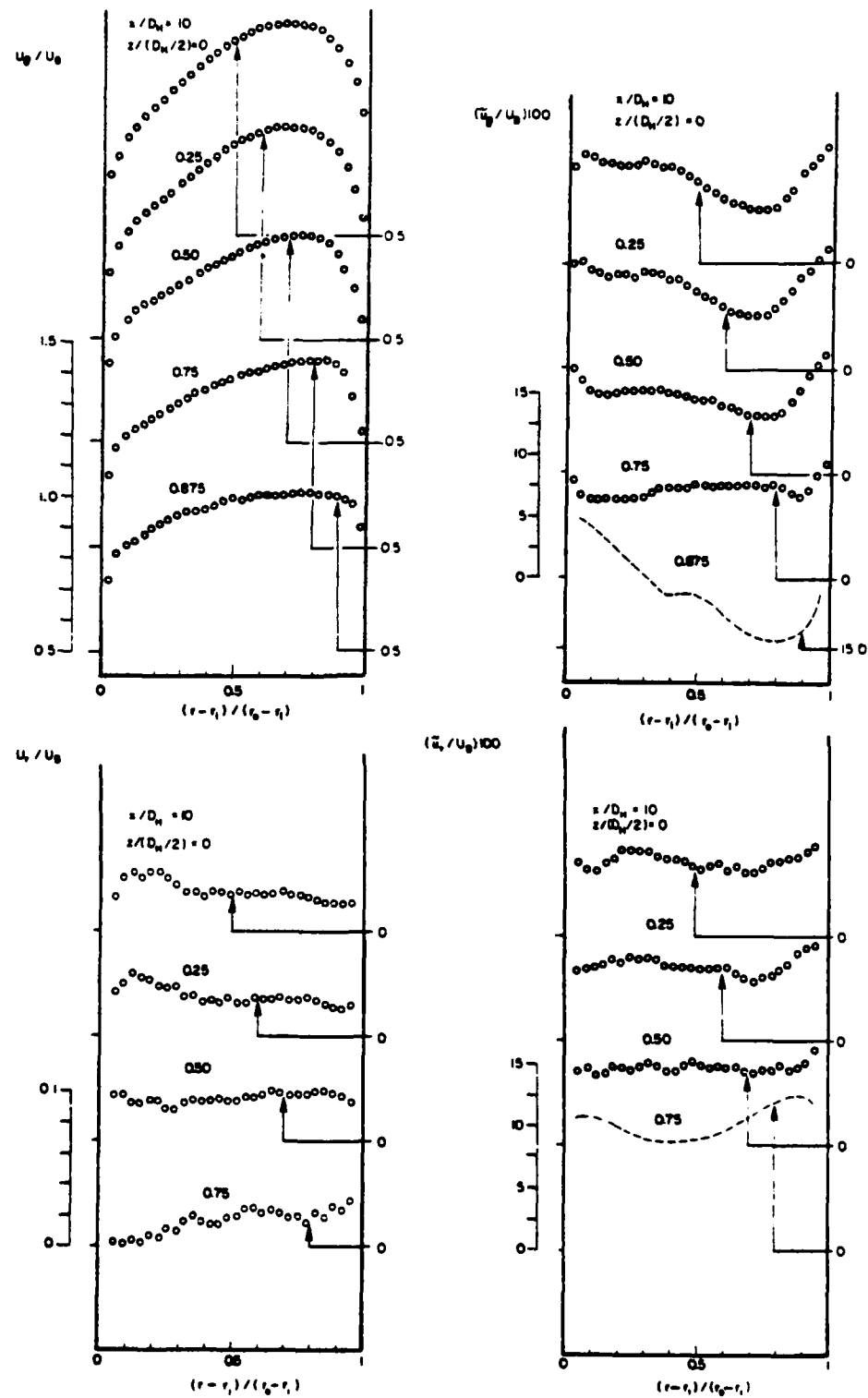


Figure 6.12 Turbulent flow measurements of mean velocity and normal stress in the downstream tangent at $X_H = 10$; dashed lines at 0.75 and 0.875 are best fits to measurements.

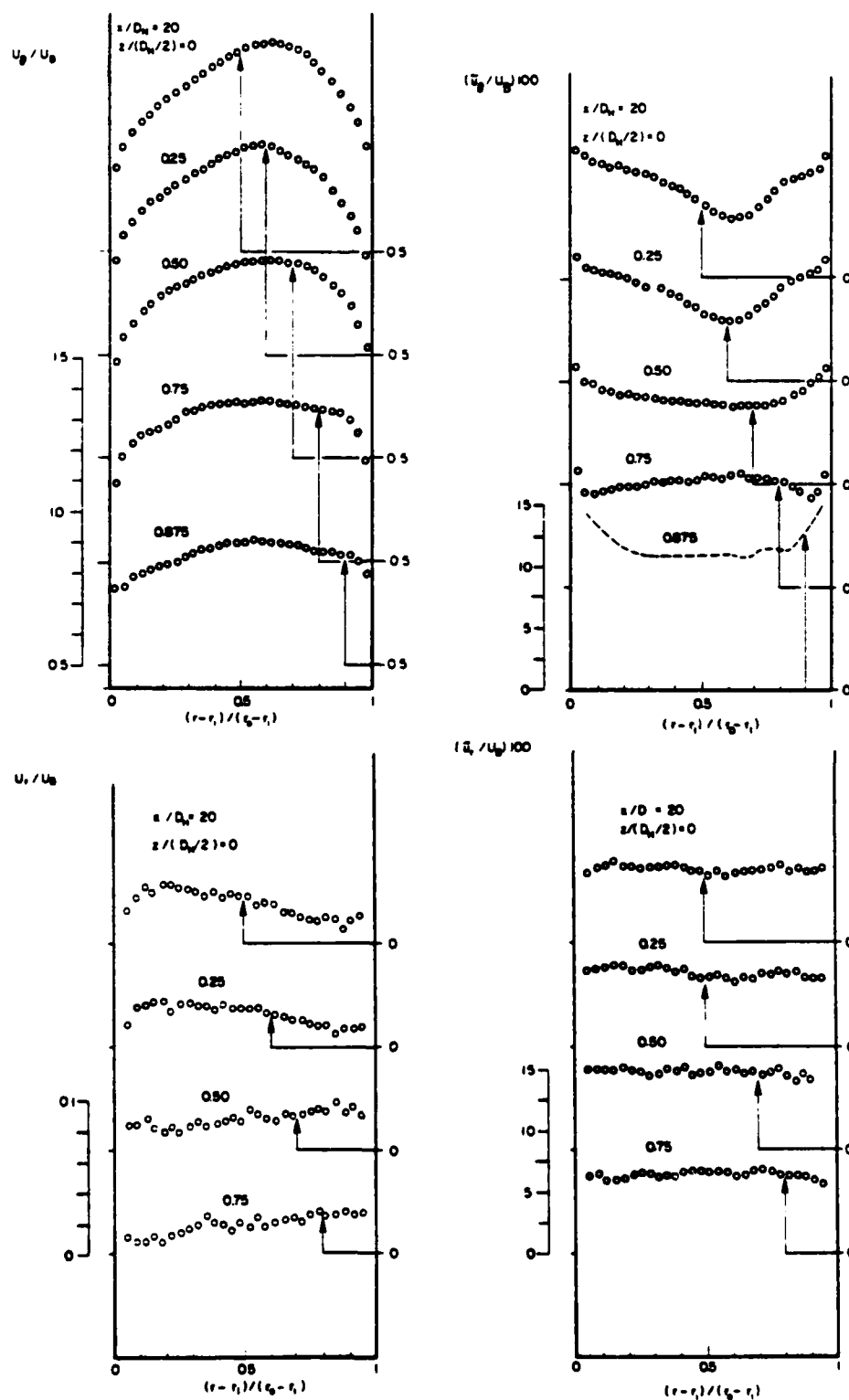


Figure 6.13 Turbulent flow measurements of mean velocity and normal stress in the downstream tangent at $x_H = 20$; dashed line at 0.875 is best fit to measurements.

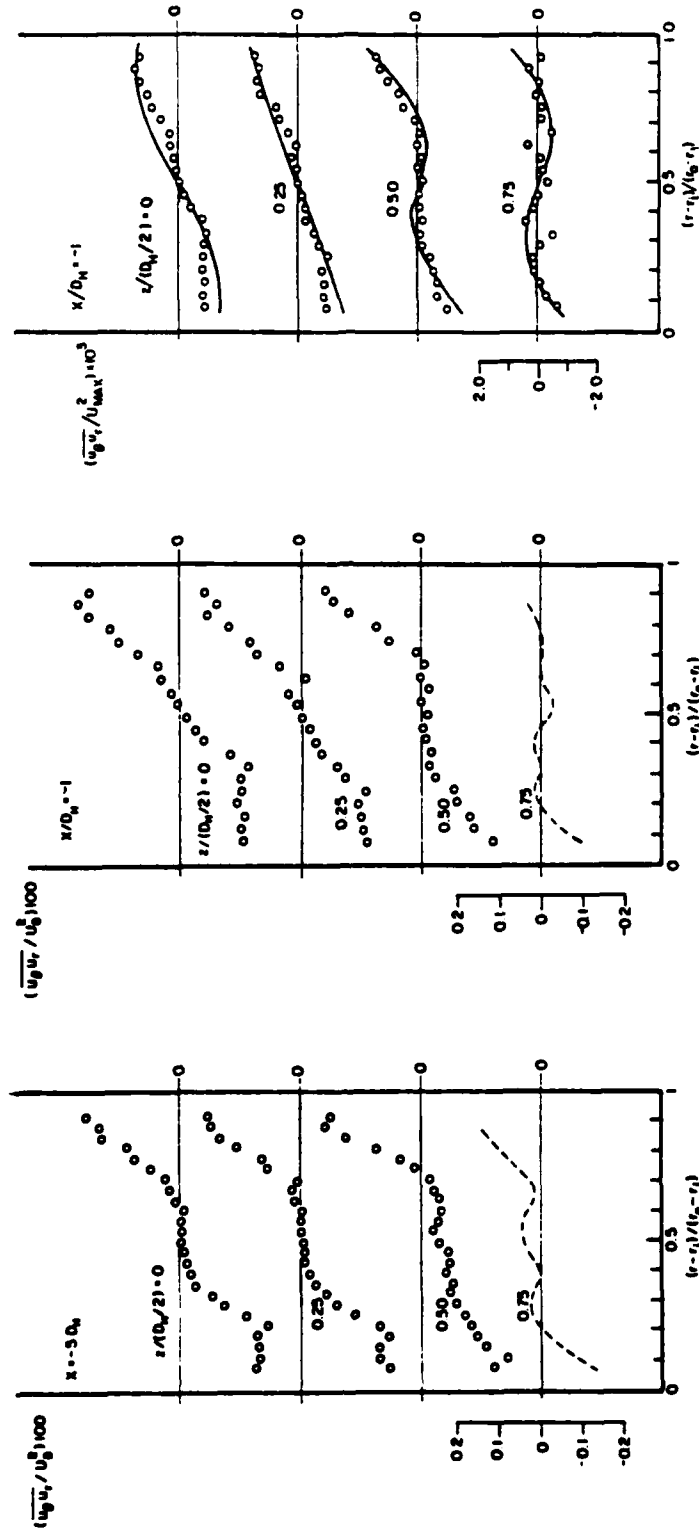


Figure 6.14 Turbulent flow measurements of shear stress at $X_H = -5$ and -1 ; (o) data from this work; (—) data from Melling and White; dashed lines at 0.75 are best fit to data.

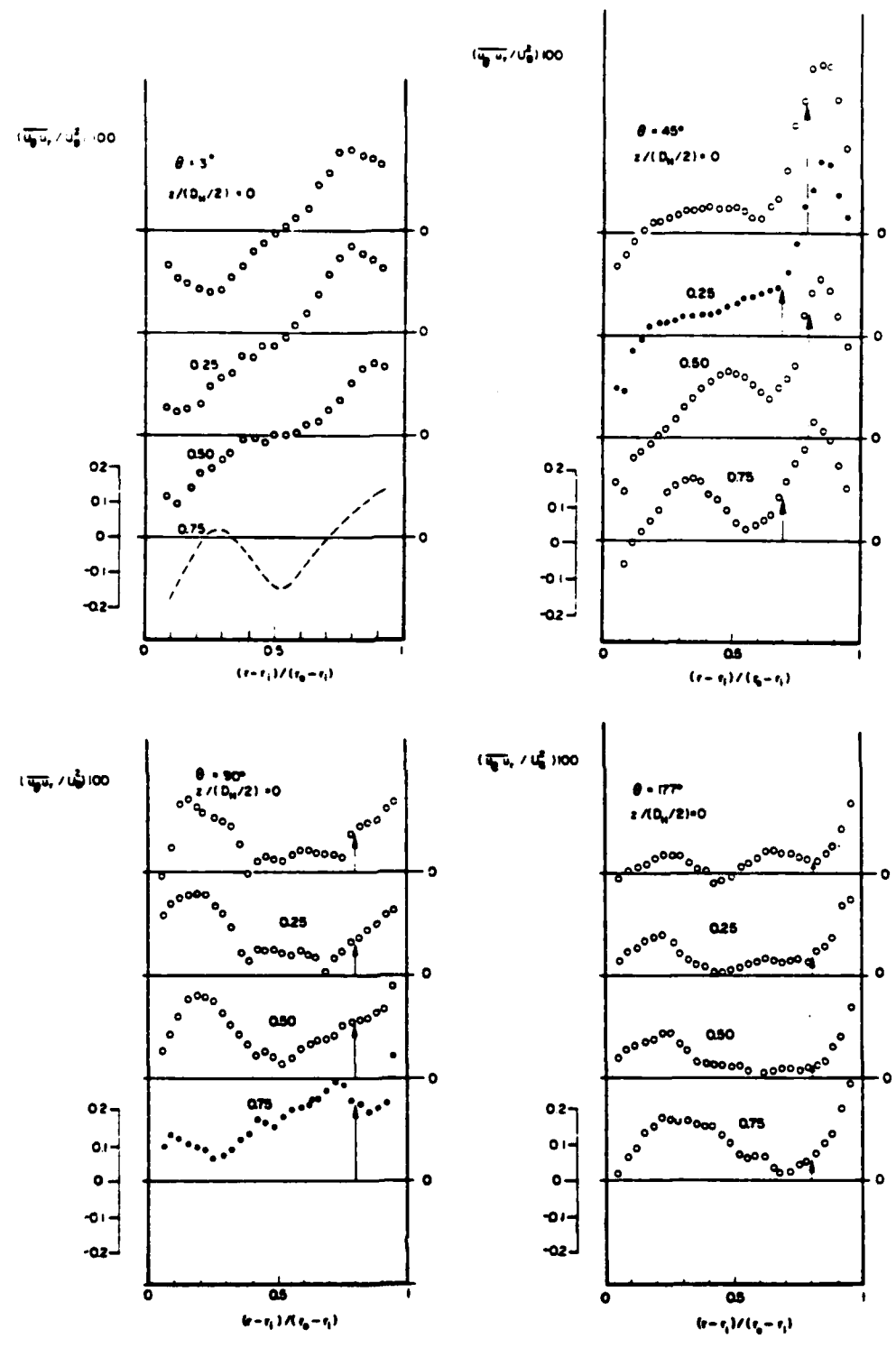


Figure 6.15 Turbulent flow measurements of shear stress at four longitudinal stations in the bend; dashed line at 0.75 is best fit to measurements.

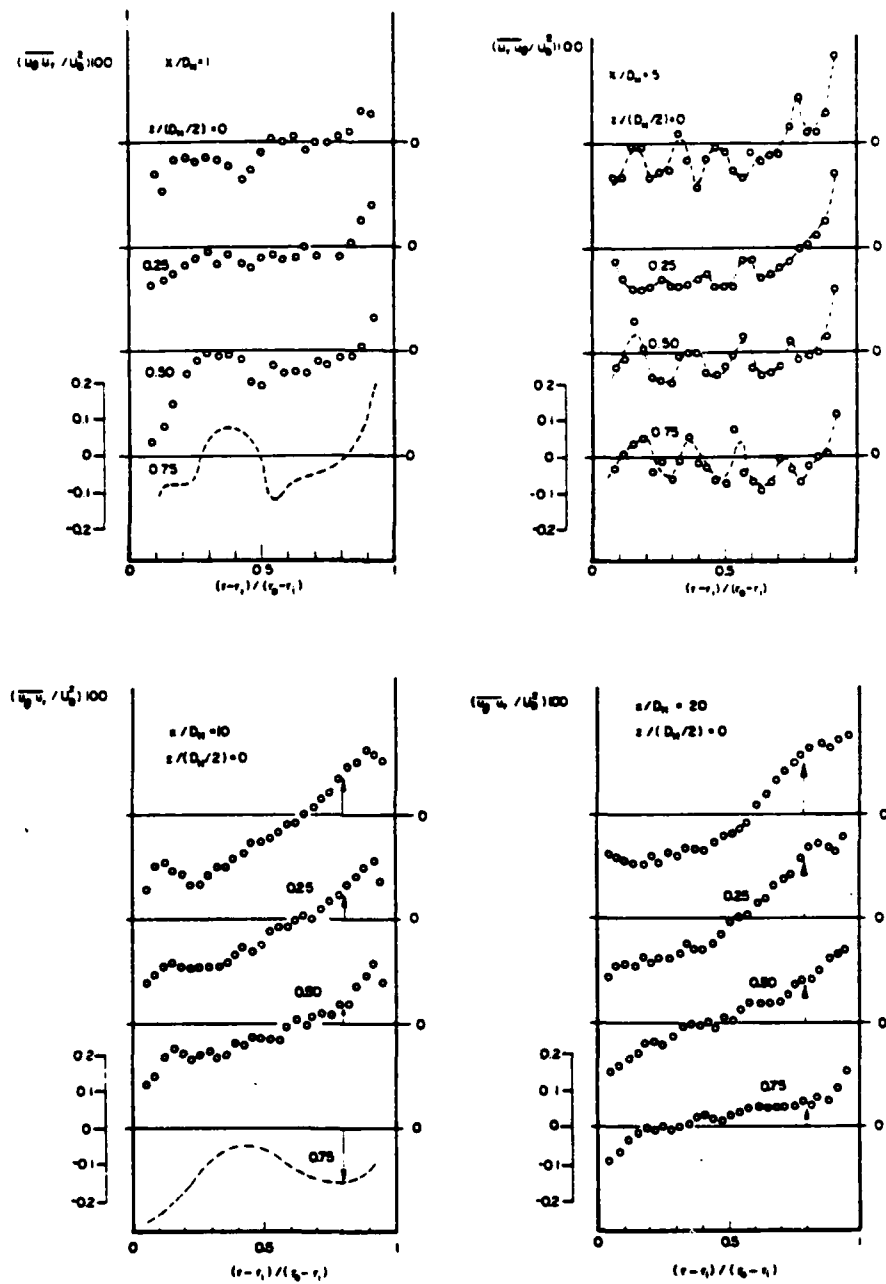


Figure 6.16 Turbulent flow measurements of shear stress at four longitudinal stations in the downstream tangent; dashed lines are best fits to measurements.

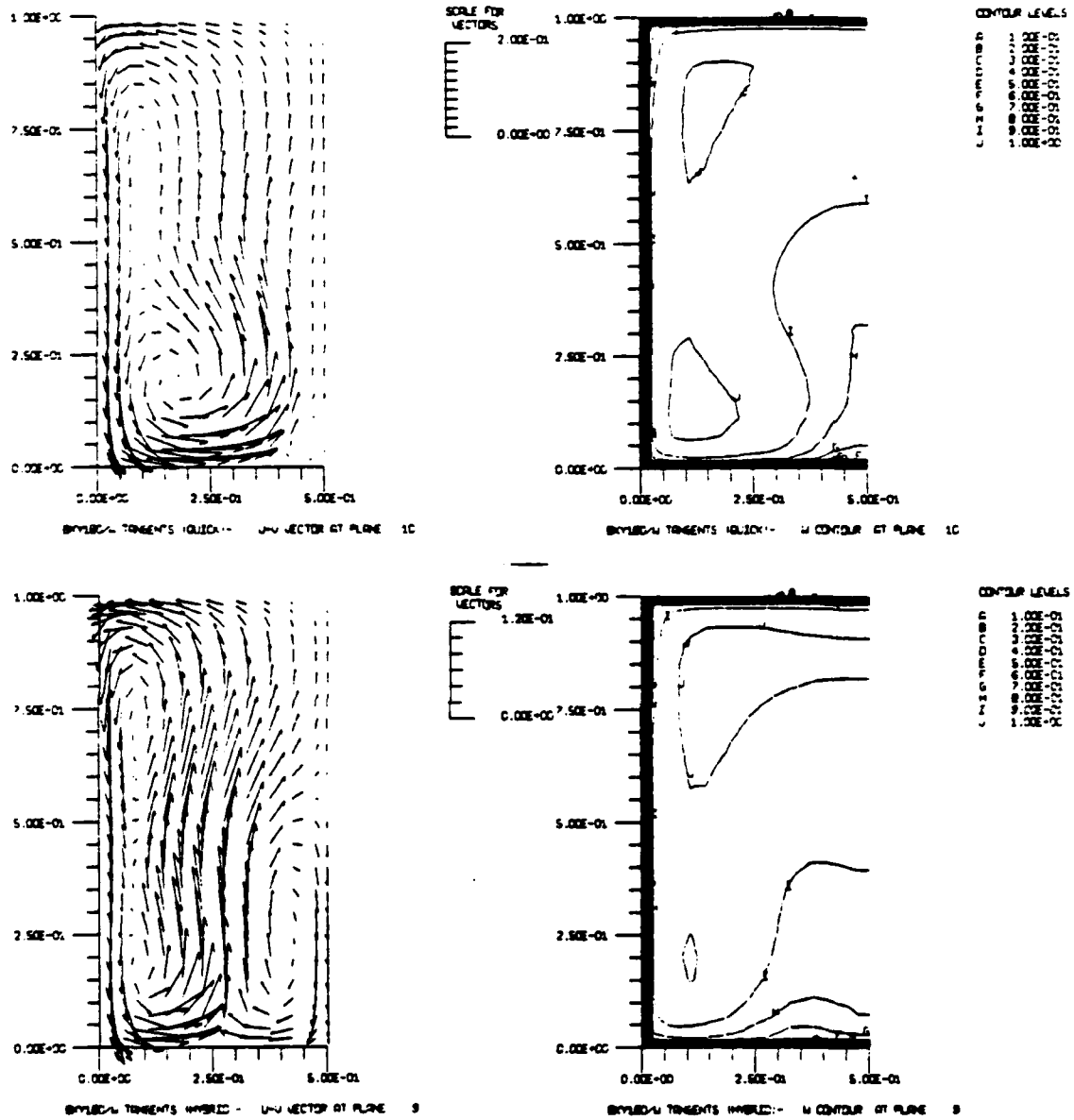


Figure 6.17 Turbulent flow predictions (k- ϵ model) of cross-stream and streamwise velocities at $\theta = 177^\circ$: velocity components are normalized by U_B ; outer radius (concave) wall is shown at the top of each plot.

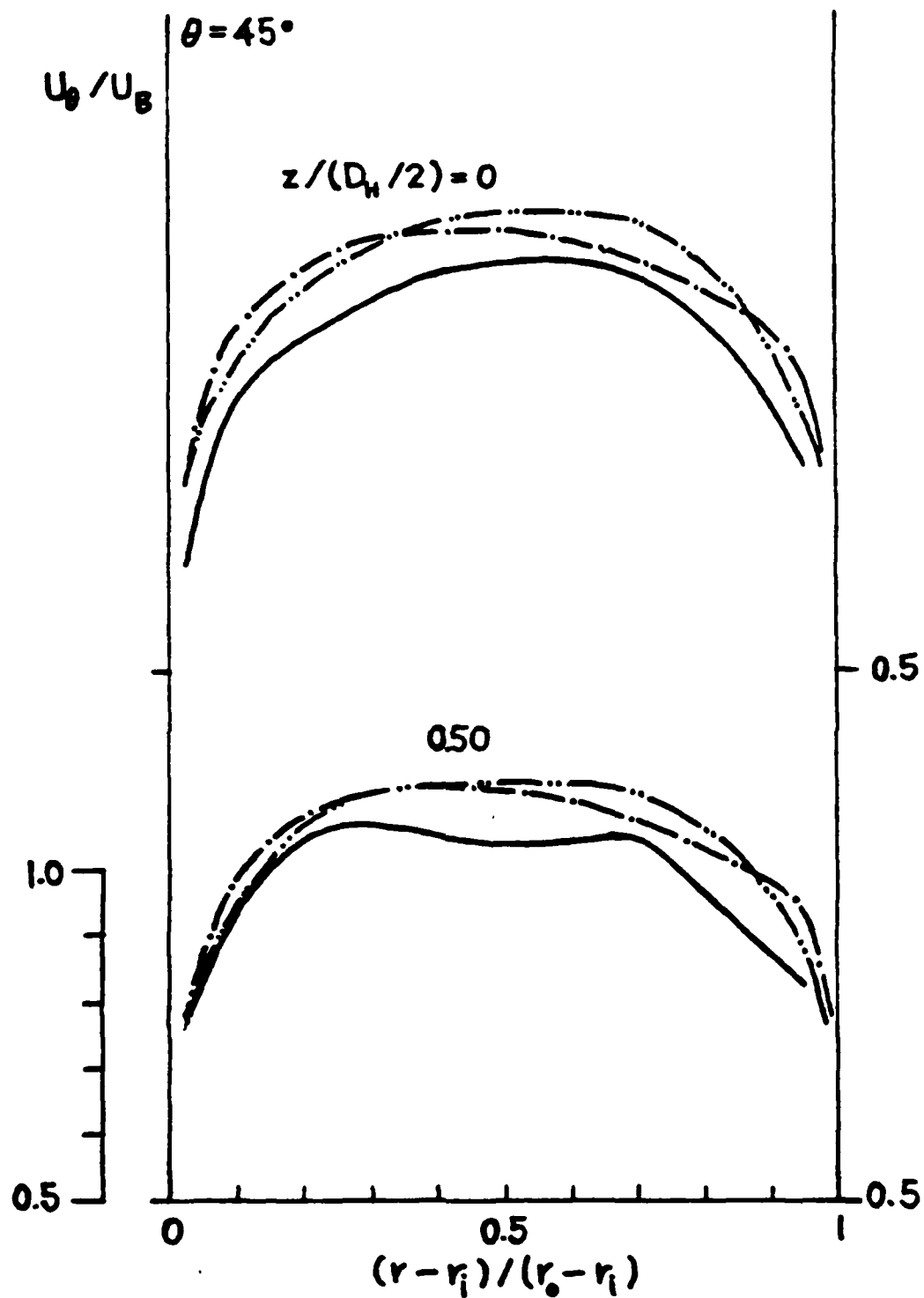


Figure 6.18 ASM calculations of U_θ/U_B at $\theta = 45^\circ$: (—) best fits to measurements, (---) ASM, (-.-.-) k- ϵ model.

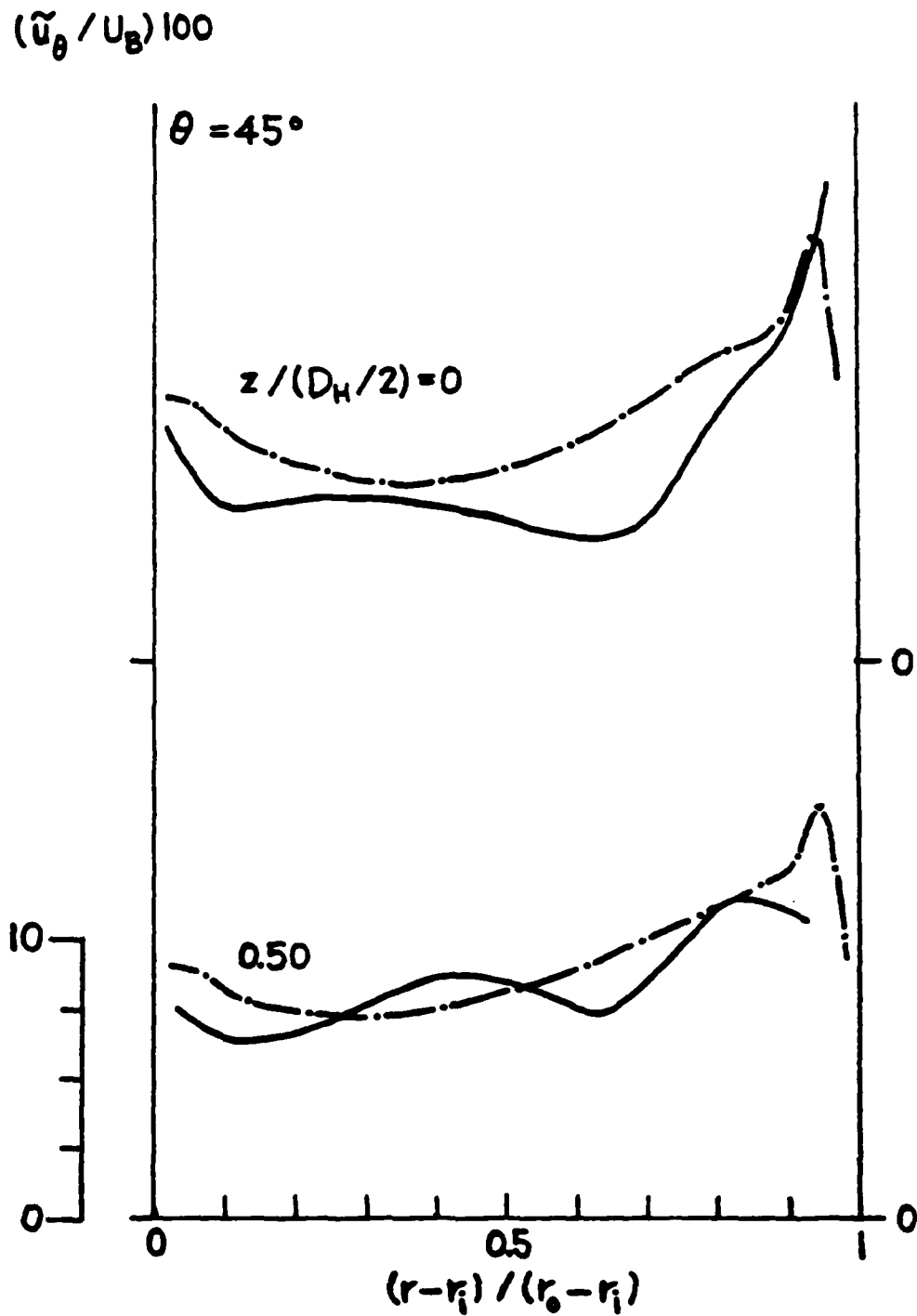


Figure 6.19 ASM calculations of $(\tilde{u}_\theta / U_B) \times 100$ at $\theta = 45^\circ$: (—) best fits to measurements, (-.-) ASM.

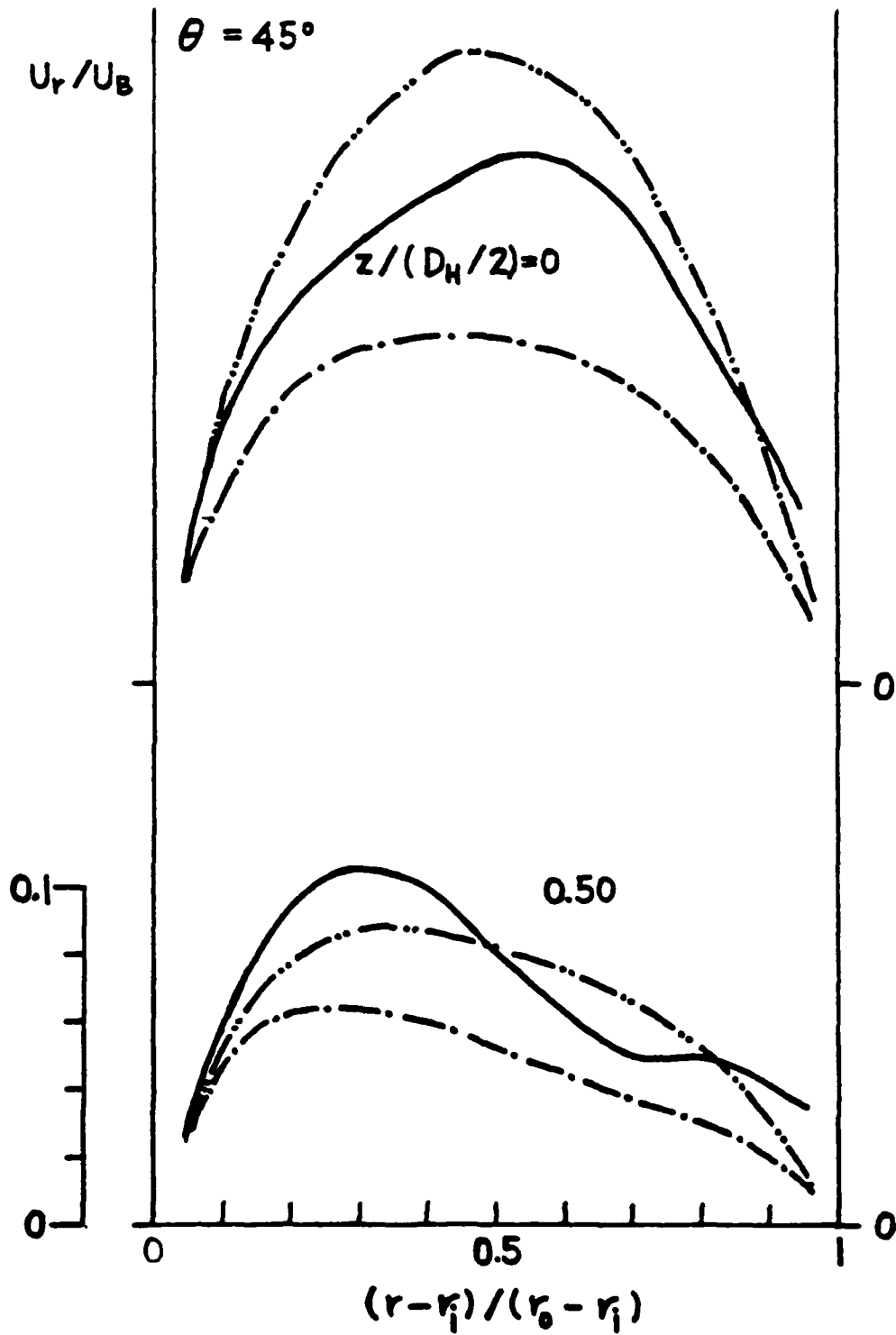


Figure 6.20 ASM calculations of (U_r/U_B) at $\theta = 45^\circ$: (—) best fits to measurements, (---) ASM, (-·-·-) k-ε model.

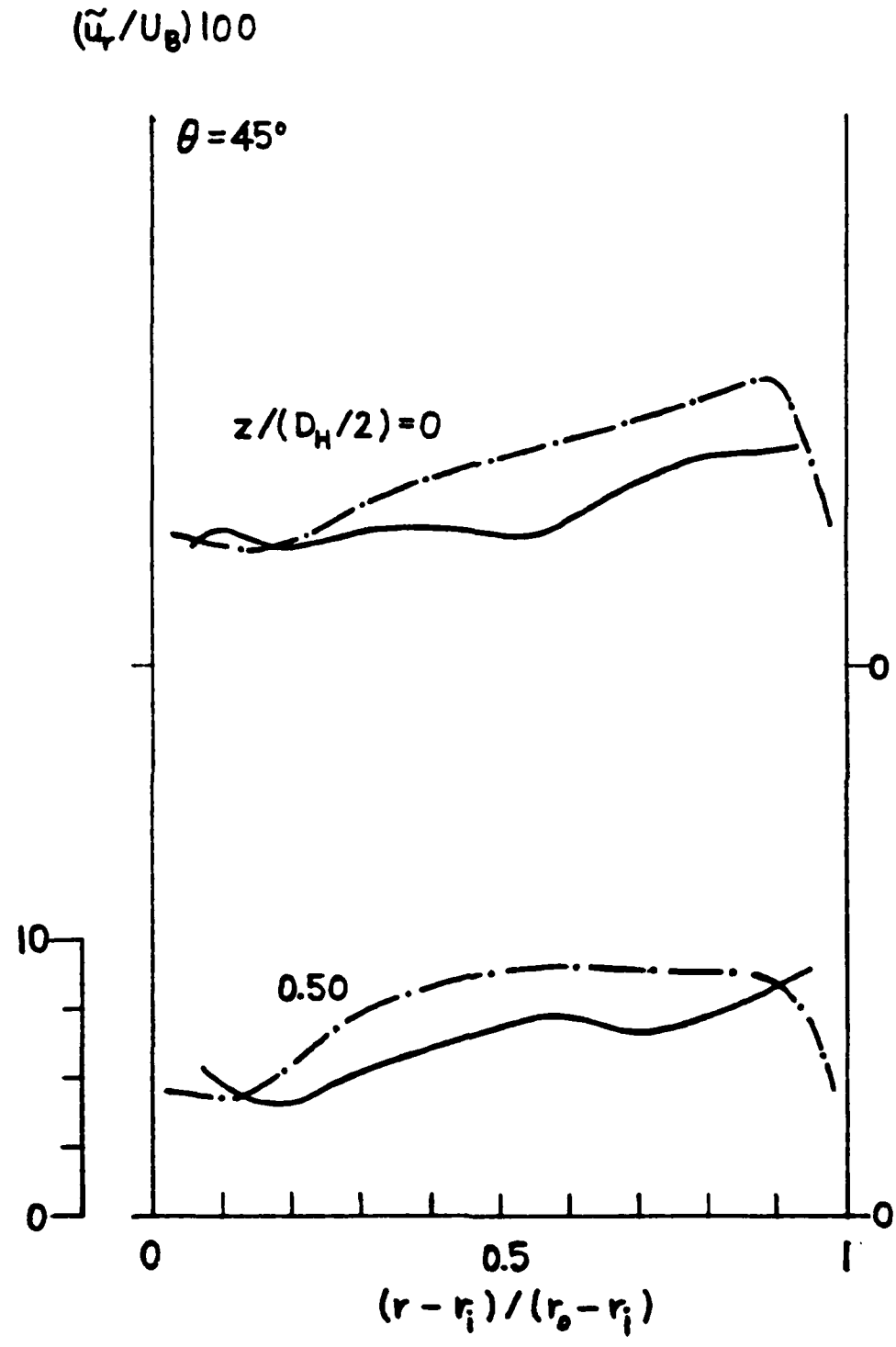


Figure 6.21 ASM calculations of $(\bar{u}_r/U_B) \times 100$ at $\theta = 45^\circ$: (—) best fits to measurements, (-.-) ASM.

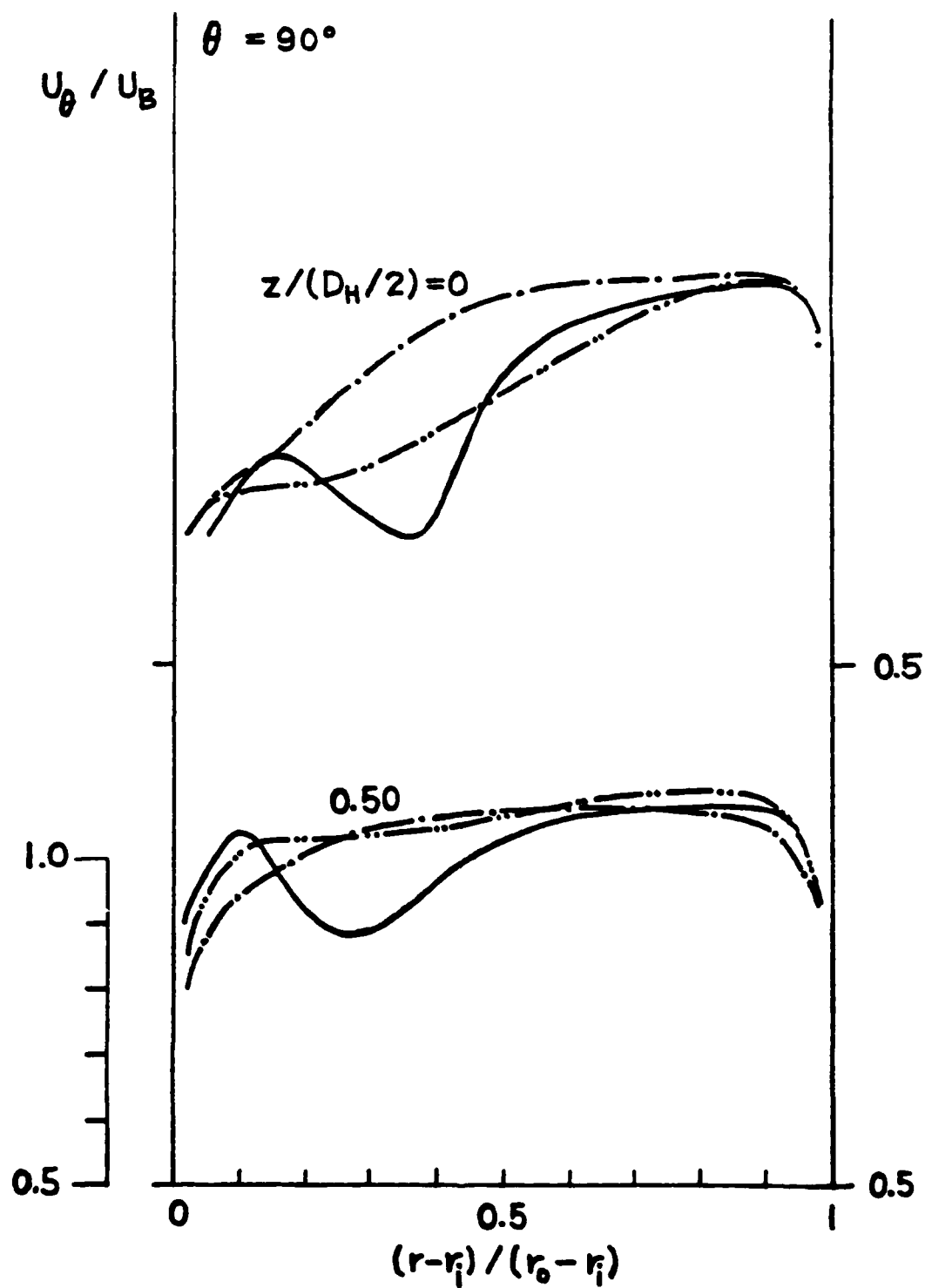


Figure 6.22 ASM calculations of U_θ/U_B at $\theta = 90^\circ$: (—) best fits to measurements, (---) ASM, (-.-.-) k- ϵ model.

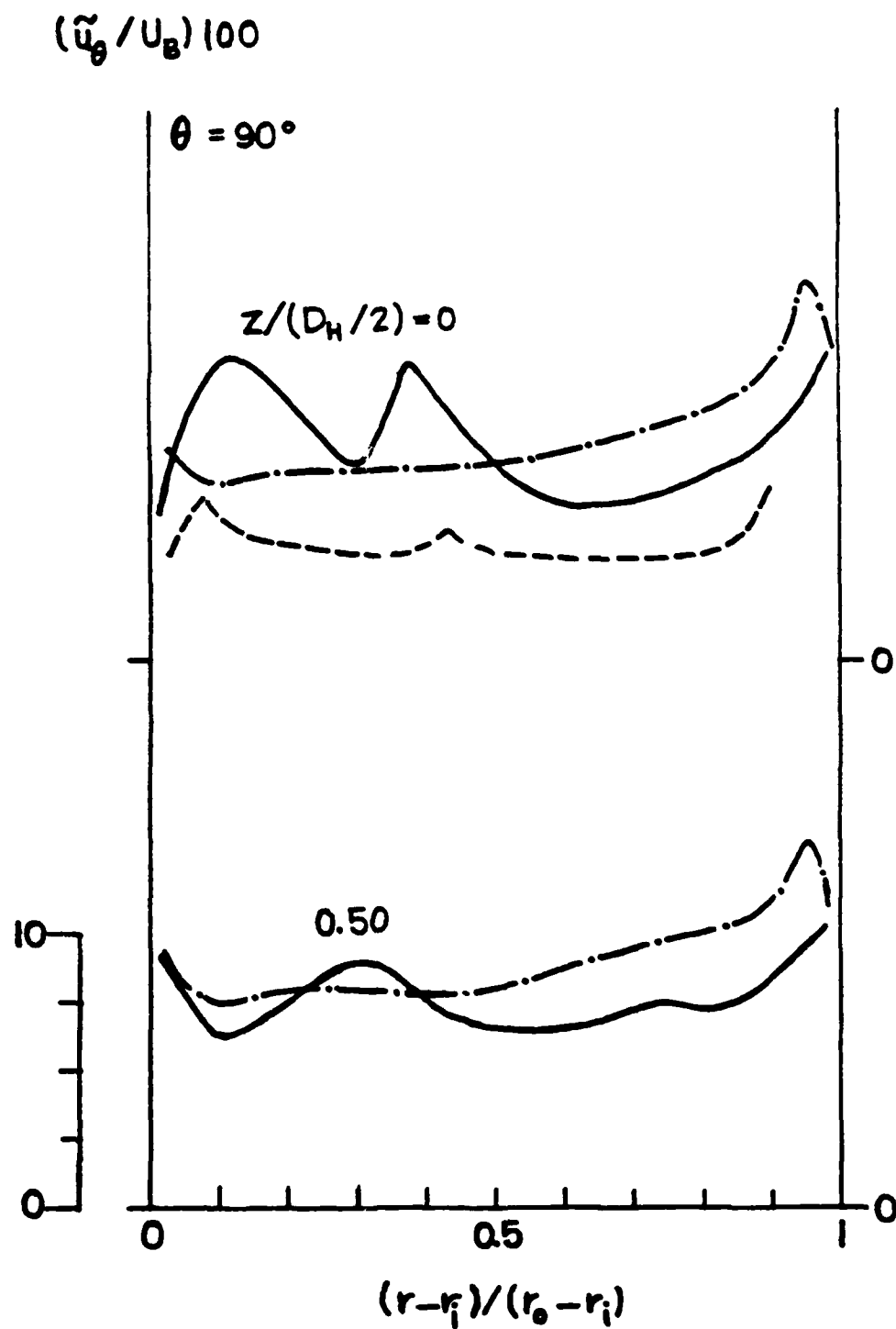


Figure 6.23 ASM calculations of $(\tilde{u}_\theta / U_B) \times 100$ at $\theta = 90^\circ$: (—) best fits to measurements, (-.-) ASM. (---) "experimental" test #1.

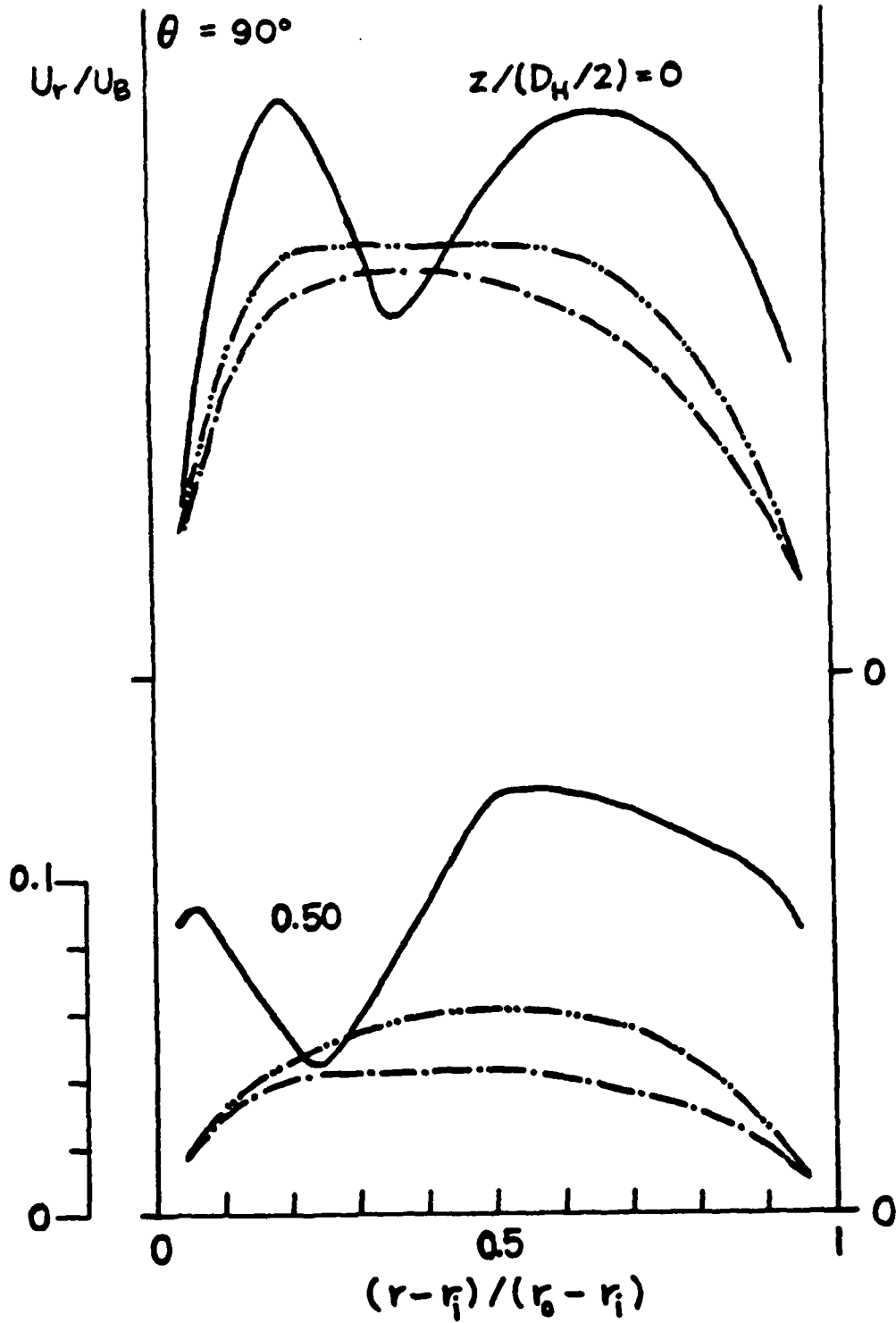


Figure 6.24 ASM calculations of (U_r/U_B) at $\theta = 90^\circ$: (—) best fits to measurements, (---) ASM, (-.-.-) k- ϵ model.

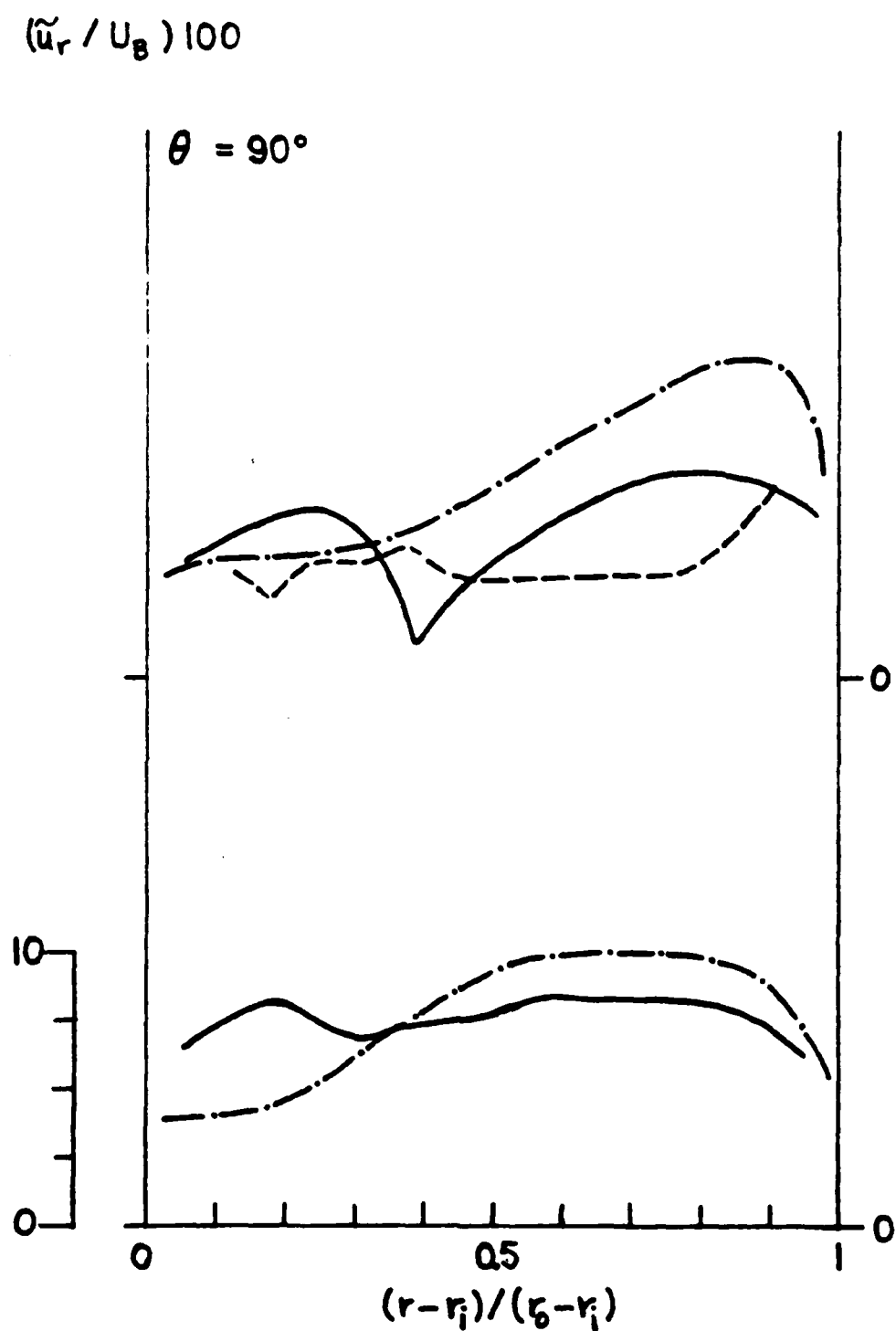


Figure 6.25 ASM calculations of $(\bar{u}_r / U_B) \times 100$ at $\theta = 90^\circ$: (—) best fits to measurements, (-.-) ASM, (- - -) "experimental" test #1.

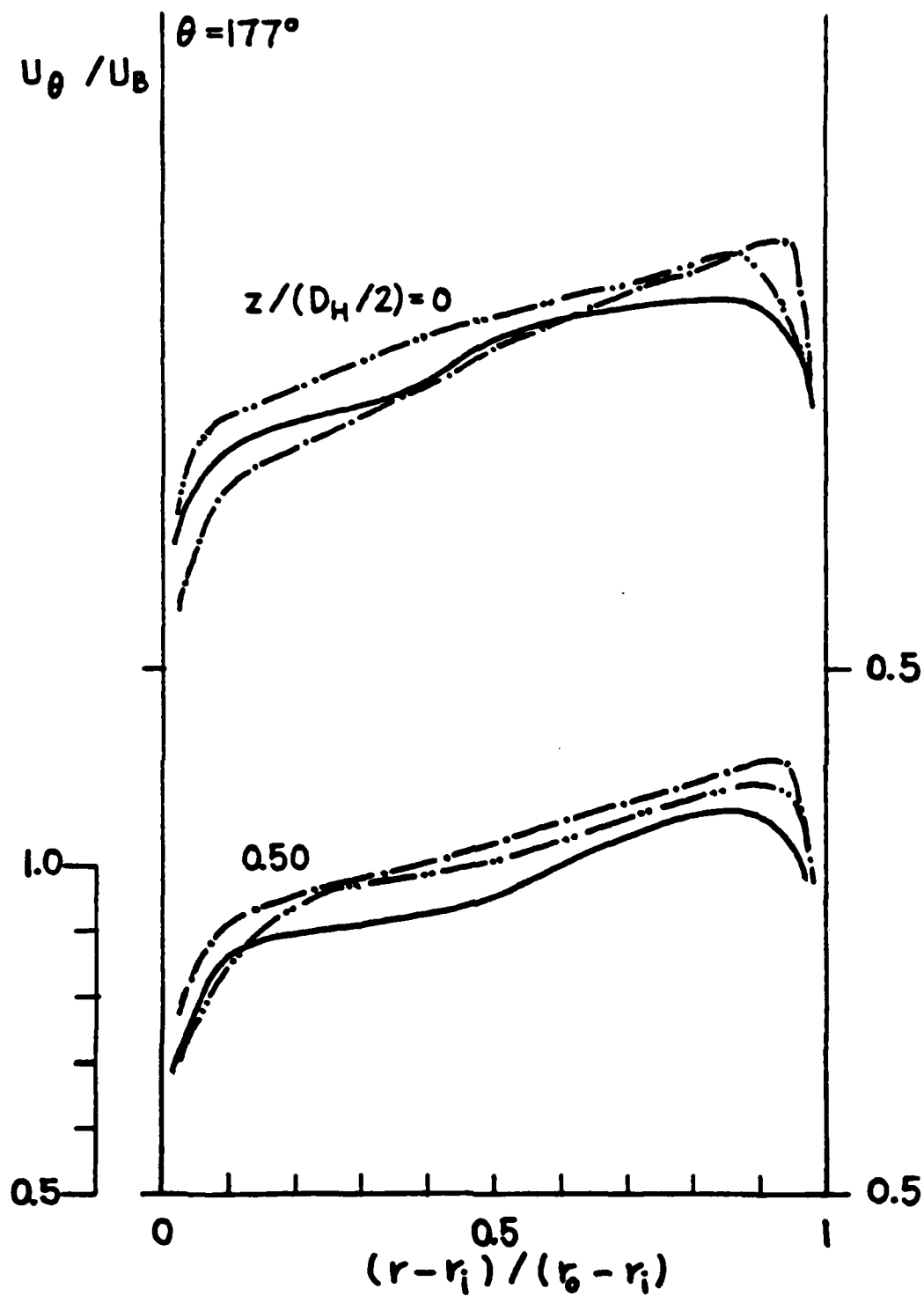


Figure 6.26 ASM calculations of U_θ / U_B at $\theta = 177^\circ$: (—) best fits to measurements, (-·-) ASM, (- - -) k- ϵ model.

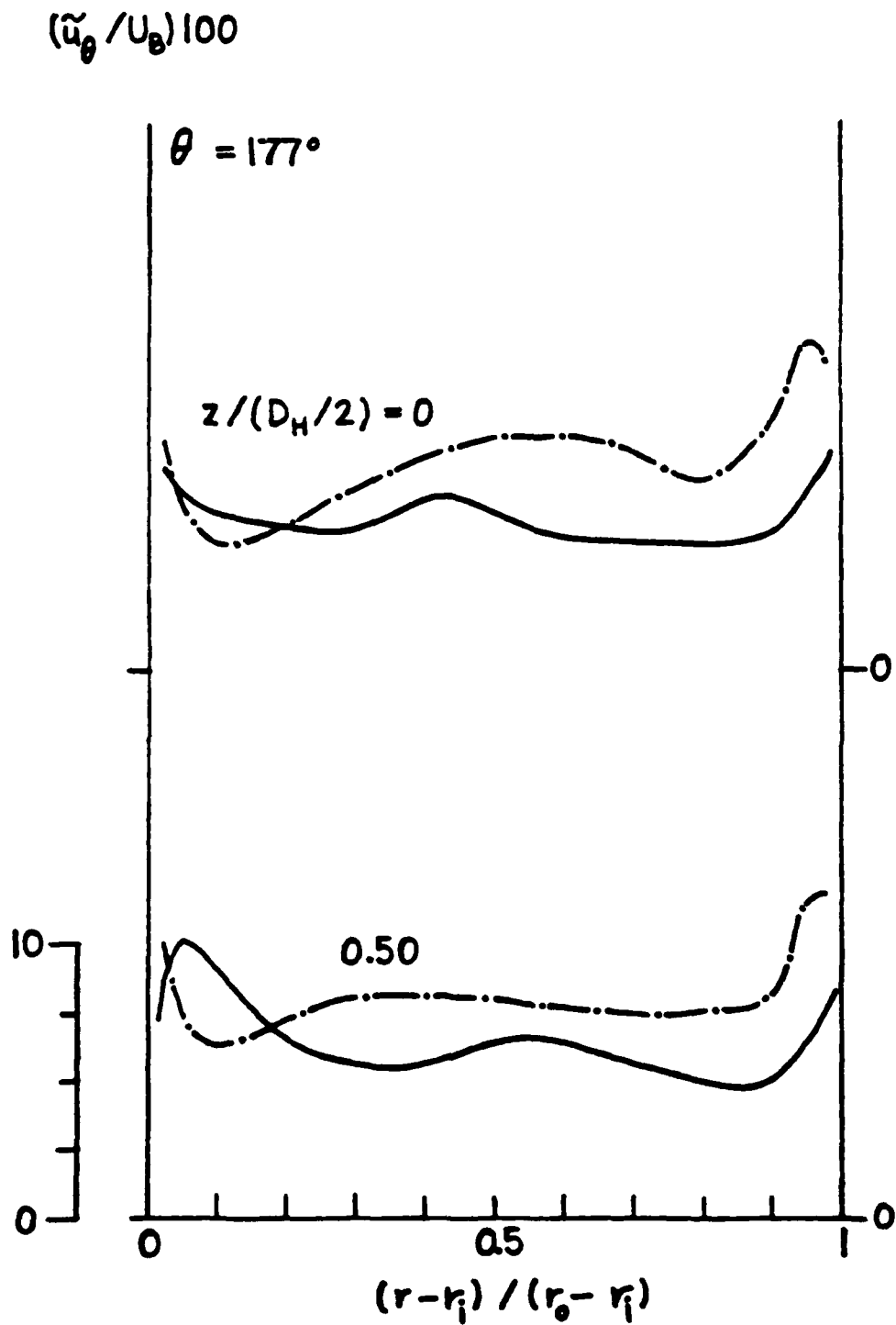


Figure 6.27 ASM calculations of $(\bar{u}_\theta / U_B) \times 100$ at $\theta = 177^\circ$: (—) best fits to measurements, (-.-) ASM.

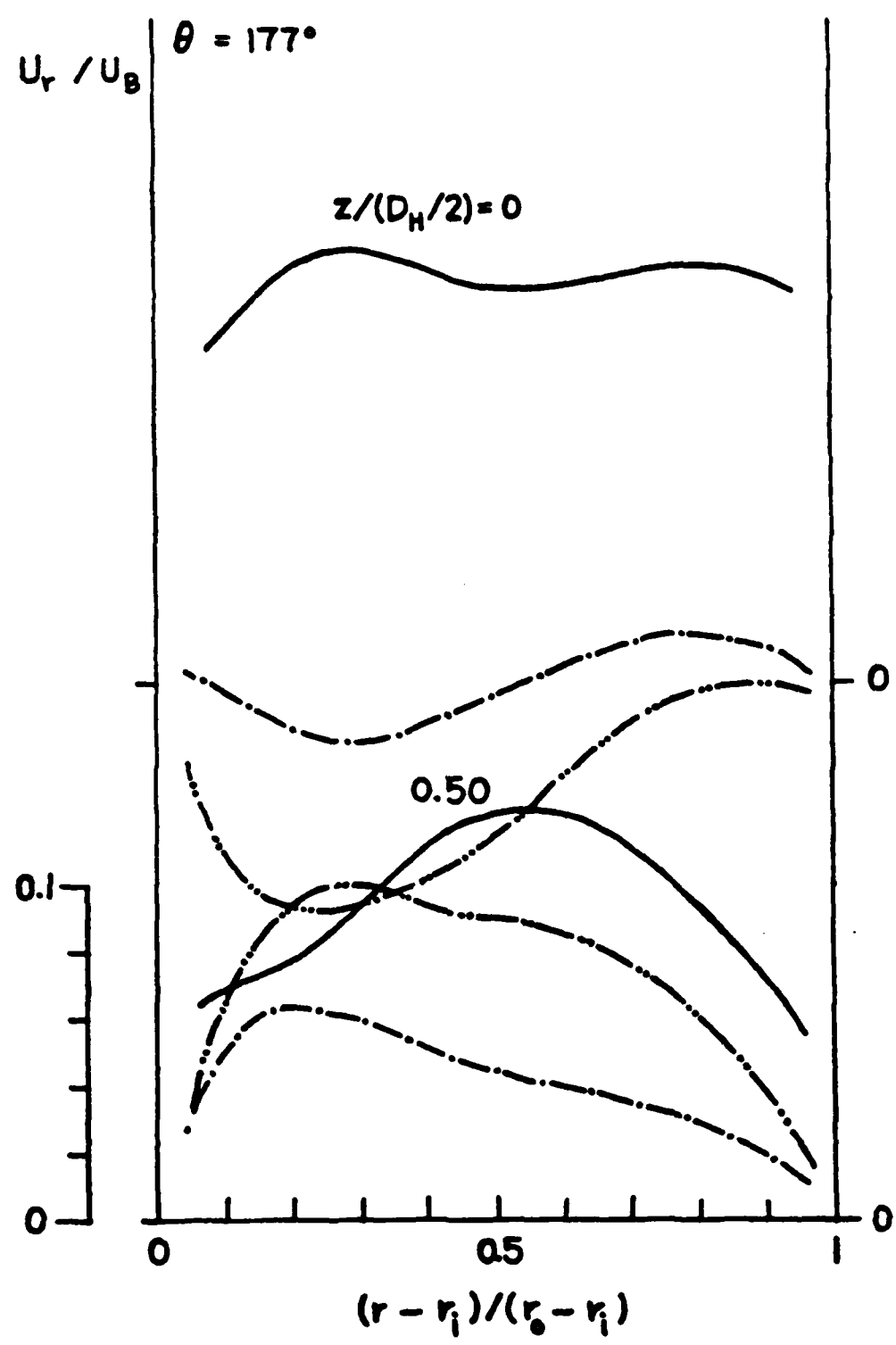


Figure 6.28 ASM calculations of (U_r / U_B) at $\theta = 177^\circ$: (—) best fits to measurements, (---) ASM, (-.-) k- ϵ model.

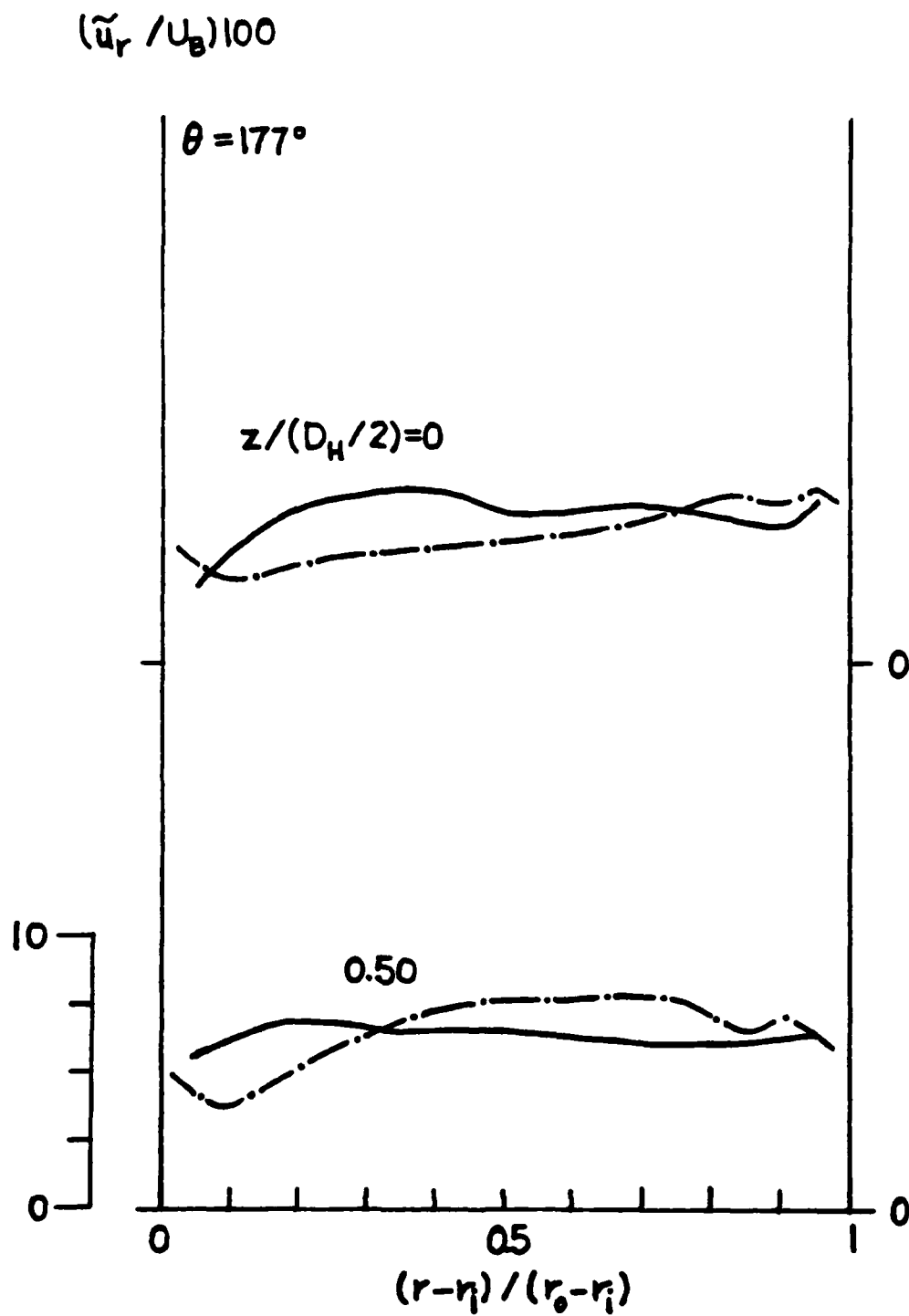


Figure 6.29 ASM calculations of $(\tilde{u}_r / U_B) \times 100$ at $\theta = 177^\circ$: (—) best fits to measurements, (---) ASM.

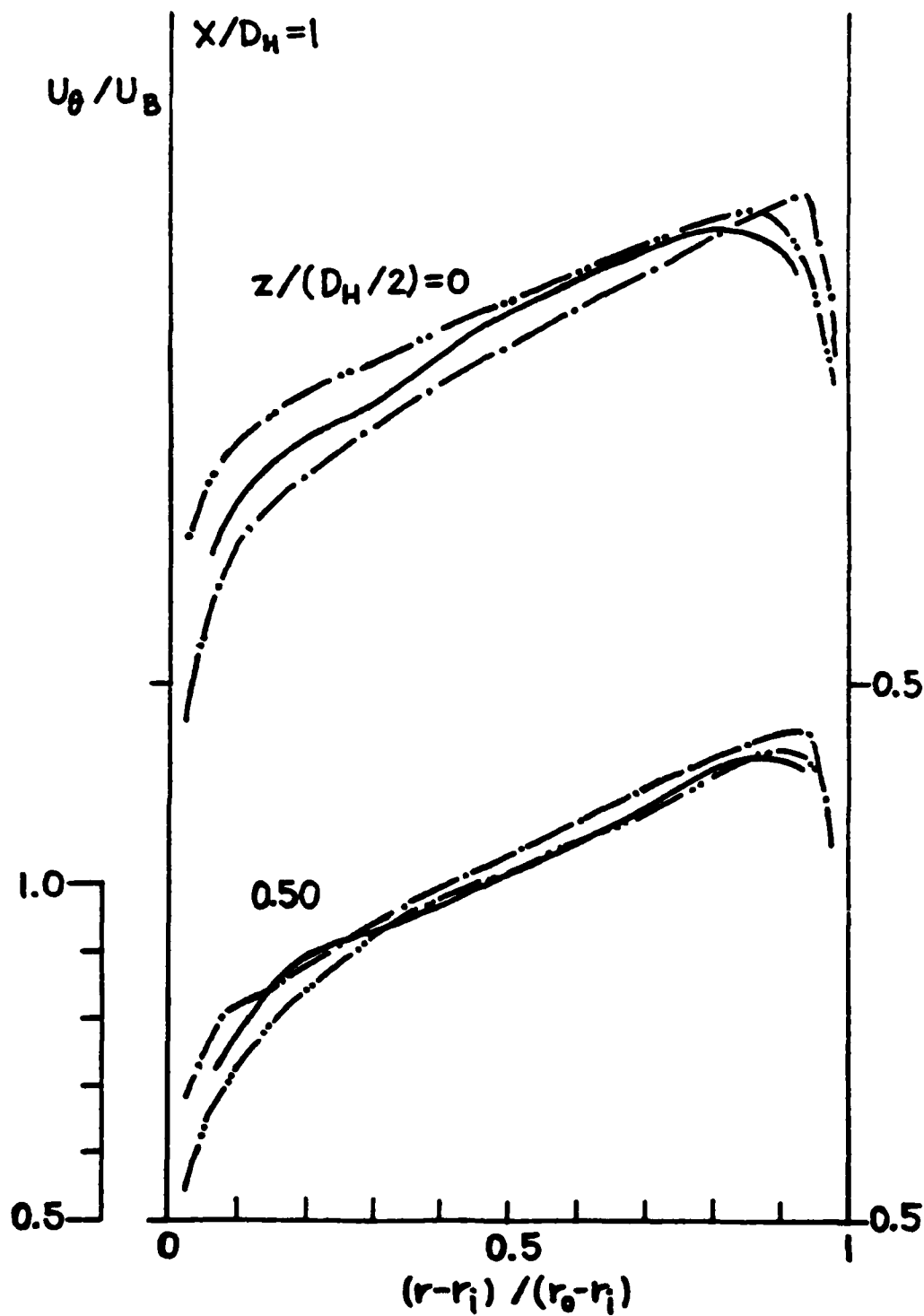


Figure 6.30 ASM calculations of U_θ/U_B at $x/D_H = 1$: (—) best fits to measurements, (---) ASM, (-.-) k- ϵ model.

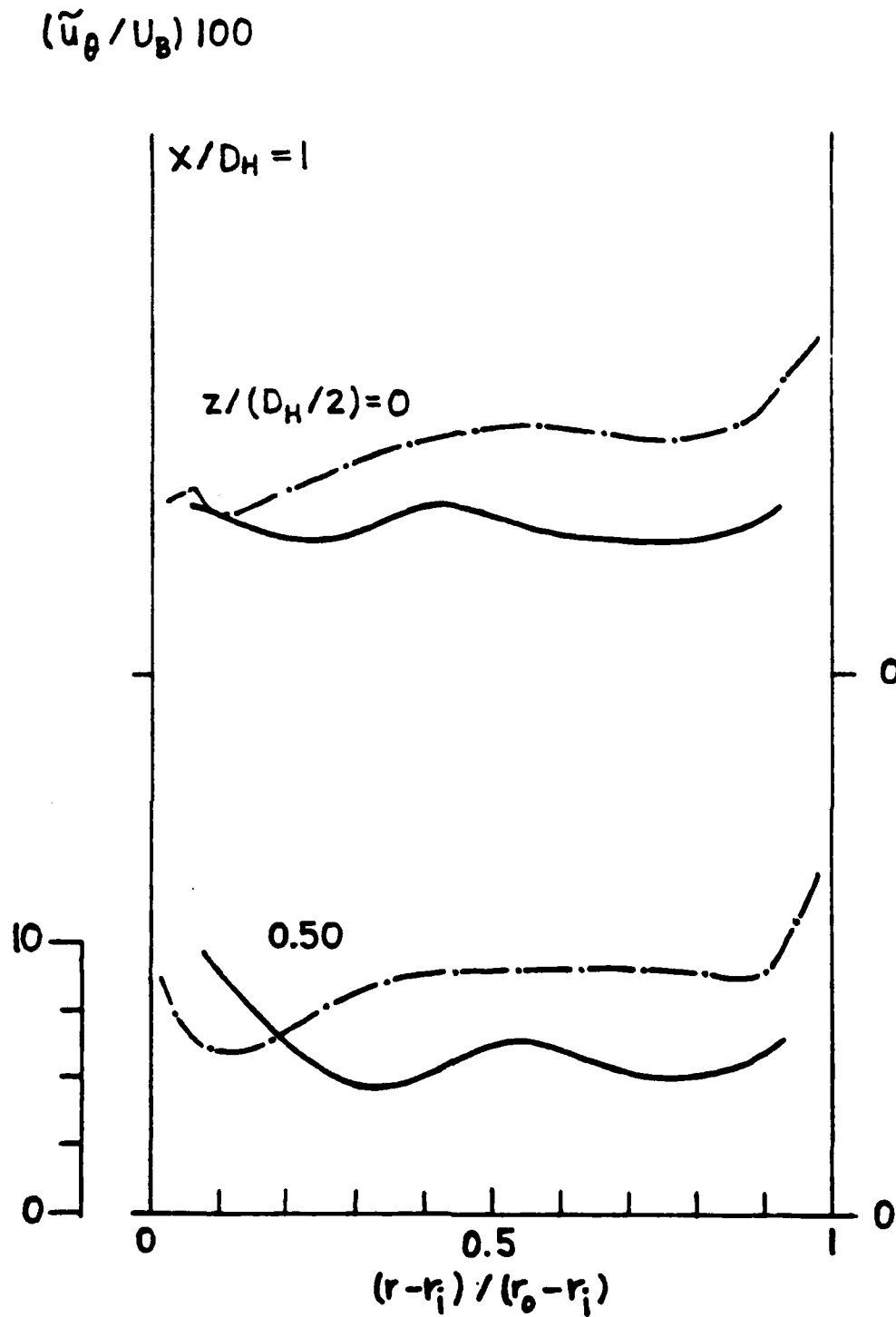


Figure 6.31 ASM calculations of $(\tilde{u}_\theta / U_B) \times 100$ at $x/D_H = 1$: (—) best fits to measurements, (-.-) ASM.

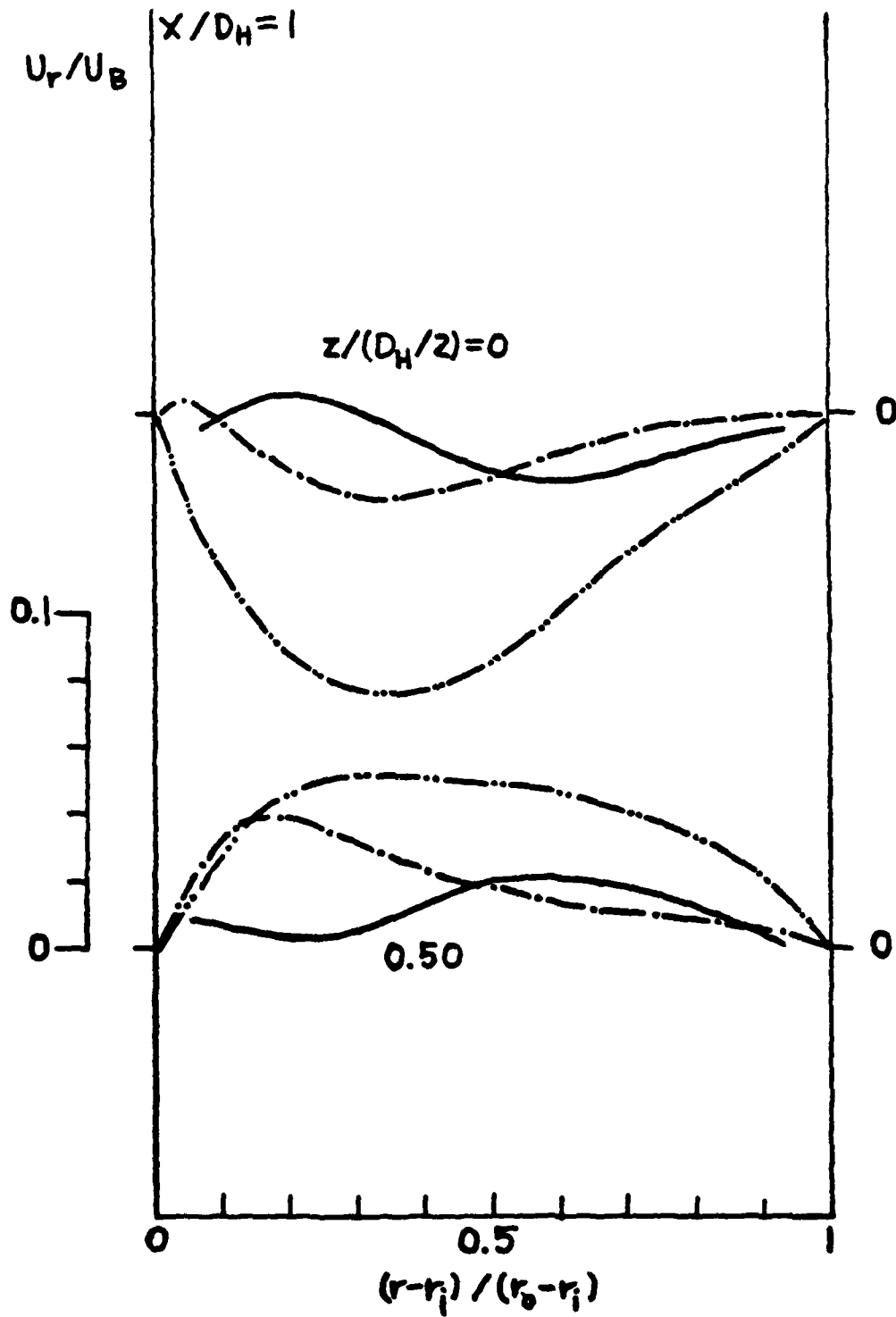


Figure 6.32 ASM calculations of (U_r/U_B) at $x/D_H = 1$: (—) best fits to measurements, (---) ASM, (-·-·) k- ϵ model.

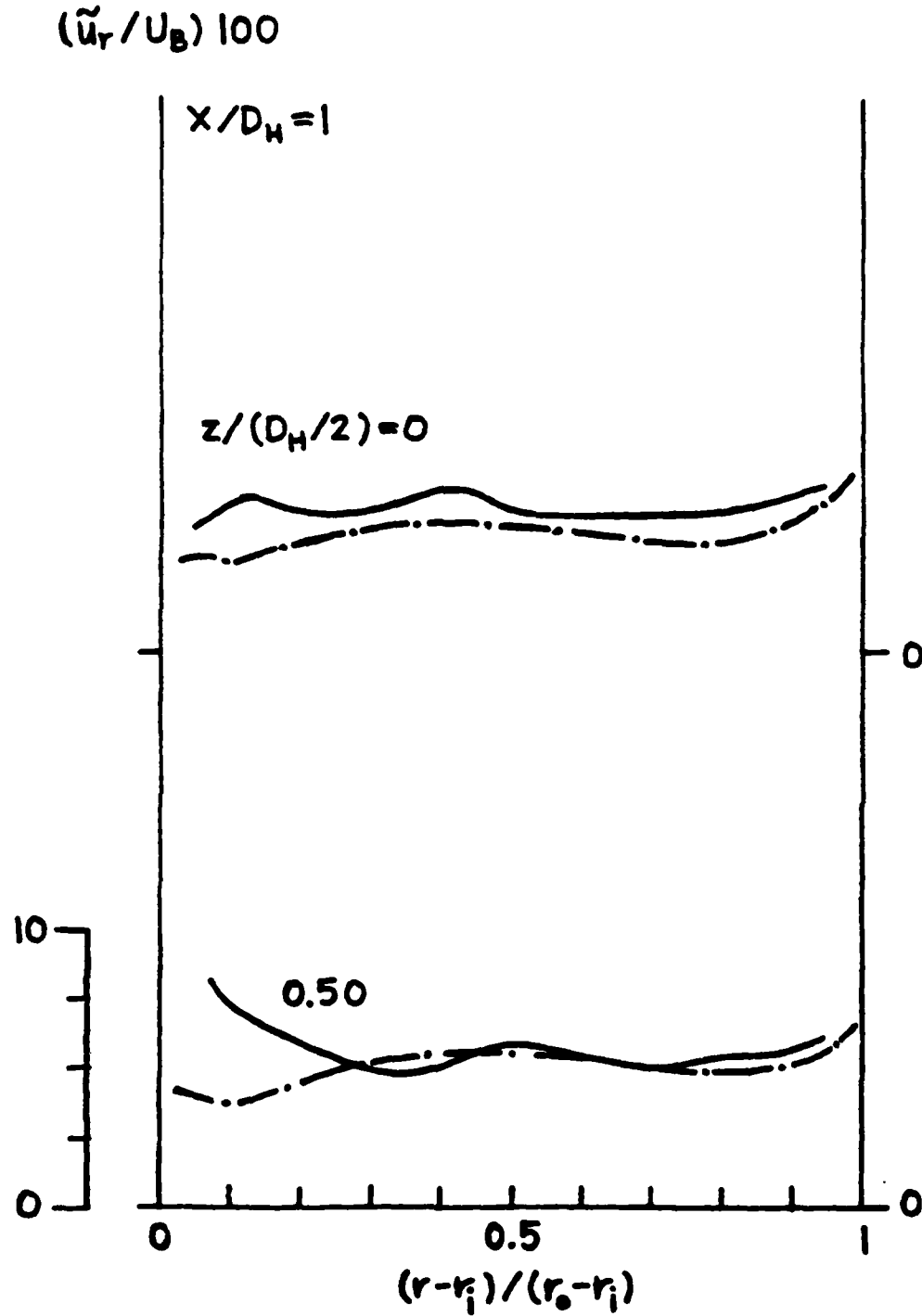


Figure 6.33 ASM calculations of $(\tilde{u}_r/U_B) \times 100$ at $x/D_H = 1$: (—) best fits to measurements, (-.-) ASM.

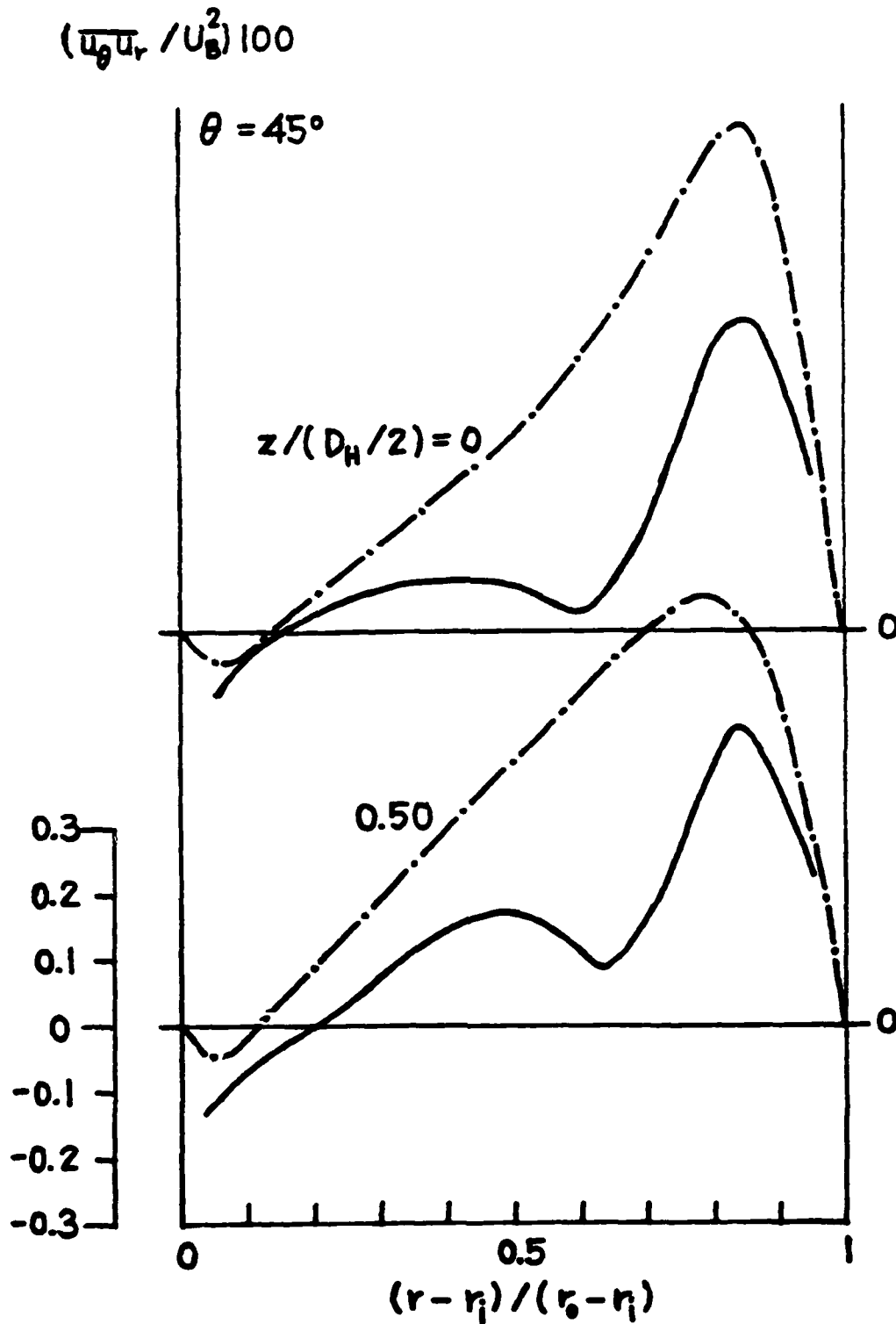


Figure 6.34 ASM calculations of $(\overline{u_\theta u_r} / U_B^2) \times 100$ at $\theta = 45^\circ$: (—) best fits to measurements, (-.-) ASM.

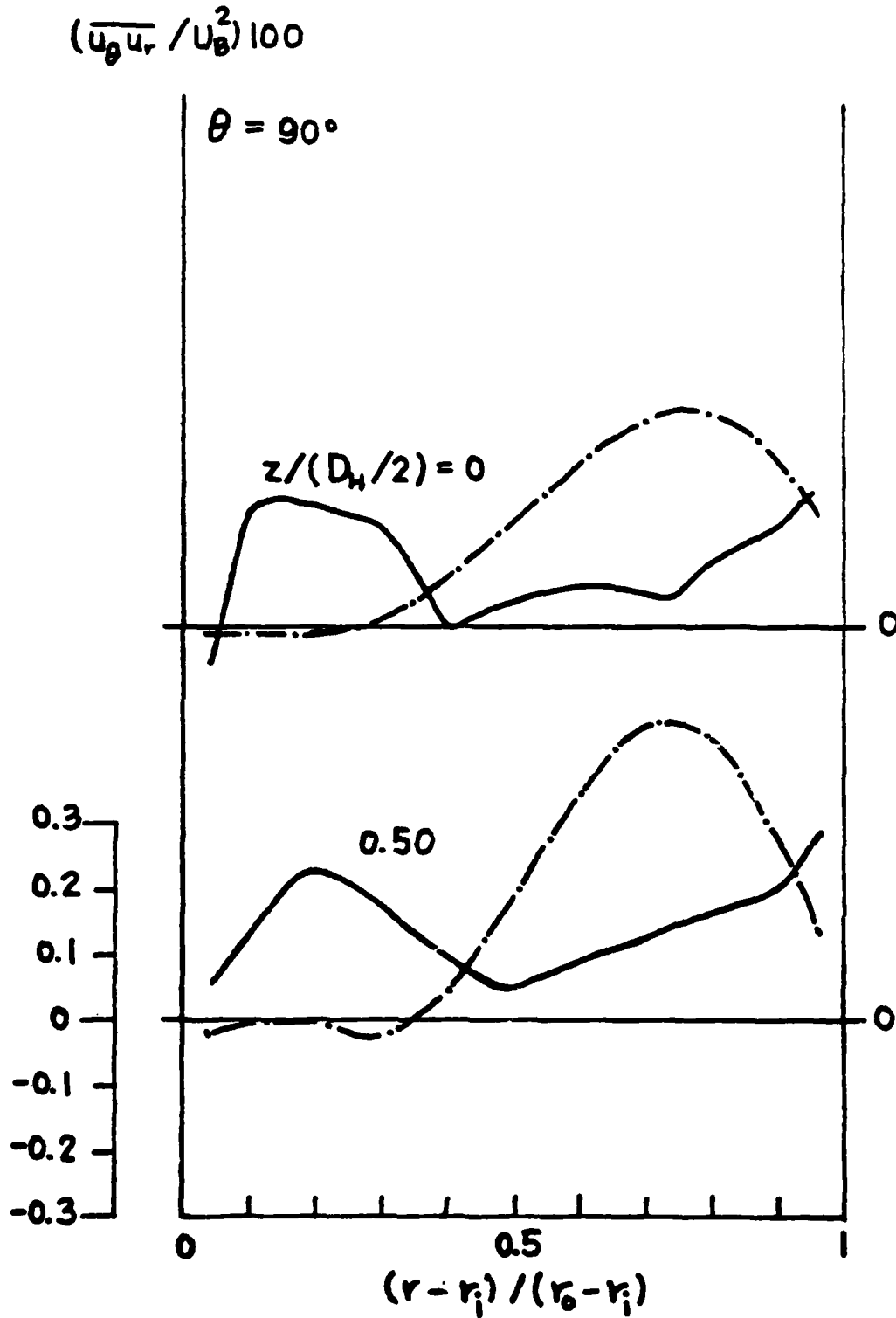


Figure 6.35 ASM calculations of $(\overline{u_\theta u_r} / U_B^2) \times 100$ at $\theta = 90^\circ$: (—) best fits to measurements, (-.-) ASM.

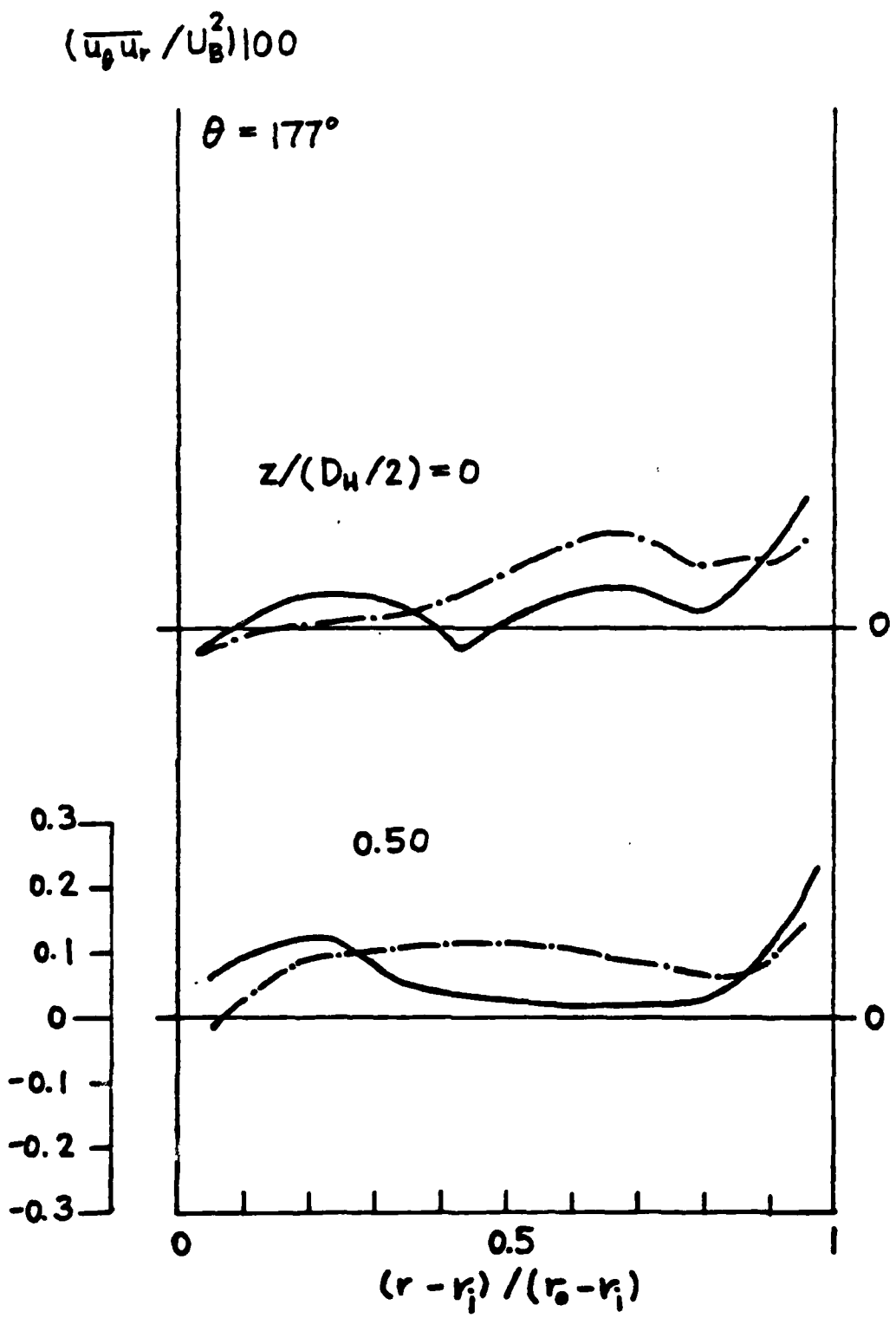


Figure 6.36 ASM calculations of $(\overline{u_\theta u_r} / U_B^2) \times 100$ at $\theta = 177^\circ$: (—) best fits to measurements, (---) ASM.

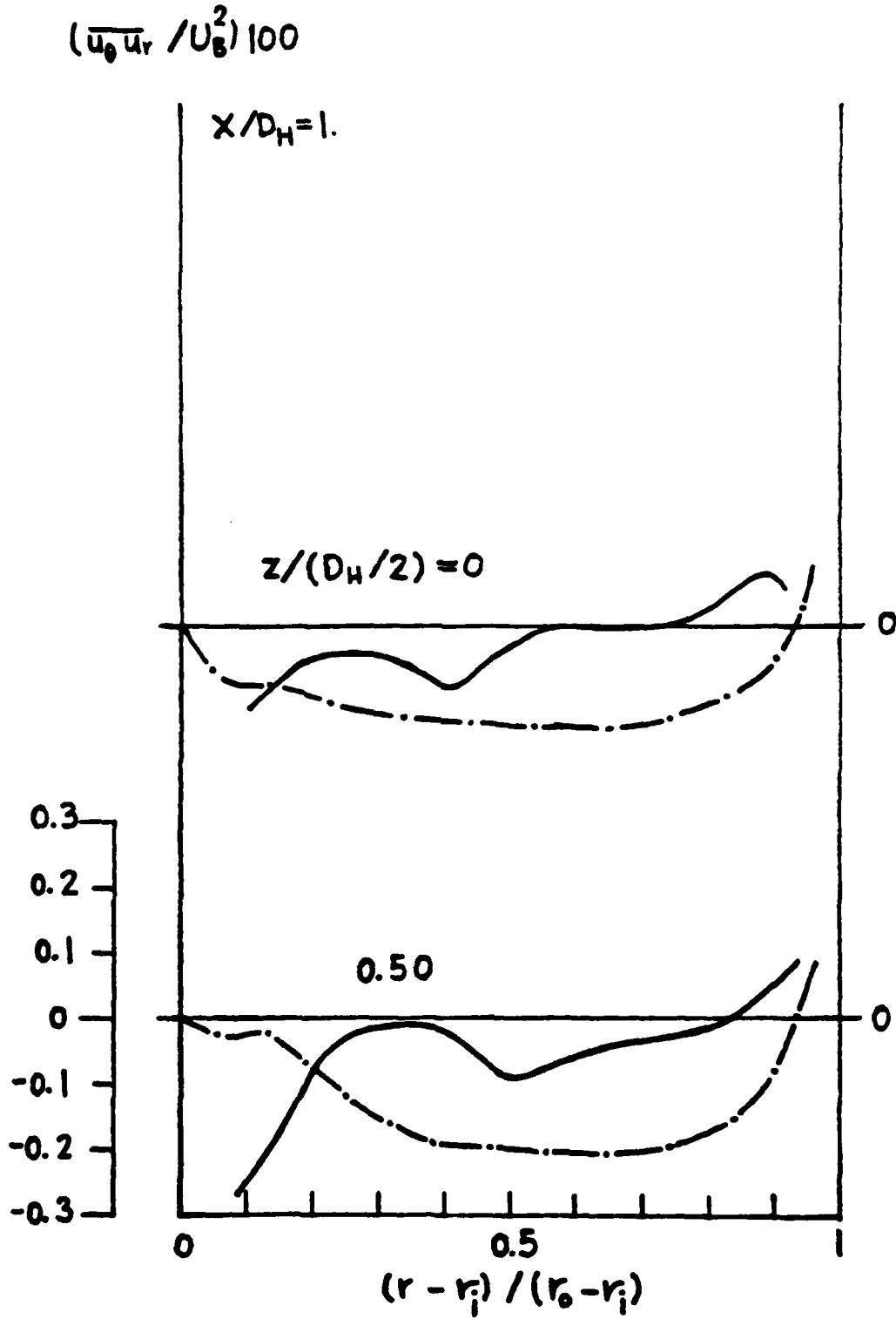


Figure 6.37 ASM calculations of $(\overline{u_\theta u_r} / U_B^2) \times 100$ at $x/D_H = 1$: (—) best fits to measurements, (---) ASM.

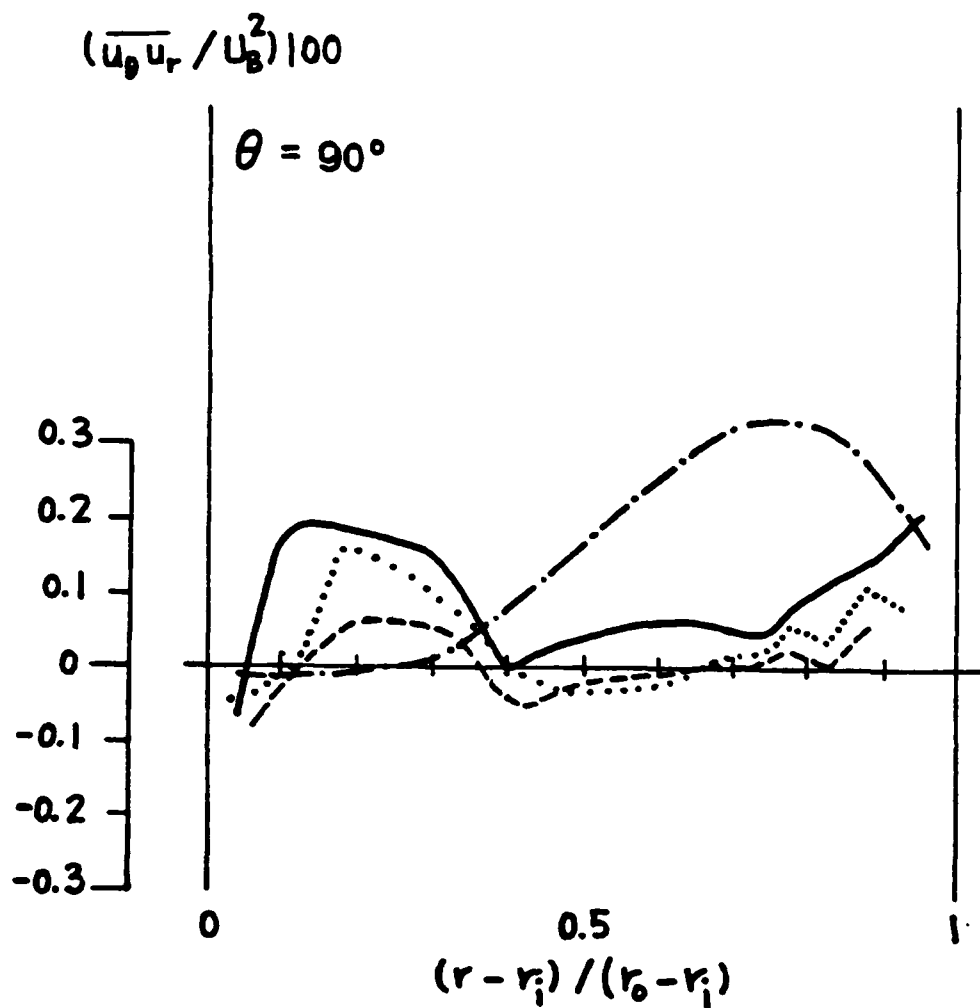


Figure 6.38 ASM calculations of $(\overline{u_\theta u_r} / U_B^2) \times 100$ at $\theta = 90^\circ$: (—) best fits to measurements, (---) ASM, (-.-) "experimental" test #1, (.....) "experimental" test #2.

END

FILMED

10-83

DTIC